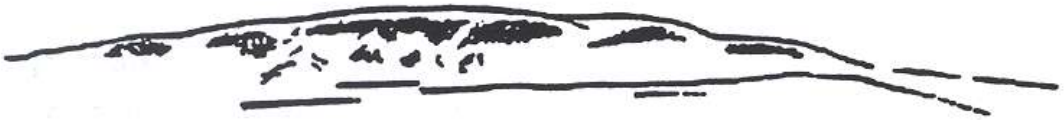

32nd SCANDINAVIAN SYMPOSIUM ON PHYSICAL ACOUSTICS
FINSE1222 HOTEL 8. February – 11. February 2009

PROGRAM

Sunday 8 February: (Some possible train arrivals: 18:16 from Bergen, and 17:14 and 20:16 from Oslo)
Dinner is served from 20:30
Opening 21:30

Monday 8:15 – 10:05 4 talks

8:15 – 8:40 Stig Synnes
Shallow water performance of AUV-based sonar

8:40 – 9:05 Roy Edgar Hansen
The HISAS interferometric synthetic aperture sonar: Experimental results and key learnings.

9:05 – 9:20 Coffee

9:20 – 9:45 Ann E.A. Blomberg
Adaptive Beamforming applied to Active Sonar Systems

9:45 – 10:05 Rolf J Korneliussen
Acoustic analysis and imaging of large euphausiid schools

10:05 – 15:45 Time available for skiing, ski-sailing and lunch. **Lunch served at: 14:00**

Monday 15:45 – 18:30 6 talks

15:45 – 16:10 Stig Kleiven
Thermoacoustic refrigerators: Time-domain modelling and experimental setup

16:10 – 16:35 Lars Ødegaard
Comsol Multiphysics Modelling of Underwater Acoustics: 101 ways to get into trouble.

16:35 – 17:00 Xueshan Bao
Modelling the Underwater Acoustic Communication Channel Using Program EasyPLR

17:00 – 17:15 Coffee

17:15 – 17:40 Guosong Zhang
The problems for point-to-point underwater acoustic communication

17:40 – 18:05 Karl Bolin, Andersson, A. Cederholm and I. Karasalo
Long distance sound propagation over a sea surface L.B.

18:05 – 18:30 Anders Løvstad
Propagation of ultrasound in steel tubes

Dinner is served at 19:00

Tuesday 8:15 – 10:40 3 talks + 3 short talks

8:15 – 9:00 Halvor Hobæk **(Invited talk)**
Parametric acoustic arrays: 50 years

9:00 – 9:25 Igor B. Esipov
Parametric Array Application in Shallow Water

9:25 – 9:40 Coffee

9:40 – 10:05 Audun Pedersen
Nonlinear sound propagation effects in fisheries research echo sounders

10:05 – 10:20 Espen Storheim
Sound speed in fish flesh - a method for quality control?

10:20 – 10:30 Mathias Sæther
Design of a broad band echo sounder transducer with constant beam pattern.

10:30 – 10:40 Adam Suleiman
Adaptive ultrasound transducer: array module

10:40 – 16:00 Time available for skiing, ski-sailing and lunch. **Lunch served at: 14:00**

Tuesday 15:45 – 18:30 6 talks + 1 short talk

15:45 – 16:10 Isabel Pérez-Arjona
Diffraction management with sonic crystals

16:10 – 16:35 Magne Aanes and Magne Vestrheim
Finite element studies of permittivity constants in piezocheramic disks

16:35 – 17:00 Halvor Hobæk and Anja Heggen
Analysis of echoes from a plane reflector - steps towards acoustic habitat mapping.

17:00 – 17:15 Coffee

17:15 – 17:40 Remi André Kippersund, Per Lunde, Kjell-Eivind Frøysa
Deposit detection using elastic plate waves.

17:40 – 18:05 Hanne Martinussen, Helge E. Engan and Astrid Aksnes.
Capacitive Micromachined Ultrasonic Transducer (CMUT): Charge diffusion and collapsed mode.

18:05 – 18:30 Shefeng Yan
Unified Approach to Optimal Design of Beamformers

18:30 – 18:40 Tormod Vaule
Thermoacoustical refrigerators, building a demonstration model

Dinner is served from 19:00

Tuesday 21:30 Applied fluid dynamics

Voluntary contributions

Wednesday 9:00 – 10:40 3 talks

9:00 – 9:25 Jens Hovem
Utbredelse av seismisk skytestøy i havet

9:25 – 9:50 Lars Hoff
Cardiac Monitoring Using Transducers Attached Directly to the Heart

9:50 – 10:15 Lars G. Johansen:
Adaptive ultrasound transducer: electronics module

Lunch served at: 11:00

One train to Oslo leave at 12:54. Two trains to Bergen leave at 12:25 and 15:26

Hotel contact info: email: booking@finse1222.no; Telephone: +47 56 52 71 00; Telefaks: +47 56 52 71 10

Participants

1.	Helge Balk	University of Oslo
2.	Xueshan Bao	Norwegian University of Science and Technology
3.	Bjarte Berntsen	Kongsberg Maritime
4.	Ann E.A. Blomberg	University of Oslo
5.	Karl Bolin	Kungliga Tekniska Högskolan
6.	Helge E Engan	Norwegian University of Science and Technology
7.	Igor Episov	Russian Oil & Gas University
8.	Víctor Espinosa	Universitat Politècnica de València
9.	Kjell-Eivind Frøysa	Christian Michelsen Research
10.	Roy Edgar Hansen	Norwegian Defence Research Establishment
11.	Anja Heggen	University of Bergen
12.	Halvor Hobæk	IFT, University of Bergen
13.	Lars Hoff	
14.	Jens Hovem	Norwegian University of Science and Technology
15.	Trond Jenserud	Norwegian Defence Research Establishment
16.	Lars G Johansen	University of Bergen
17.	Ganpan Ke	Norwegian University of Science and Technology
18.	Remi A Kippersund	Christian Michelsen Research AS
19.	Stig Kleiven	Chalmers University of Technology
20.	Vidar Knappskog	Christian Michelsen Research AS
21.	Rolf Korneliussen	Institute of Marine Research
22.	Ulf Kristiansen	Norwegian University of Science and Technology
23.	Bjørnar Langli	Kongsberg Maritime
24.	Anders Løvstad	Norwegian University of Science and Technology
25.	Svein Mjølsnes	Forsvarets Logistikkorganisasjon (FLO)
26.	Geir K Nilsen	Bjørge Naxys AS
27.	Torstein O Sæbø	Norwegian Defence Research Establishment
28.	Audun Pedersen	Christian Michelsen Research
29.	Geir Pedersen	Christian Michelsen Research
30.	Isabel Pérez-Arjona	Universitat Politècnica de València
31.	Arne Reitan	
32.	Noela Sánchez-Carnero	Universidade de a Coruña
33.	Morten Smedsund	Norwegian Defence Research Establishment
34.	Marianne Solberg	IFT, University of Bergen
35.	Stian H Stavland	Christian Michelsen Research
36.	Espen Storheim	IFT, University of Bergen
37.	Adam Suleiman	IFT, University of Bergen
38.	Haohai Sun	Norwegian University of Science and Technology
39.	Stig Synnes	Norwegian Defence Research Establishment
40.	Mathias Sæther	IFT, University of Bergen
41.	Frank Tichy	Kongsberg Maritime Subsea
42.	MagneVestrheim	University of Bergen
43.	Shefeng Yan	Norwegian University of Science and Technology
44.	Guosong Zhang	Norwegian University of Science and Technology
45.	Lars Ødegaard	Norwegian Defence Research Establishment (FFI)
46.	Magne Aasheim	IFT, University of Bergen
47.	Erlend Viggen	Norwegian University of Science and Technology
48.	Tormod Vaule	Norwegian University of Science and Technology

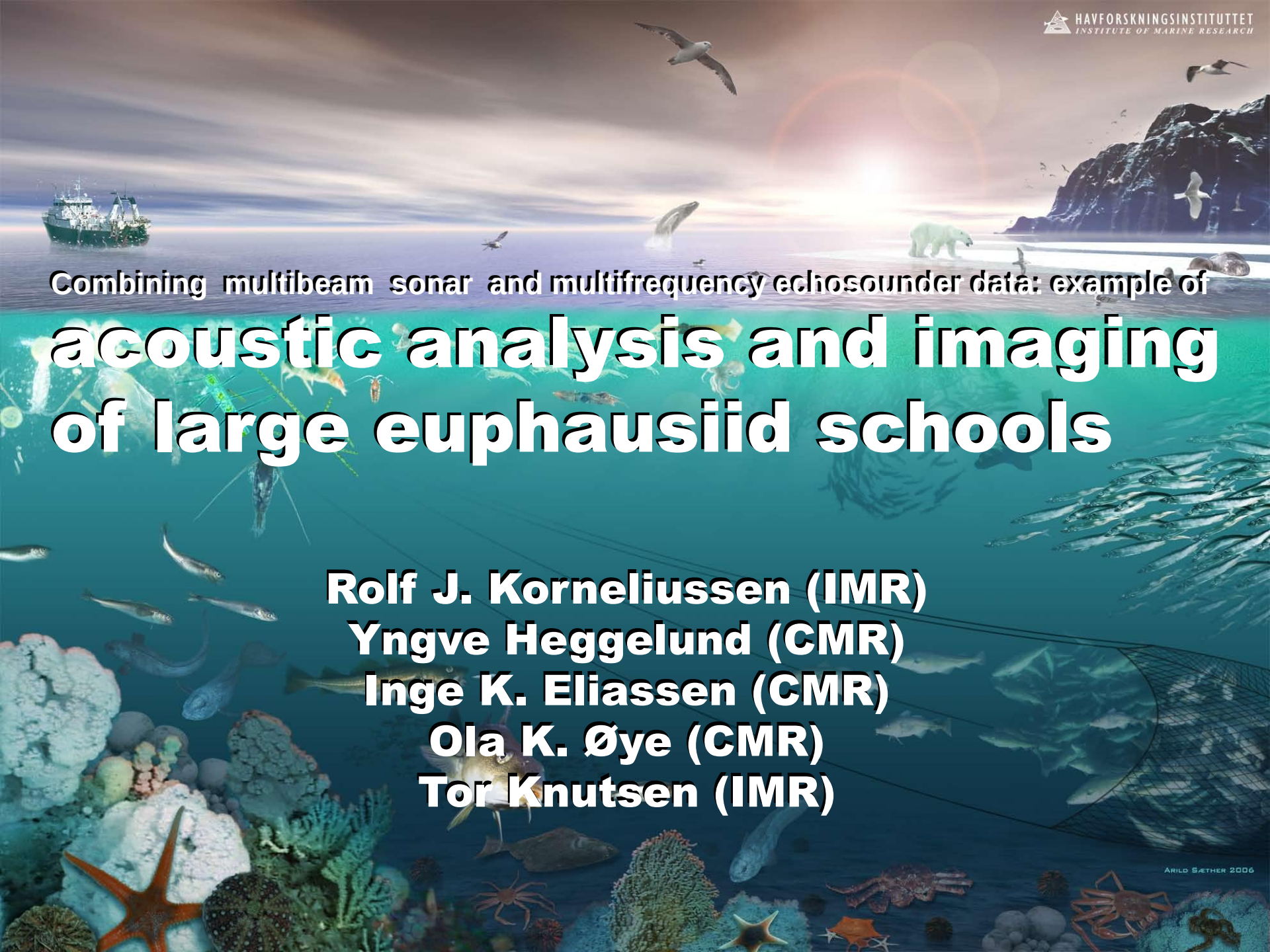
HAVFORSKNINGSINSTITUTTET
INSTITUTE OF MARINE RESEARCH
Combining multibeam sonar and multifrequency echosounder data: example of
acoustic analysis and imaging of large euphausiid schools
Rolf J. Korneliussen (IMR)
Yngve Heggelund (CMR)
Inge K. Eliassen (CMR)
Ola K. Øye (CMR)
Tor Knutsen (IMR)
Arild Sæther 2006

Overview

1. Ecosystems and ecosystem management
2. Acoustic needs for ecosystem investigations
3. 3D/4D-measurements of schools
4. Non-invasive verification of 3D-measurements
5. Trawl verification
6. Conclusions

Ecosystem approacch
for management of marine resources

- The whole water column have to be measured simultaneously for all species…
- … which inherently mean that some species are not optimally distributed for measurements

The Barents sea ecosystem (simplified)

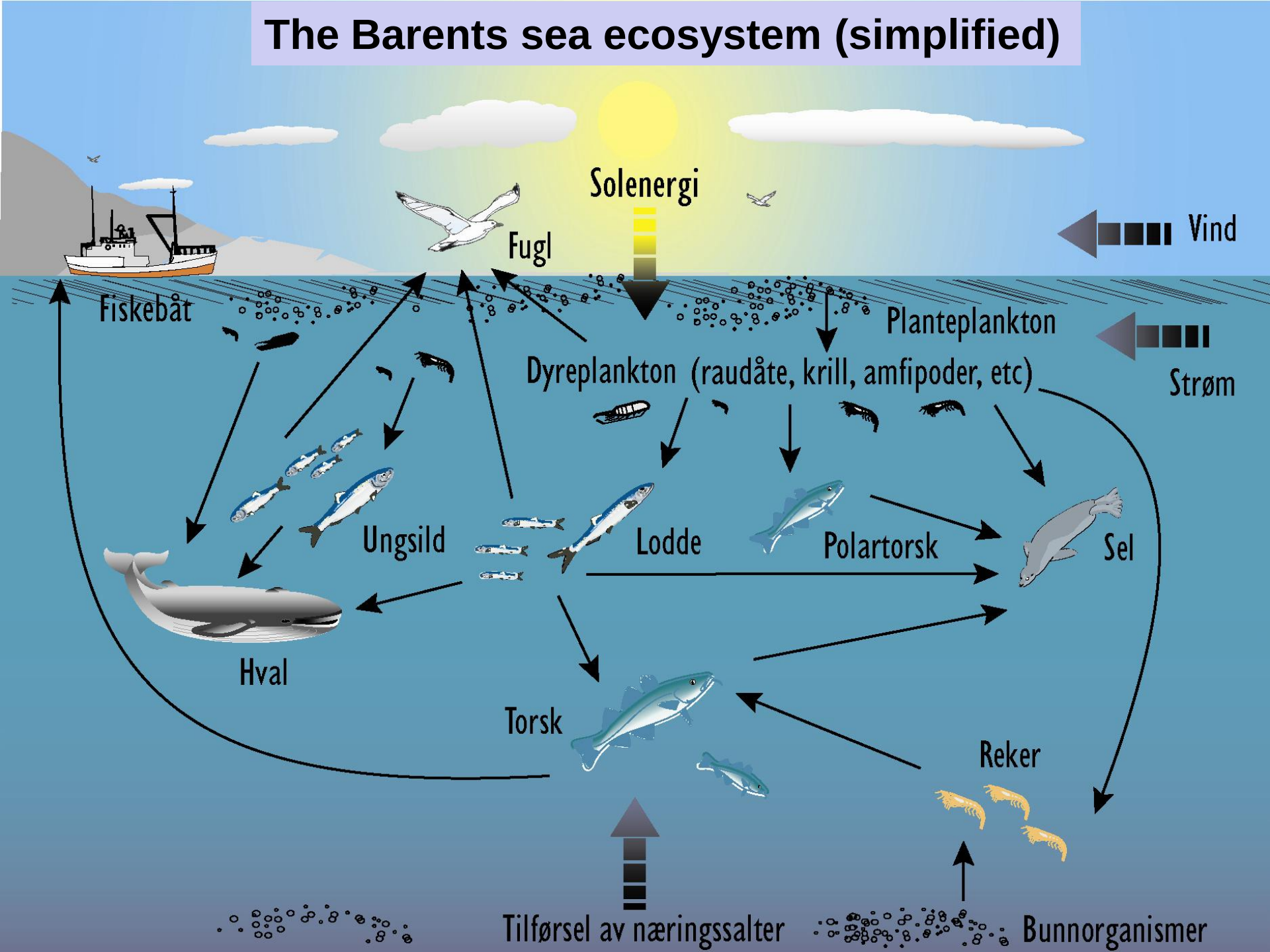

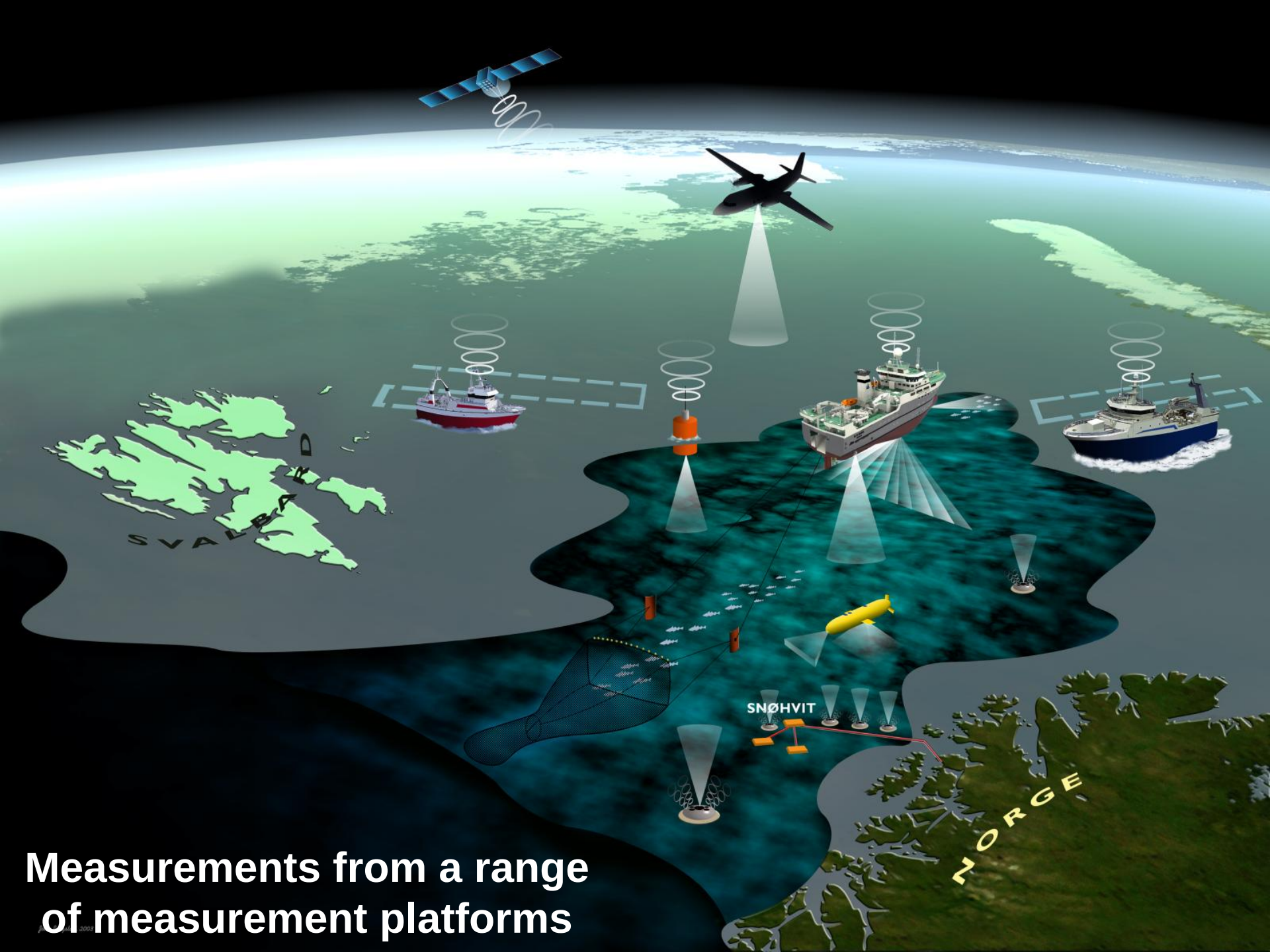

Measurements from a range of measurement platforms

The acoustic needs

for investigating species of marine ecosystems

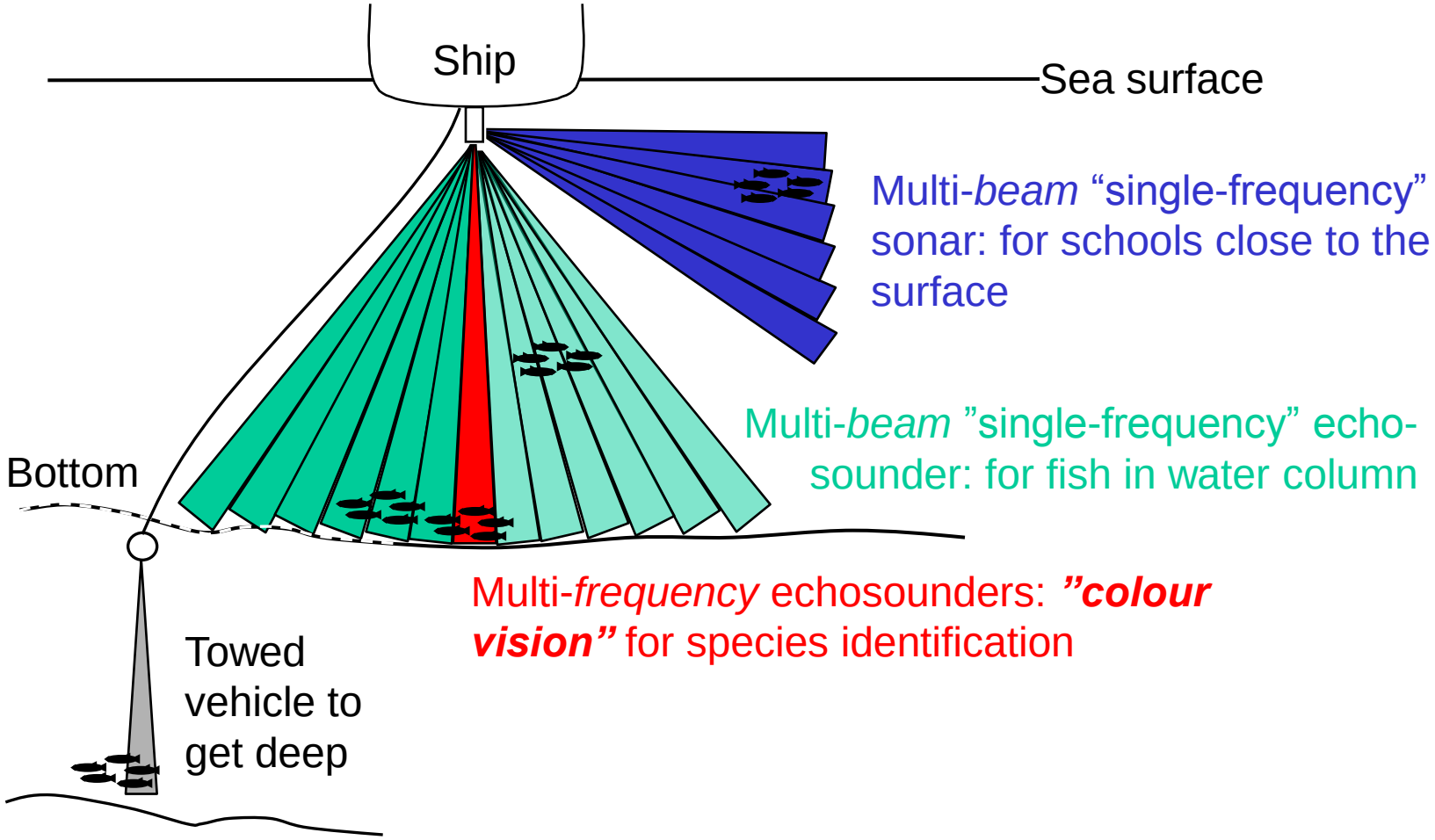

Acoustic needs as implemented for abundance estimation at IMR

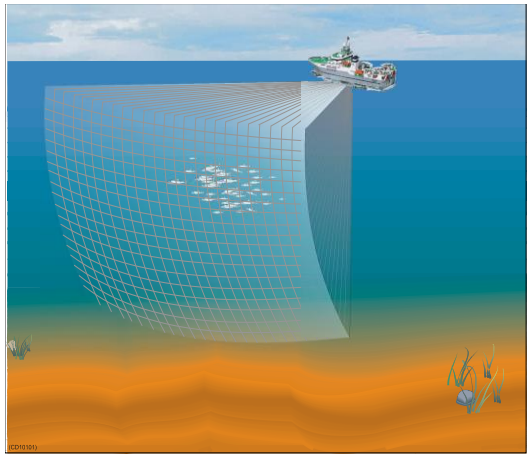

Multibeam sonar (**MS70 – 500 beams**)

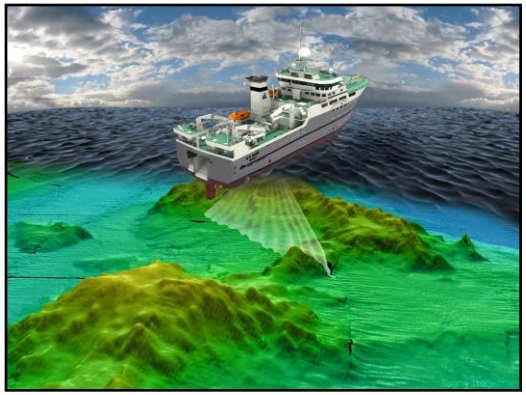

Multibeam echosounder **ME70**

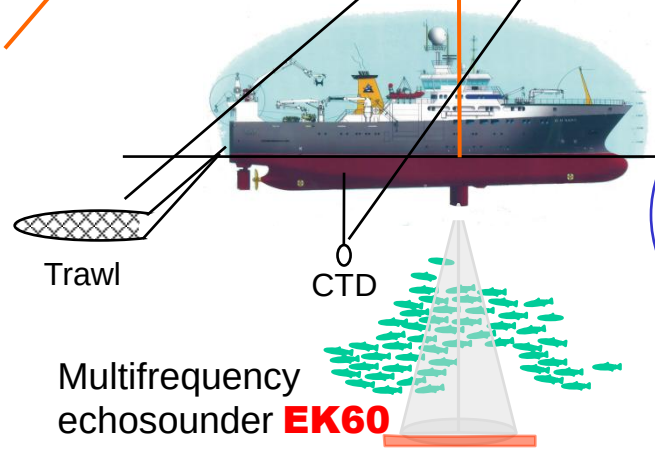

Multifrequency echosounder **EK60**

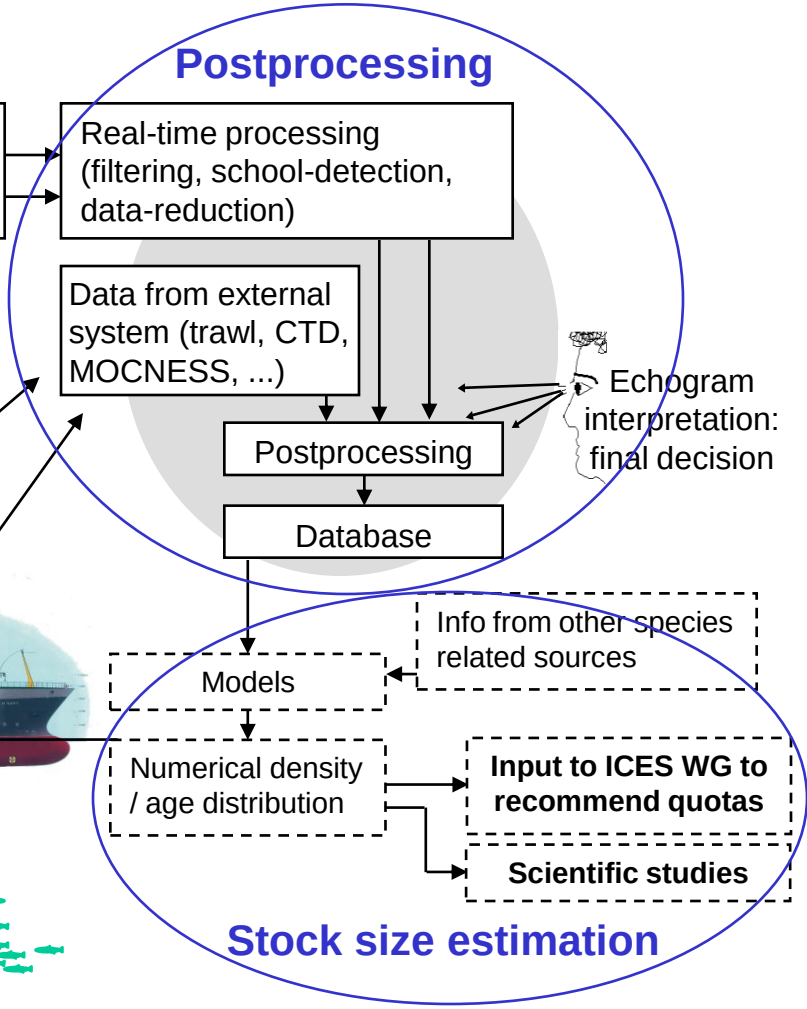

Essential:
- *combination of acoustic data with size distribution from biological samples*
- *scientists (not the system) take the final decision*

IMR equipment

multibeam echosounder not available

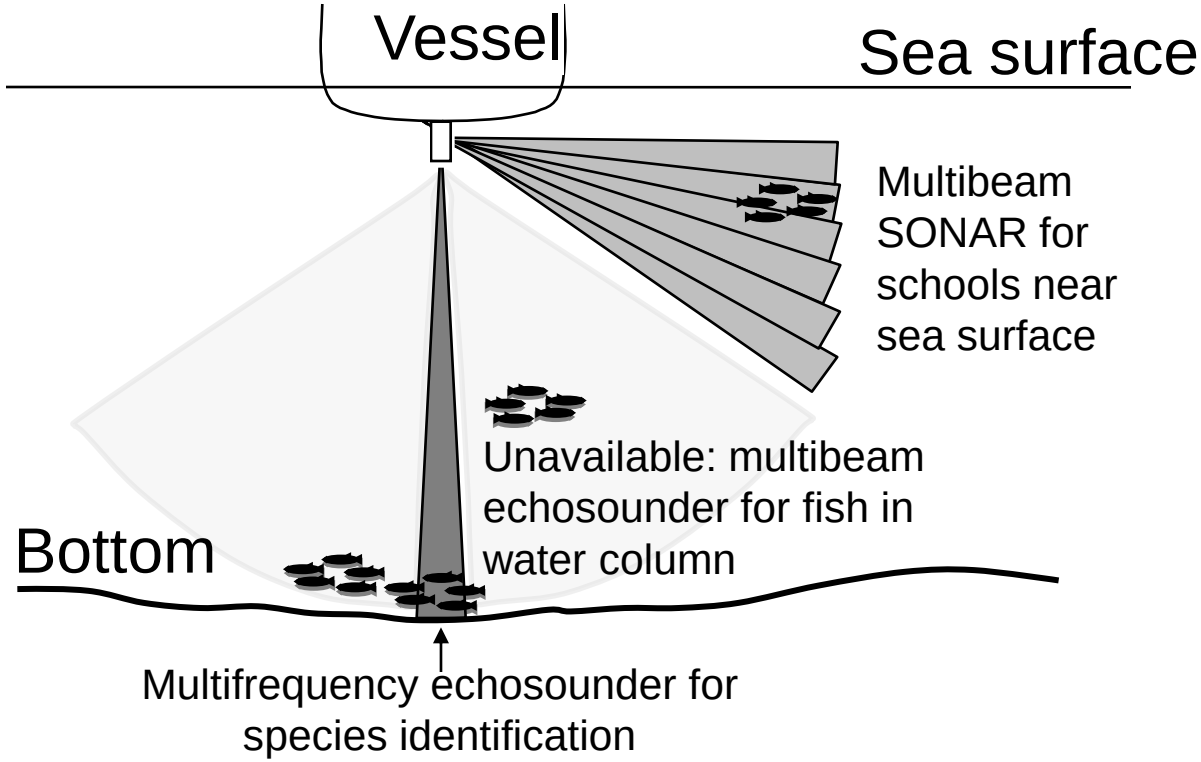

Problem: no overlapping volumes between EK60 and MS70

Interface of operational system implementing acoustic needs

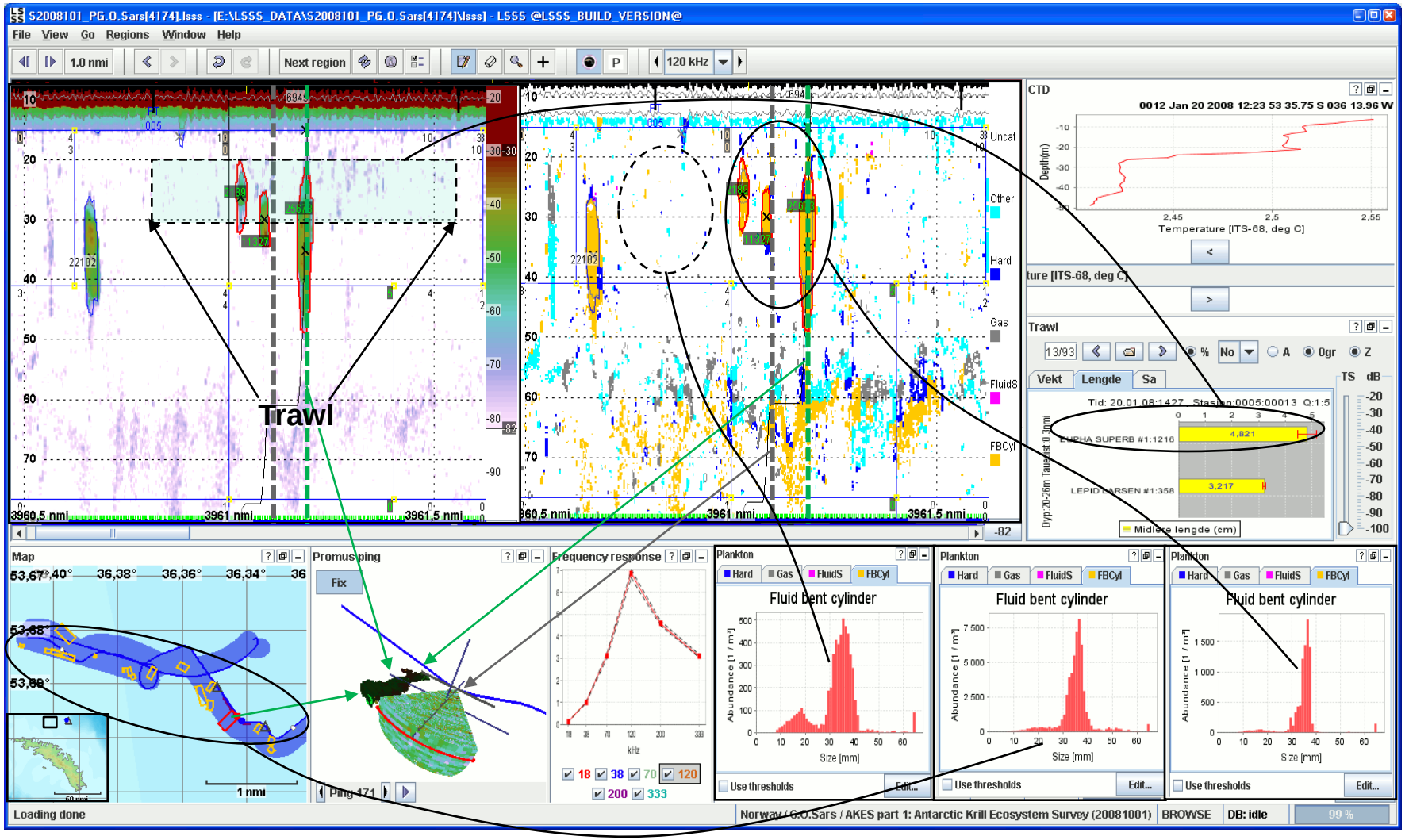

Not in schools All schools Trawled schools

Non-invasive verification of 3D/4D measurements of schools

a)

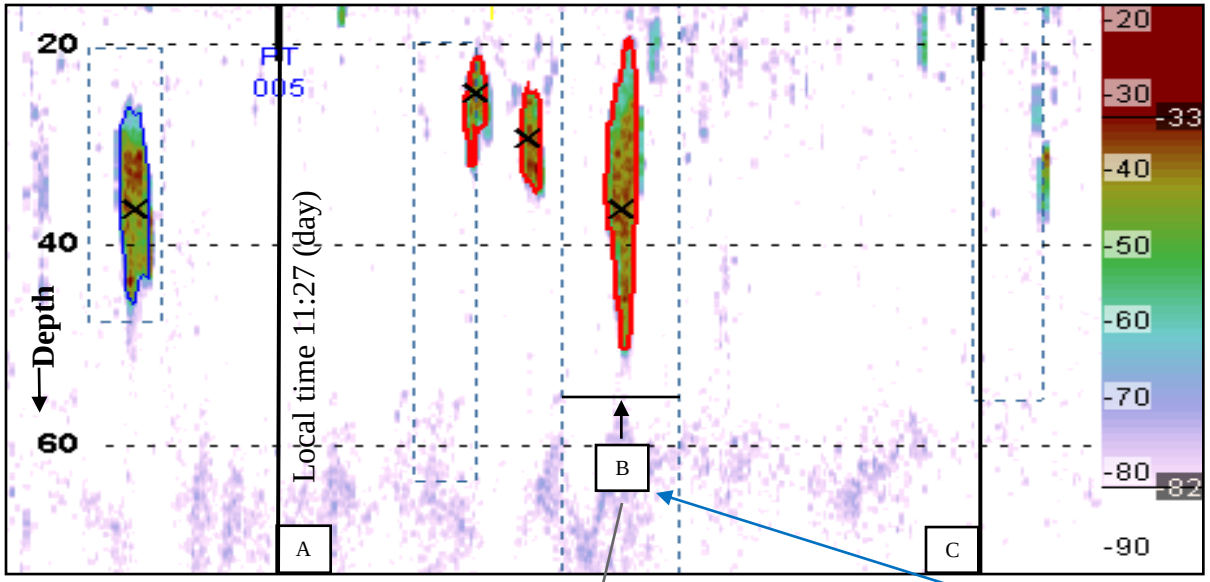

b)

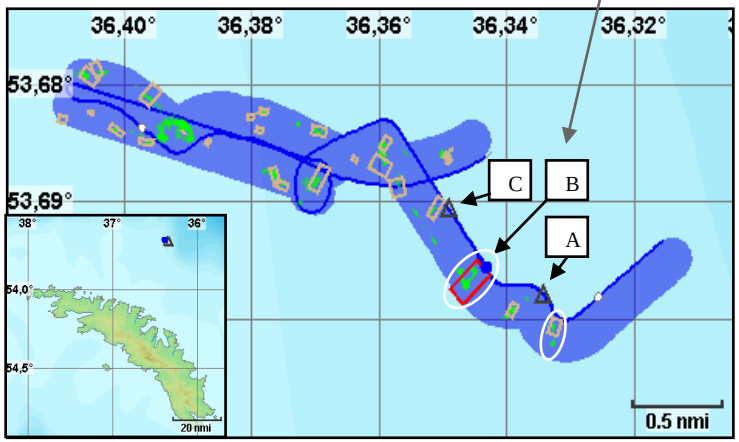

c)

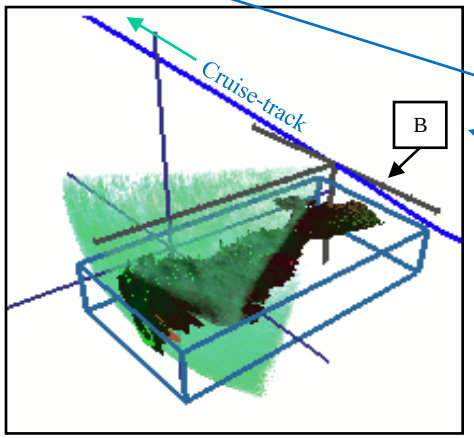

Some school parameters comparable 3D and 2D

3D/4D: max/min elongation

$$E_{max} = \frac{L_{BC,max}}{H_{BC}} \qquad E_{min} = \frac{L_{BC,min}}{H_{BC}}$$

$L_{BC,min}$ and $L_{BC,max}$ are horizontal dimensions and H_{BC} of corrected school bounding box

2D: elongation at B

$$E = \frac{L_{BC}}{H_{BC}}$$

E = 2.4

E_{min} = 2.9

E_{max} = 7.5

3D measurements of schools

essentially

- Multi-beam, but single-frequency: morphological measures for species id
- Volumetric measurements and calibrated s_v for quantification

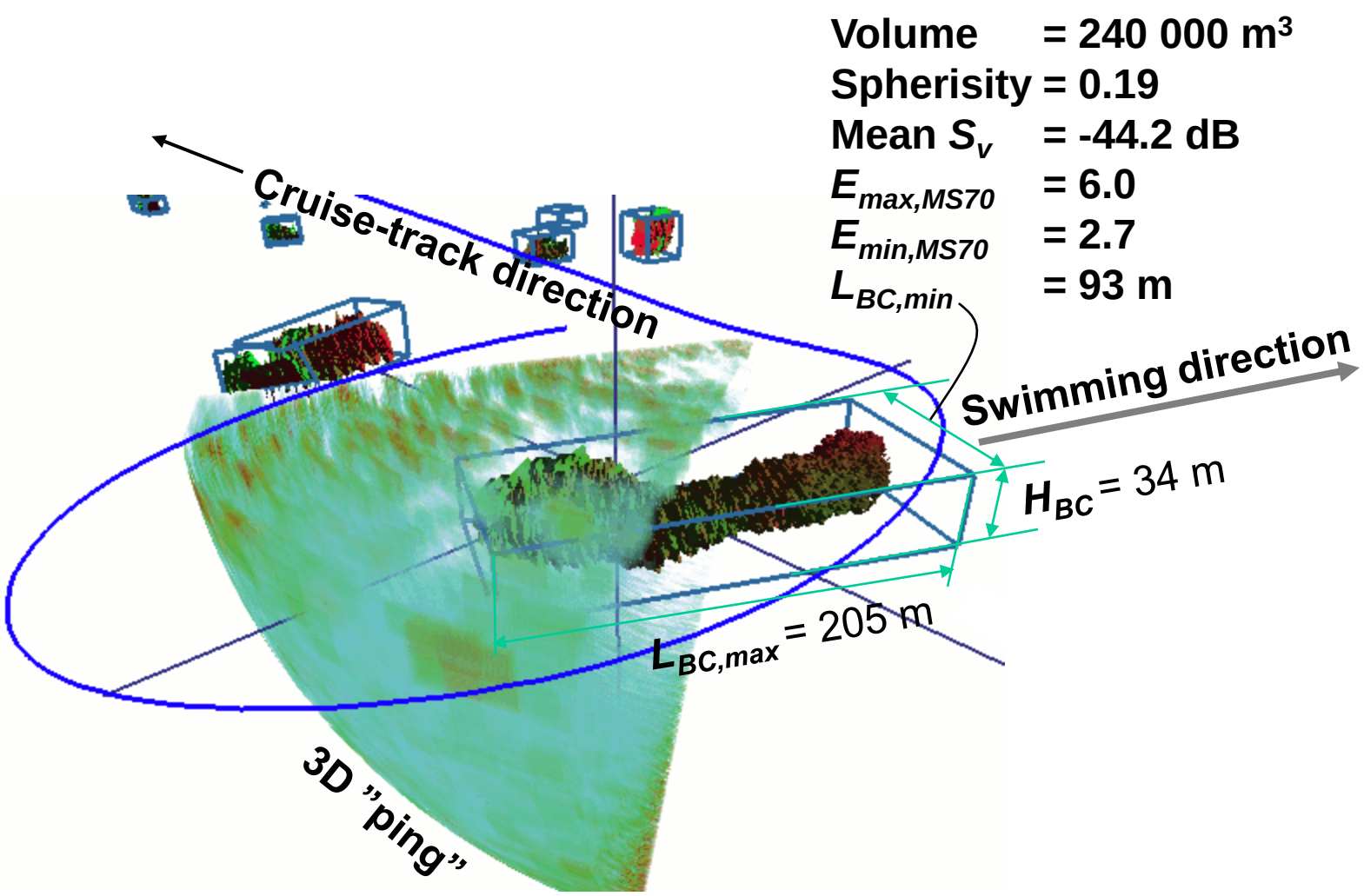

3D measurement sequence

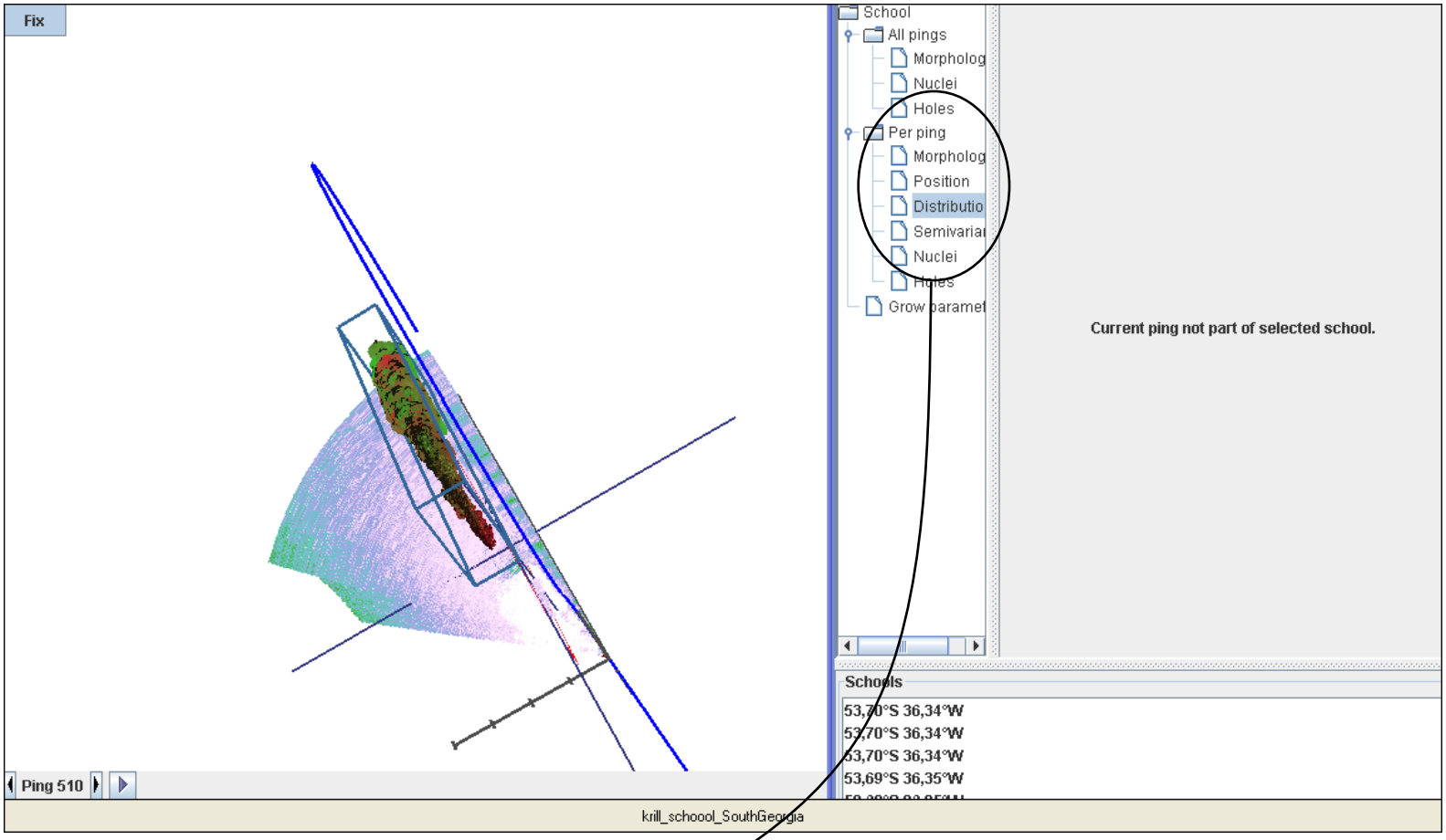

Per ping calculations

Verification of estimated length

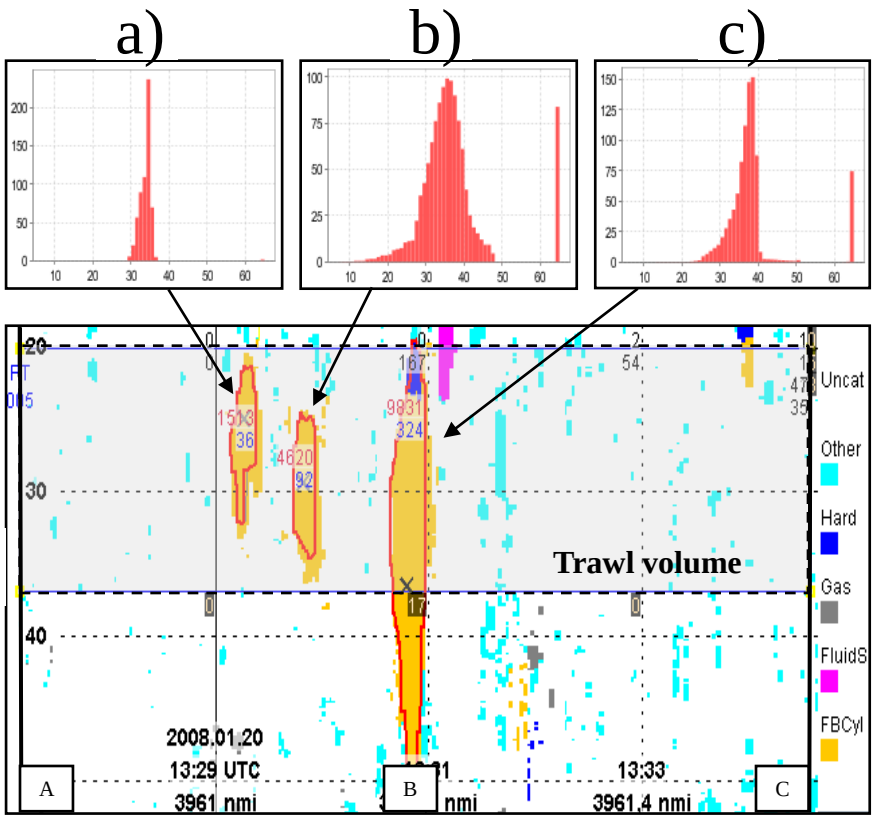

(a-c) Lengths of three schools

(d) Krill: orange synthetic colour

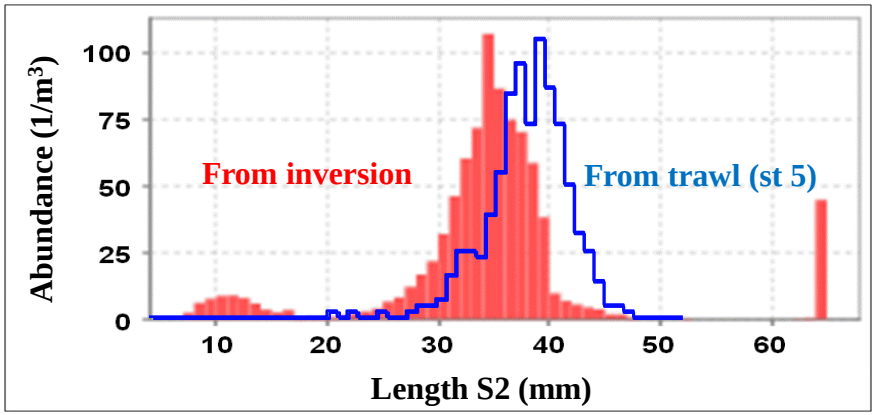

(e) Estimated length (grey area in d) compared to trawl catch. Catch: 99.99% *Euphausia superba* (1000 kg) of S2=38.0 3.3 mm (= AT=46.2 4.1 mm*). Estimated: 36 mm mean.*

Species identification and size estimation

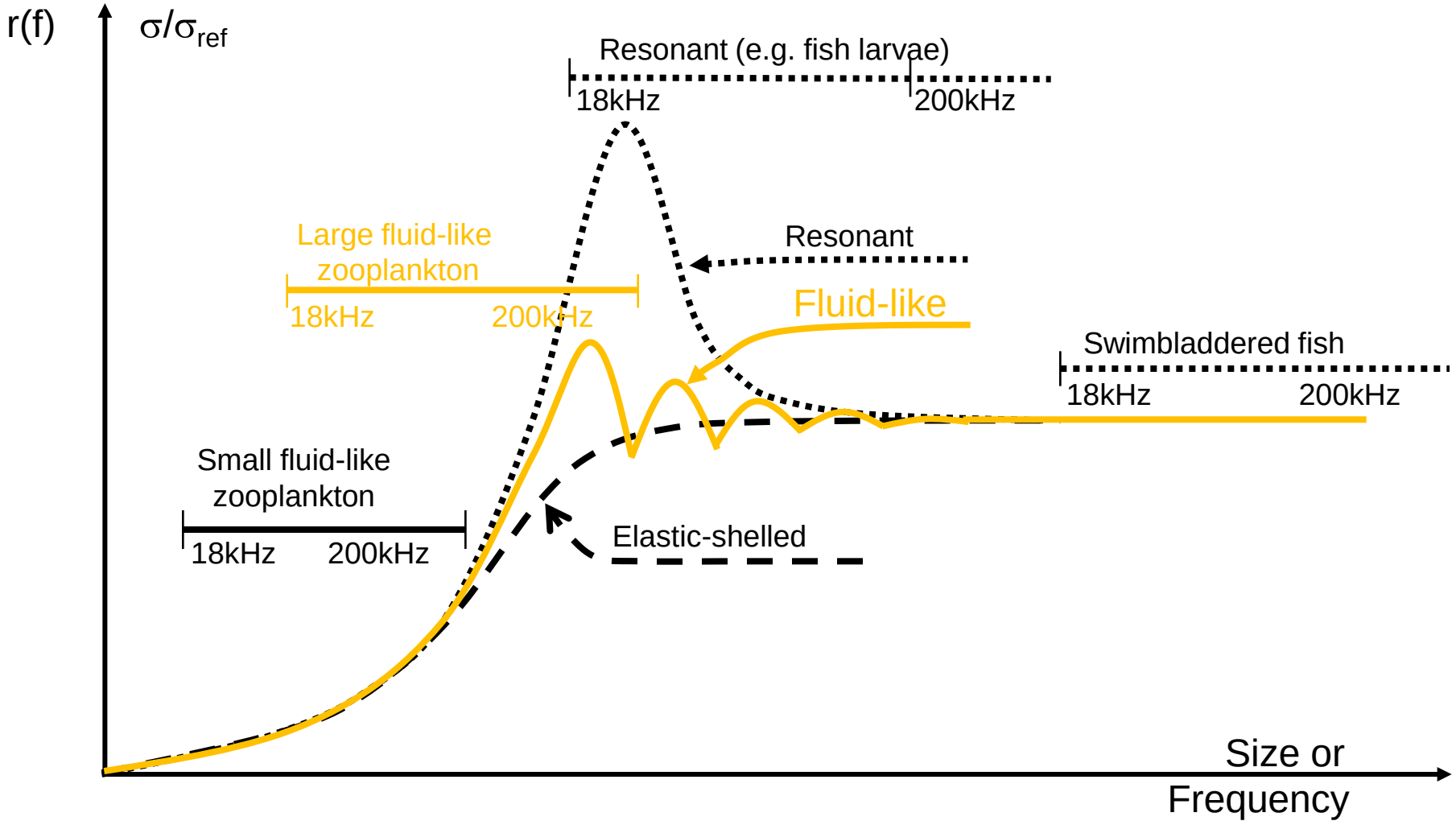

Length measures of euphausiids

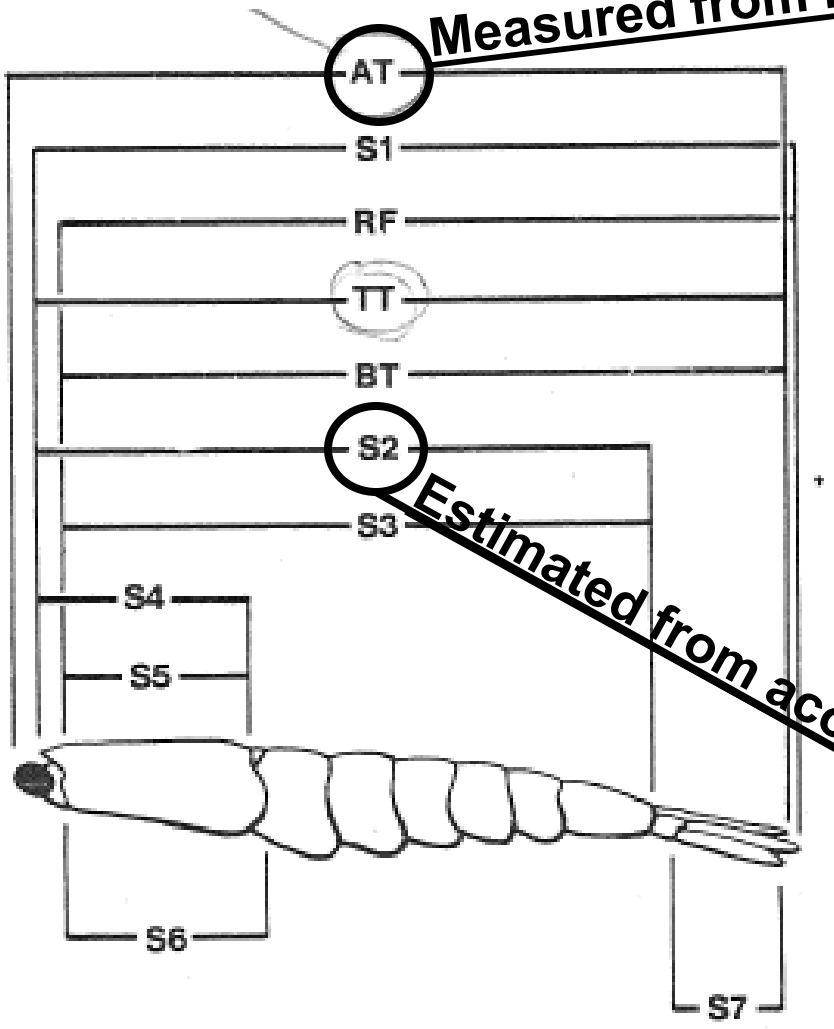

Measured from biological samples

Estimated from acoustic data

*Anterior edge of eye to tip of telson

Tip of rostrum to tip of uropods, excluding setae

Base of eye-stalk to tip of uropods, excluding setae (reference length)

*Tip of rostrum to tip of telson, excluding setae

NB!!

*Base of eye to tip of telson (can include setae e.g. Clarke 1976)

Tip of rostrum to posterior edge of 6th abdominal segment

Base of eye-stalk to posterior edge of 6th abdominal segment

Tip of rostrum to mid-dorsal posterior edge of carapace

Base of eye-stalk to mid-dorsal posterior edge of carapace (oblique axis)

Base of eye-stalk to lateral edge of carapace

Total length of uropod, excluding setae

Fig. 1. Definitions and codes for various length measurements of *Euphausia superba*.

(From Morris et. al, 1988

Conclusions

- **Schools visualised during routine survey operations**
- **School descriptors calculated: in future to be used for reliable identification of the species of schools**
- **Zooplankton specimen size calculated from acoustic data and verified to give reasonable results.**

32nd Scandinavian Symposium on Physical Acoustics 2009 at Finse

Thermoacoustic refrigerators: Time-domain modelling and experimental setup

Stig Kleiven

Chalmers University of Technology
Division of Applied Acoustics, Dep. of Civil and Environmental engineering, CHALMERS, SE-41296 Gothenburg, SWEDEN
Email: stig.kleiven@chalmers.se

Comments to the presentation

Most of the content in my presentation to the SSPA 2009 has been described in more detail in other publications:

- The experimental setup presented is described in more detail in my licentiate thesis [1].
- The equivalent source method (ESM) in the time-domain is described in my licentiate thesis [1] and in the article [2].
- The finite difference (FD) model for thermoacoustic devices that was presented was based on the model by M. Hamilton *et al.* [3].
- The combination of ESM and finite-difference time-domain (FDTD) is described in the article [2].
- The combination of ESM and the two-step Lax-Wendroff scheme for adiabatic wave propagation is described in the conference paper submitted to NOVEM 2009 [4].

References

[1] S. Kleiven. *Thermoacoustic refrigerators: Time-domain modelling and experimental setup*. Chalmers University of Technology, Sweden, 2008. Technical report, lic 2008:4, ISSN 1652-9146.

[2] S. Kleiven, K. Larsson, and W. Kropp. Time-domain modelling: Combining ESM and FDTD methods for acoustic wave propagation. *Acta Acustica United with Acustica*. To be published, accepted 28 Oct. 2008.

[3] M. F. Hamilton, Y. A. Ilinskii, and E. A. Zabolotskaya. Nonlinear two-dimensional model for thermoacoustic engines. *J. Acoust. Soc. Am.*, 111:2076–2086, 2002.

[4] S. Kleiven, W. Kropp, and K. Larsson. Time-domain modelling of thermoacoustic devices: Combining esm and finite-difference methods. *NOVEM*. To be in conference proceedings, April 2009.

Thermoacoustic refrigerators: Time-domain modelling and experimental setup

Stig Kleiven
stig.kleiven@chalmers.se

February 9, 2009

Introduction

Thermoacoustics

- heat generates sound (engine)
- heat pumping driven by sound (heat pump/refrigerator)
- examples of applications
  - refrigerator in space shuttle
  - solar-powered thermoacoustic refrigerator
  - acoustic Stirling engine

Thermoacoustic principle

1

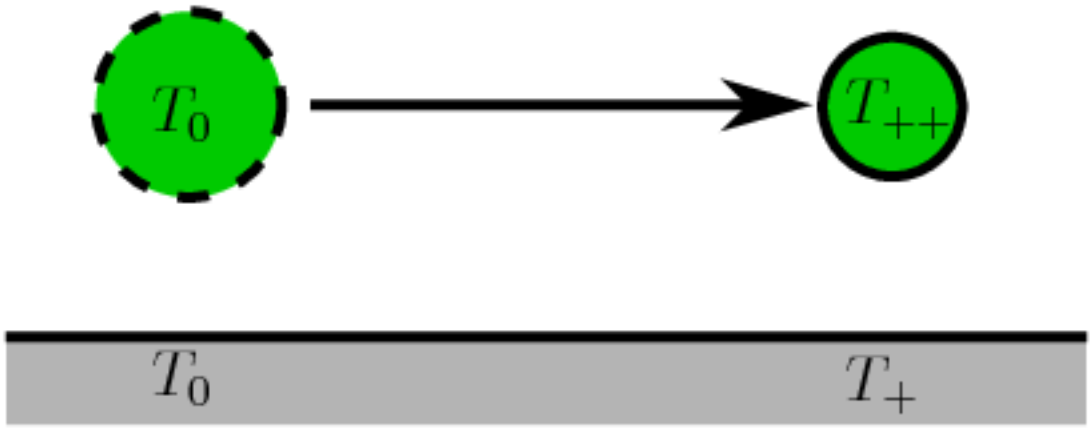

compression and displacement

$\Rightarrow$ higher p and higher T

Thermoacoustic principle

2

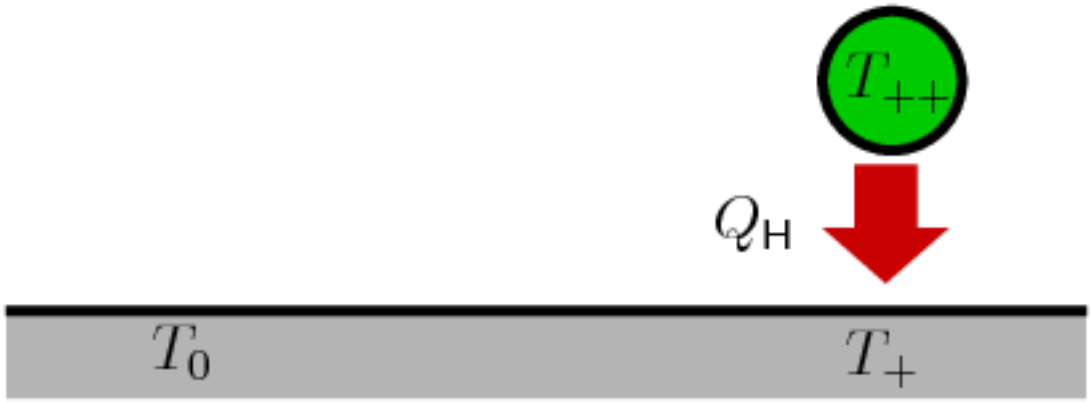

heat transfer: gas $\Rightarrow$ plate

Thermoacoustic principle

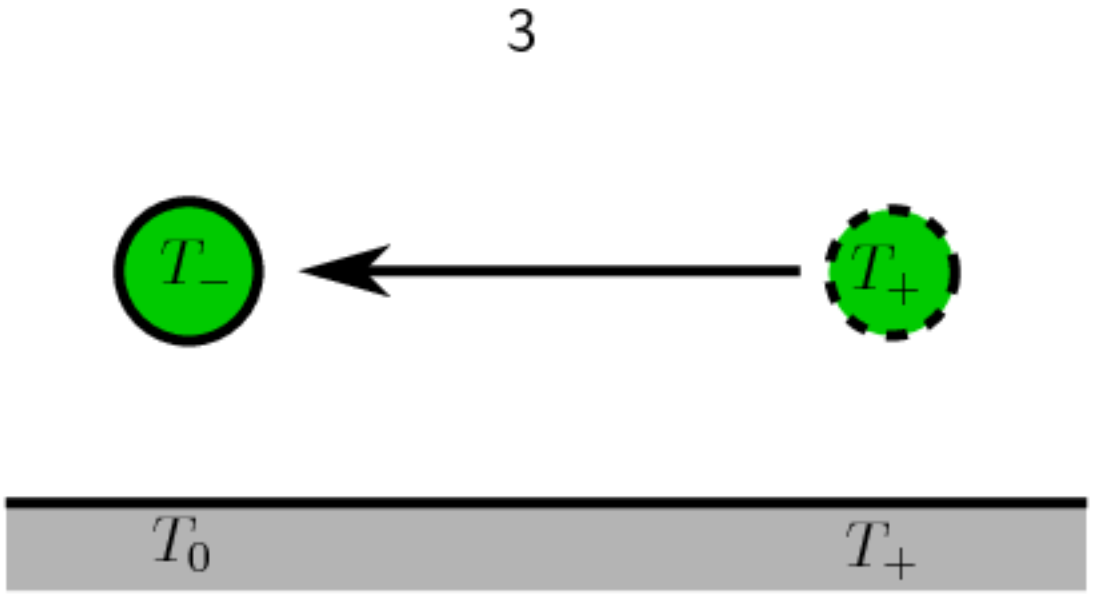

expansion and displacement

$\Rightarrow$ lower p and lower T

Thermoacoustic principle

4

heat transfer: plate $\Rightarrow$ gas

Thermoacoustic principle

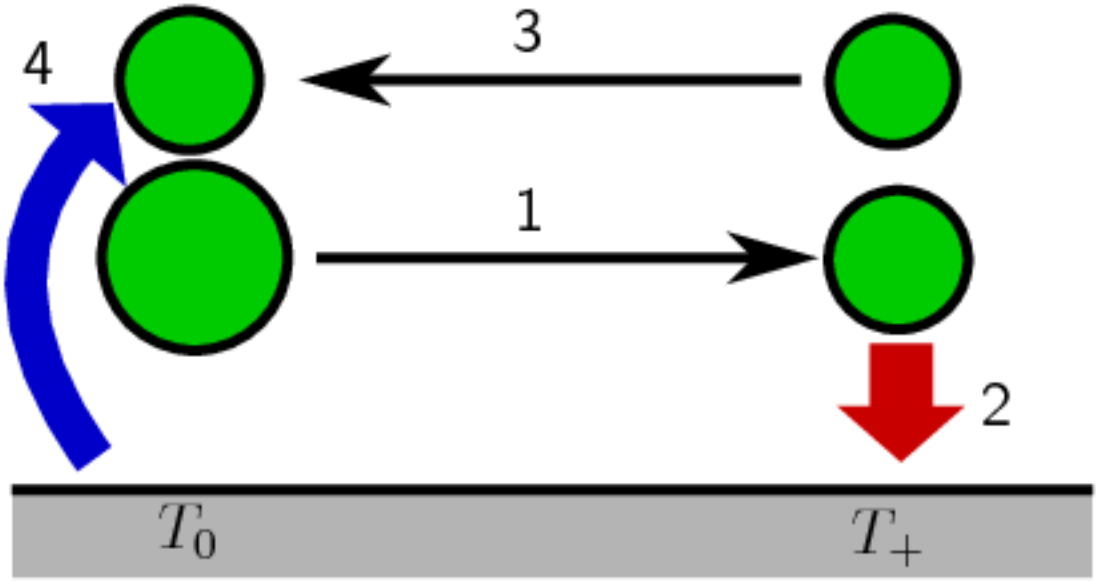

heat pumping from cold to hot

Standing-wave thermoacoustic refrigerator

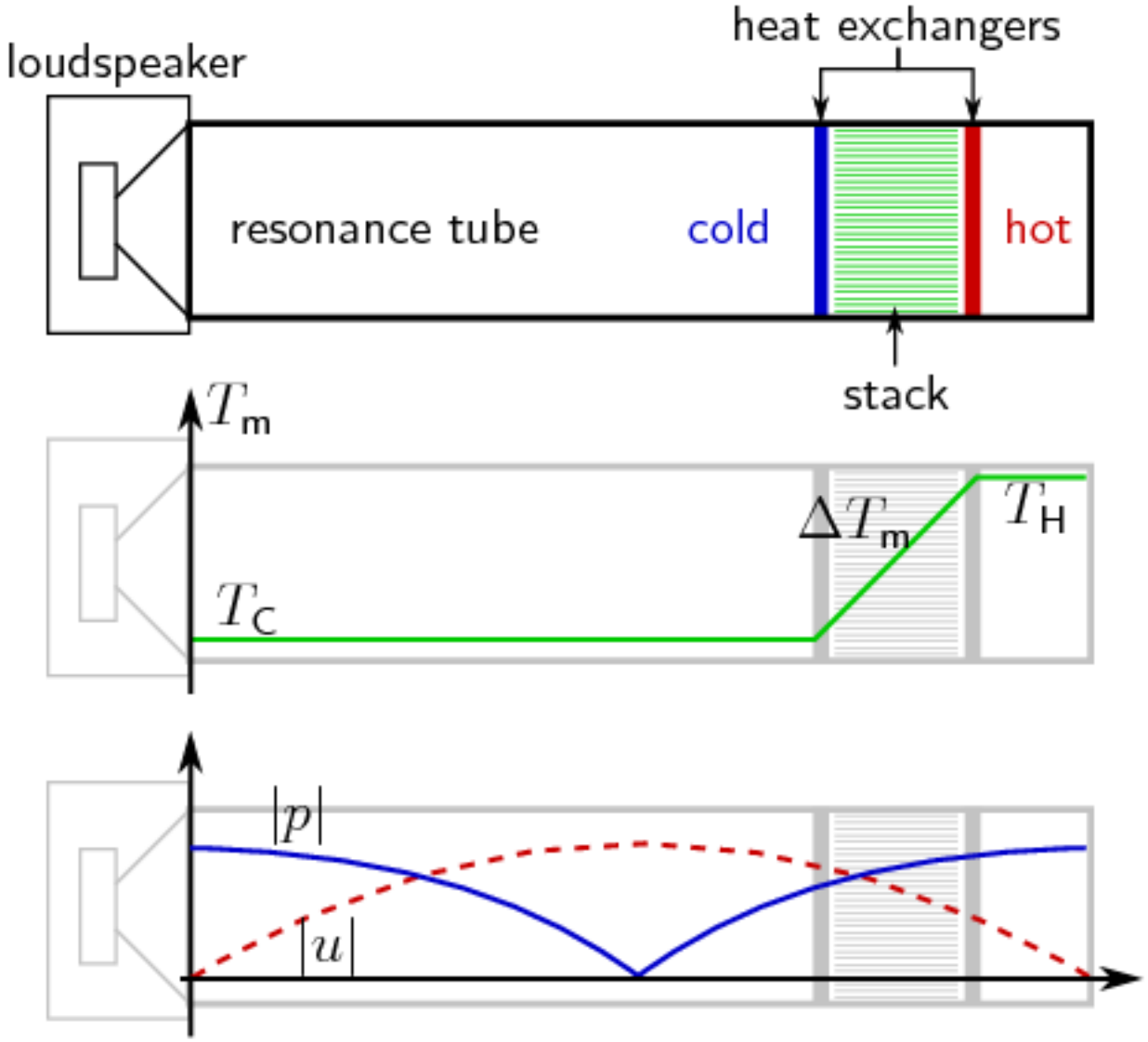

Benefits

- Environmentally safe
- Few moving parts
- Robust
- Cheap
- Low maintenance
- Low weight

Drawbacks

- Low efficiency
- Low power

How to improve the efficiency?

- optimise each component
- optimise the acoustic field
  - differs from standing-wave

How to improve the efficiency?

- optimise each component
- optimise the acoustic field
  - differs from standing-wave

$\Rightarrow$ adaptively vary the acoustic field?

$\Rightarrow$ improve the efficiency by active control?

  - time-domain model needed
  - experimental setup needed

Experimental setup

Requirements

- Flexibility
- Simplicity
- Time-varying boundary conditions
- Measurable temperature difference
- Measurable cooling power

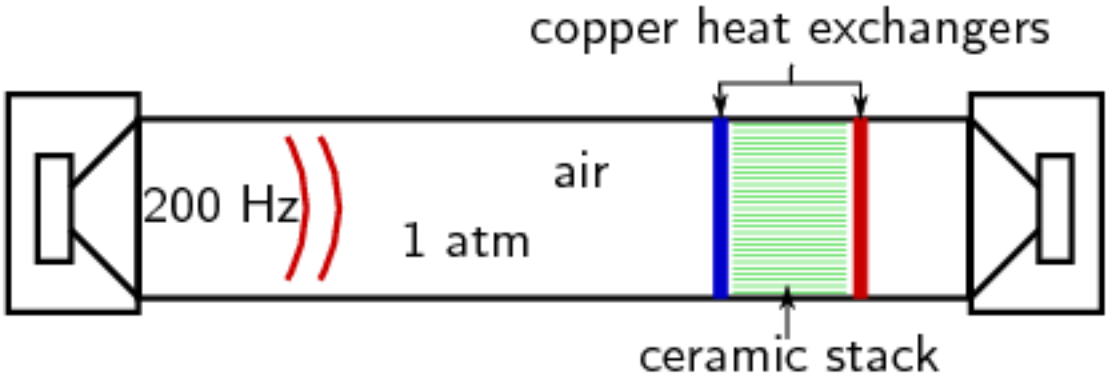

Complete setup

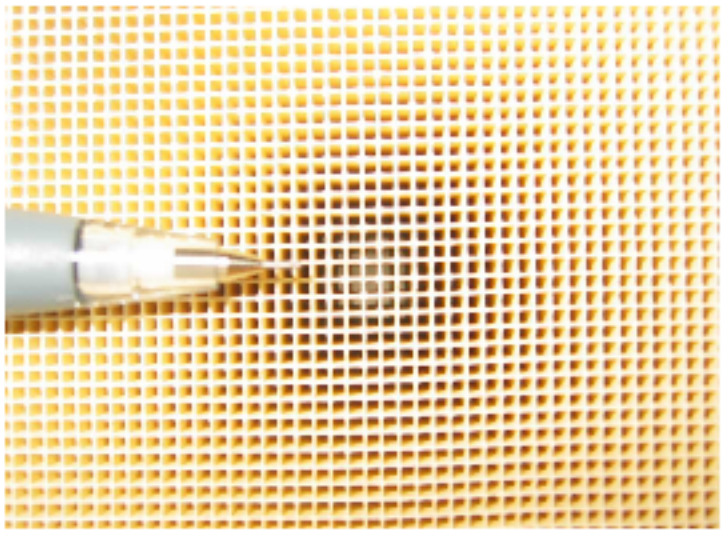

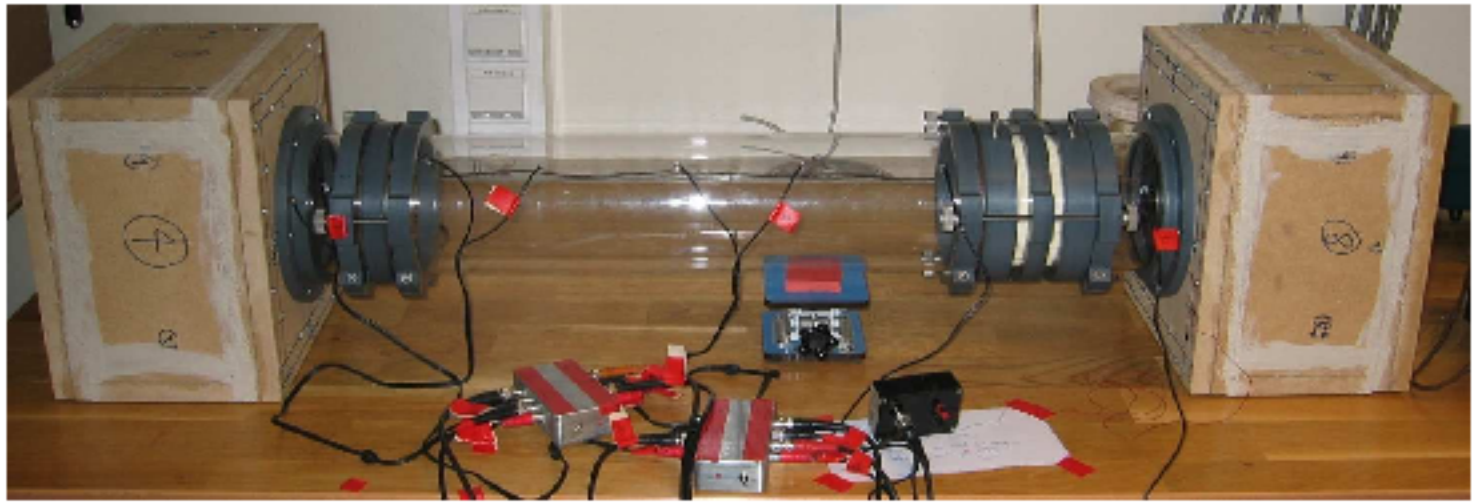

Results

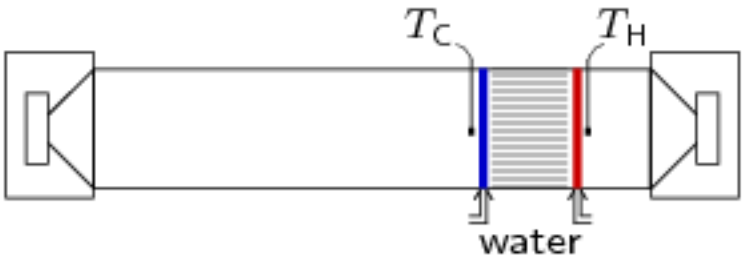

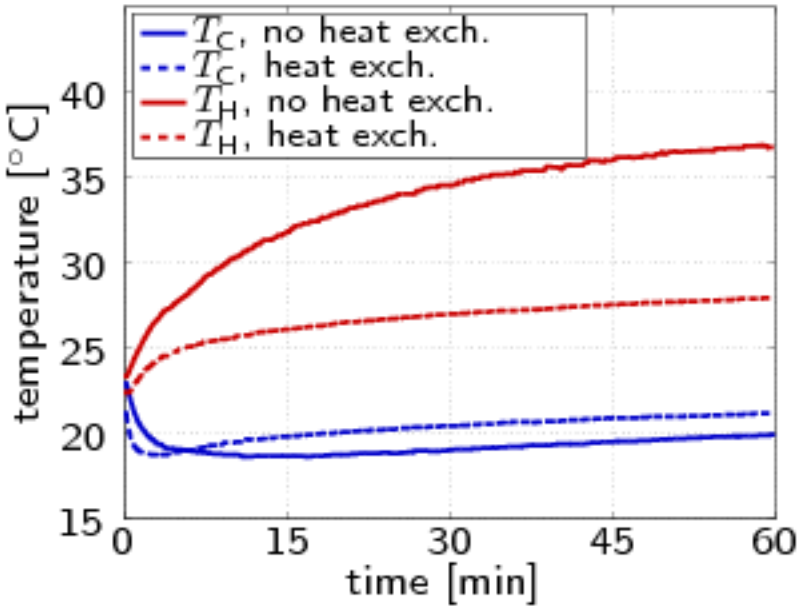

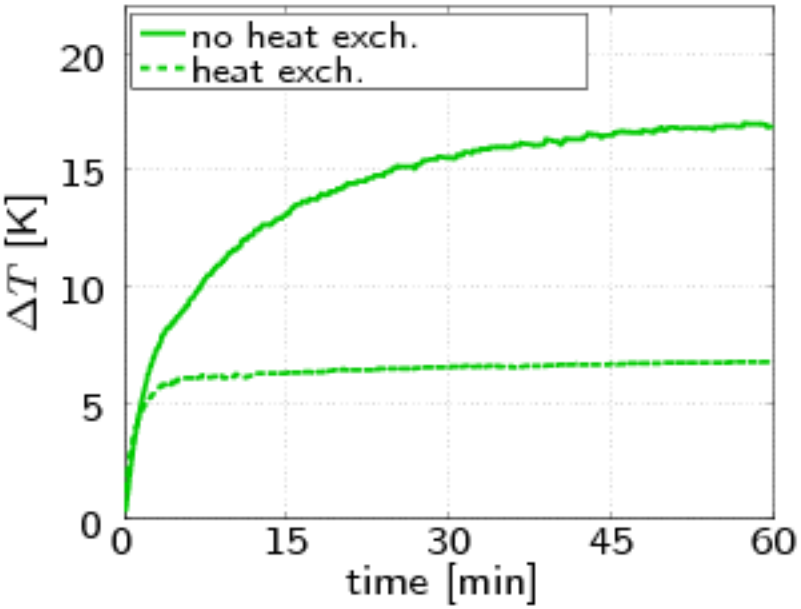

Time-domain modelling

Idea

- Time-domain modelling
  - time varying effects and boundary conditions (BCs)
  - reflections
  - transients

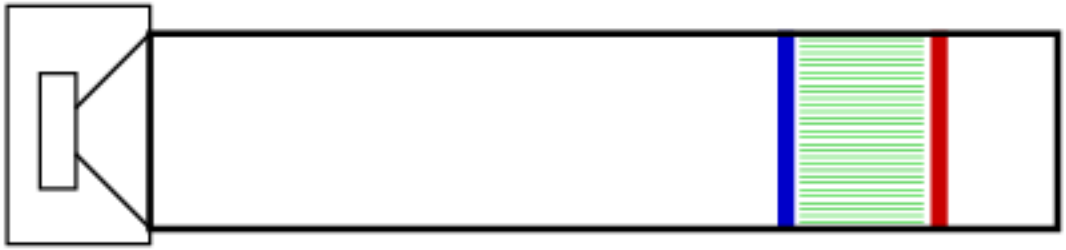

Idea

- Time-domain modelling
  - time varying effects and boundary conditions (BCs)
  - reflections
  - transients
- First idea: A finite difference (FD) method
  - Problem: Too long calculation time

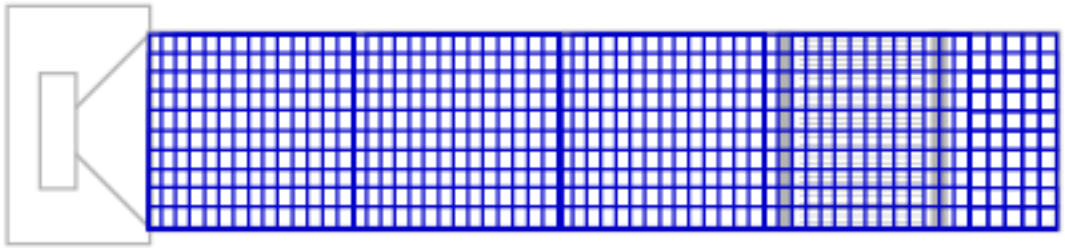

FD

Idea

- Time-domain modelling
  - time varying effects and boundary conditions (BCs)
  - reflections
  - transients
- First idea: A finite difference (FD) method
  - Problem: Too long calculation time
- One solution: Combine FD with the more efficient ESM

Equivalent source method (ESM)

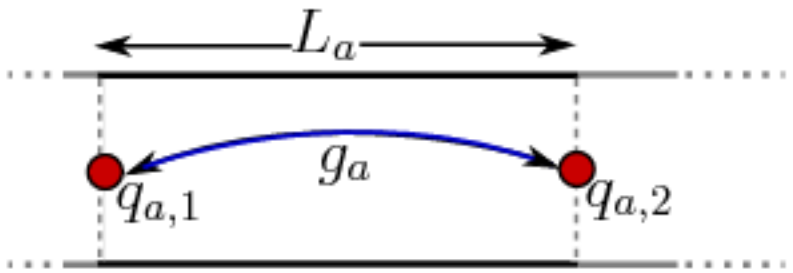

- Sources placed at boundaries
- Adapt source strengths to fulfil BCs.
- Wave propagation described with Green's functions
- Assume
  - plane waves
  - infinite tube

Finite-difference model

Implemented model developed by M. Hamilton, JASA (2002)

Based on finite difference solution of:

- Eq. of continuity $\Rightarrow$ $\partial\rho/\partial t$
- Eq. of momentum $\Rightarrow$ $\partial[\rho u_x]/\partial t$
- Eq. of energy $\Rightarrow$ $\partial e/\partial t$

Finite-difference model: Assumptions

Main assumptions:

- $L_x \sim \lambda$
- $y_0 \sim \delta_\kappa$
- $L_x \gg y_0 \gg$ w
- $\frac{\partial p}{\partial x} \gg \frac{\partial p}{\partial y}$
- $u_x \gg u_y$

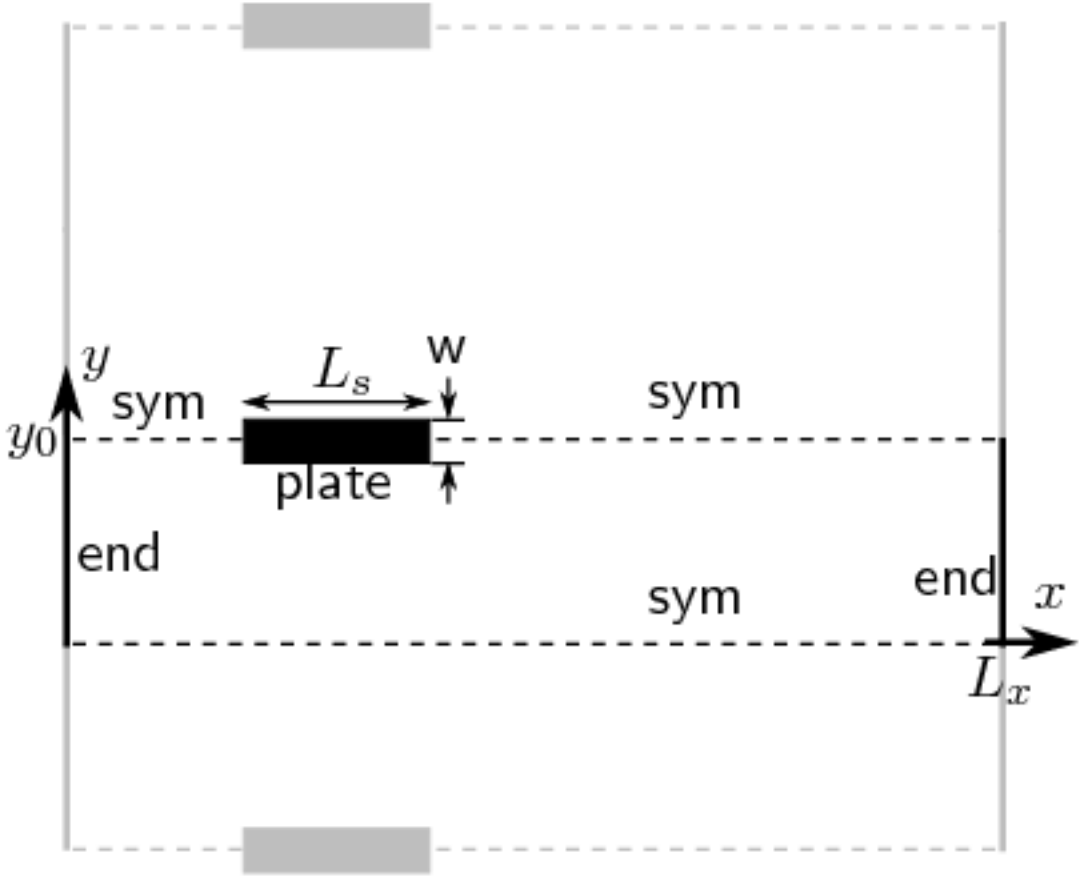

Finite-difference model: Assumptions

Main assumptions:

- $L_x \sim \lambda$
- $y_0 \sim \delta_\kappa$
- $L_x \gg y_0 \gg$ w
- $\frac{\partial p}{\partial x} \gg \frac{\partial p}{\partial y}$
- $u_x \gg u_y$

In model:

- $\frac{\partial p}{\partial y} = 0 \Rightarrow u_y$
- $\frac{\partial [\rho u_y]}{\partial t} = 0$

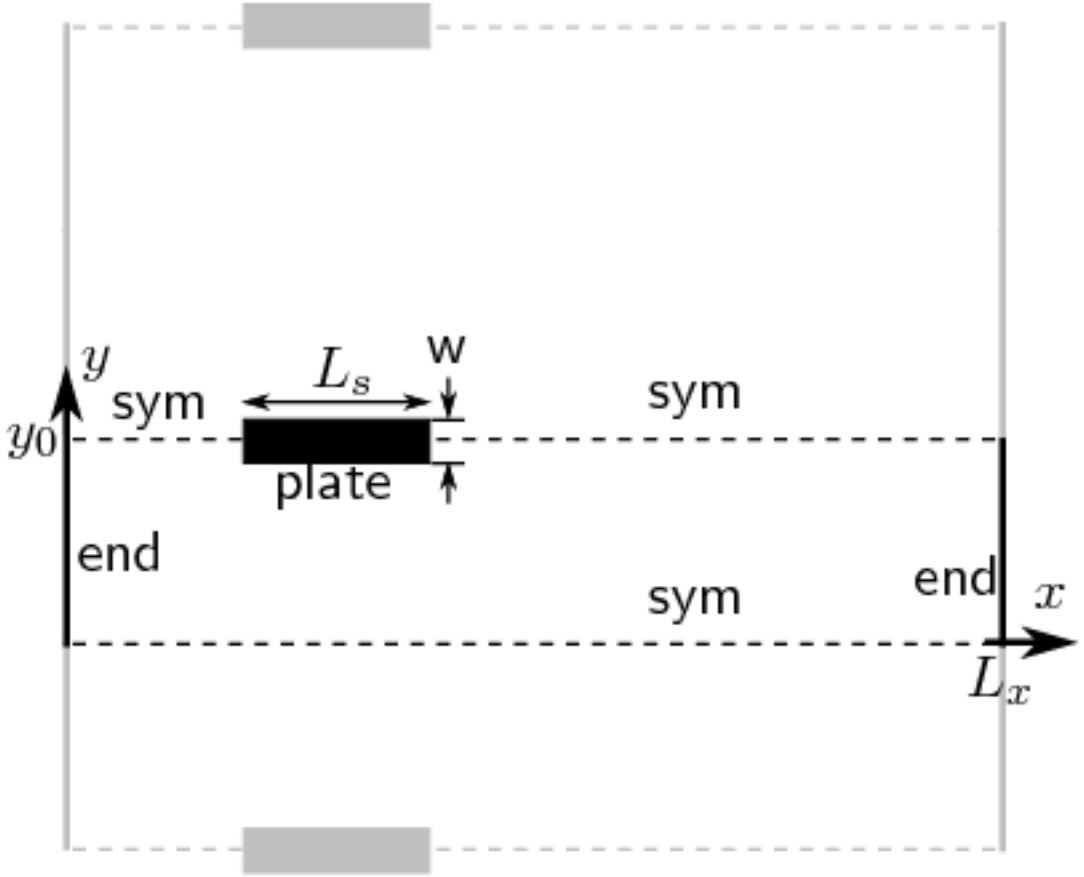

Finite-difference model: Results

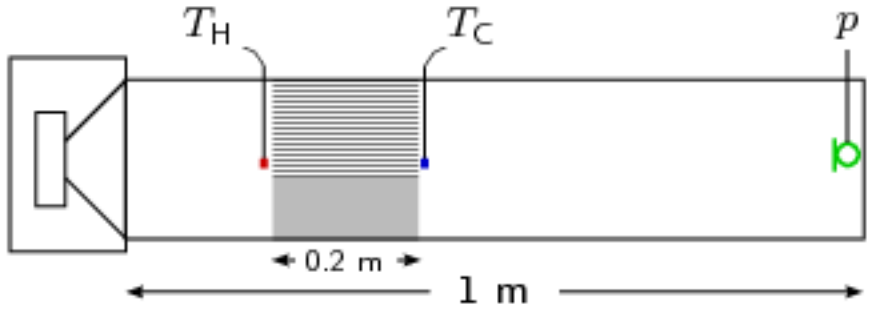

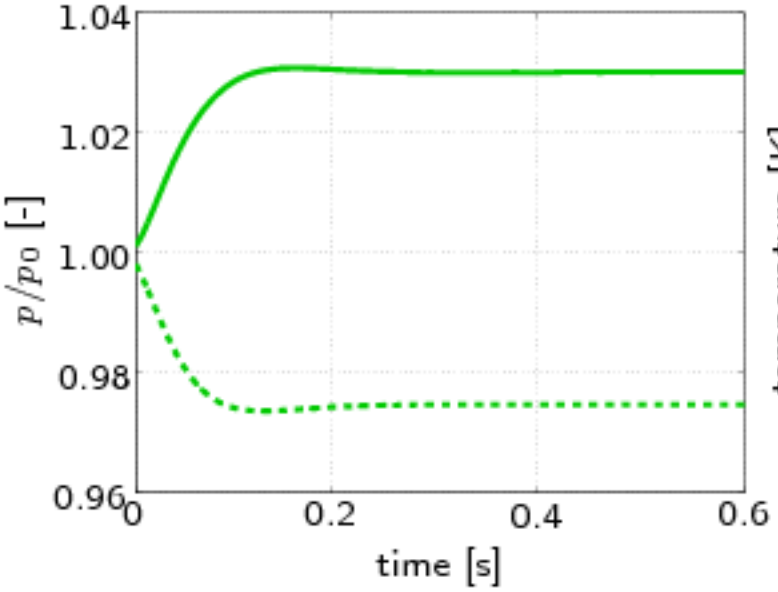

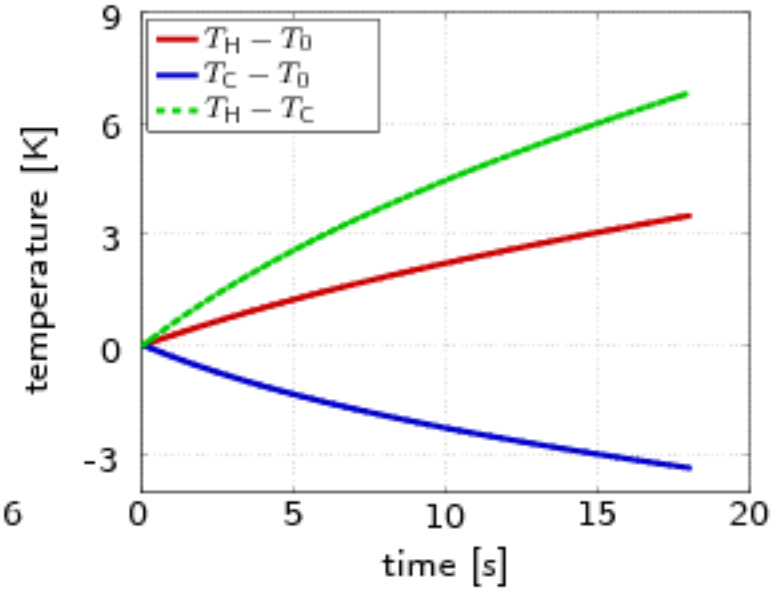

Finite-difference model: Results

- Pressure and temperature in the stack
- 1 δ_κ (0.25 mm) away from the plate
- One acoustic period

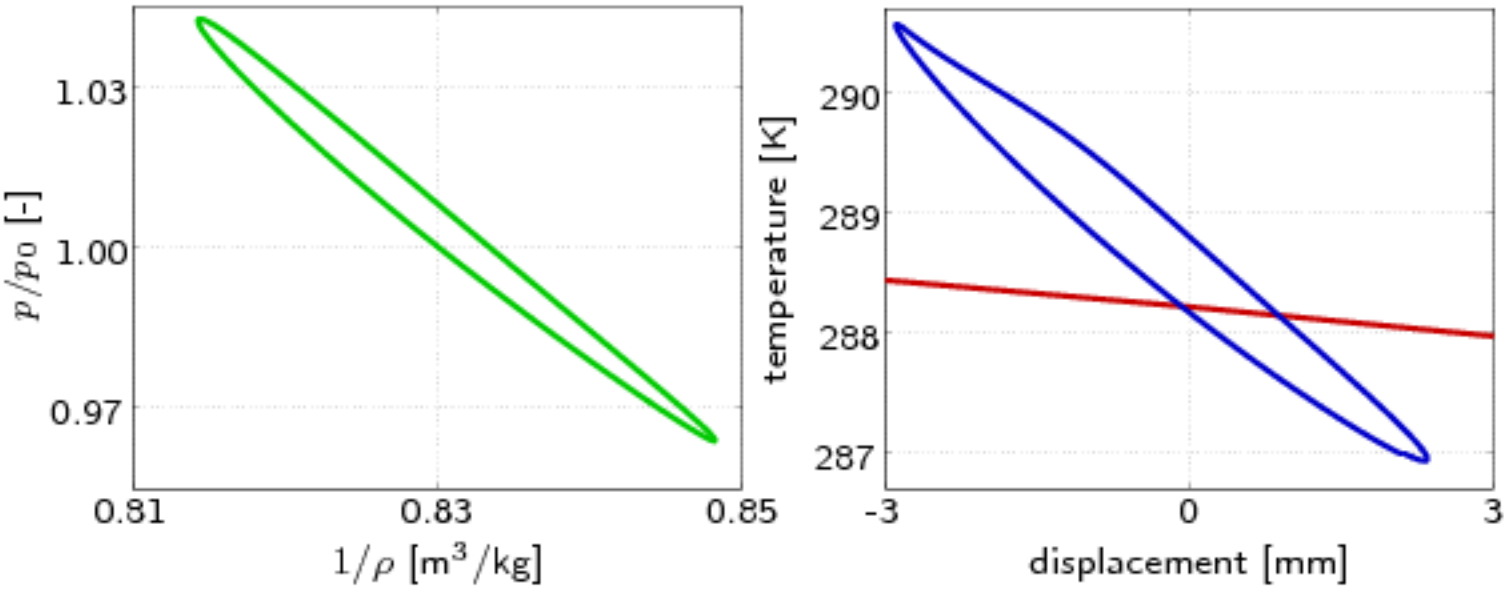

Combining ESM and FD

- Continuity of pressure and volume velocity
- Adiabatic conditions outside the stack

Current status:

- Included:
  - 1-D adiabatic wave-propagation (p, u)
  - different cross section S
  - Lax-Wendroff scheme (same as complete FD)
- Excluded:
  - thermal and viscous effects
- Results:
  - Works within acceptable errors

Conclusions and future work

Conclusions

- experimental setup
  - flexible and functional
  - 6 K/17 K ΔT obtained
  - no measurable cooling power
- modelling
  - thermoacoustic effects included in FD
  - ESM+FD works (adiabatic)
  - computational cost reduced

Future work

- combine ESM with the complete FD model
- validate model by using theory and experimental setup
- study time-varying boundary conditions
- study possibility for active control

Appendix

FD model equations:

$$\frac{\partial \rho}{\partial t} = -\frac{\partial \left[\rho u_x\right]}{\partial x} - \frac{(\rho u_y)}{\partial y} \quad (1)$$

$$\frac{\partial \left[\rho u_x\right]}{\partial t} = -\frac{\partial \left[\rho u_x^2 + P\right]}{\partial x} + \frac{\partial}{\partial y}\left(\mu \frac{\partial u_x}{\partial y}\right) - \frac{(\rho u_x u_y)}{\partial y} \quad (2)$$

$$\frac{\partial e}{\partial t} = -\frac{\partial (e+P)u_x}{\partial x} - \frac{\partial (e+P)u_y}{\partial y} + \frac{\partial}{\partial y}\left(\kappa \frac{\partial T}{\partial y}\right) + \frac{1}{2}\frac{\partial}{\partial y}\left(\mu \frac{\partial u_x^2}{\partial y}\right) \quad (3)$$

$$\frac{\partial T_s}{\partial t} = \frac{1}{\rho_s c_s}\frac{\partial}{\partial x}\left(\kappa_s \frac{\partial T_s}{\partial x}\right) - \frac{\kappa}{\rho_s c_s w}\frac{\partial T}{\partial y}\Big|_{\text{plate}} \quad (4)$$

Long range sound propagation over a sea surface

Brodd Leif Andersson, Karl Bolin, Mathieu Boué, Alex Cederholm and Ilkka Karasalo
KTH - The Marcus Wallenberg Laboratory / FOI - Swedish Defence Research Agency[a)]

(Dated: January 2009)

This paper describes methodology and results from a model-based analysis of data on sound transmission from controlled sound sources at sea to a 10 km distant shore. The data consist of registrations of sound transmission loss together with concurrently collected atmospheric data at the source and receiver locations. The purpose of the analysis is to assess the accuracy of methods for transmission loss prediction in which detailed data on the local geography and atmospheric conditions is used for computation of the sound field. The results confirm that sound propagation predictions are accurate and reproduce observed variations of the noise level as function of time in a realistic way. The results further show that the employed atmospheric model must include a description of turbulent wind to ensure predicted noise levels to remain realistically high during periods of sound shadow.

PACS numbers:

I. INTRODUCTION

In the light of global warming the transition to renewable power sources is a crucial challenge to today's society. A power source that will probably play a major role in the future is wind turbine power. Until now most of the wind turbines are land based, however large offshore farms are under construction or planned all over the world. These will exploit the vast wind resources available in this environment and by 2020 50 GW of installed capacity is planned worldwide[1]. Due to cost increases with increasing water depth, off-shore wind turbines are often situated in shallow waters near a coast, *and are therefore a corcern for causing noise annoyance in coastal areas.* Since atmospheric sound propagation is highly dependent upon the prevailing meteorological conditions, the level of such noise disturbances vary significantly with time.

Measurement of long distance sound propagation over water surfaces have been performed by[2,3] but the meteorological conditions were only measured up to a few hundred meters height. Predictions from this limited meteorological data could be considered insufficient. Knowledge of meteorological conditions (wind velocity, humidity and temperature) further up in the atmosphere would improve the input to prediction models and consequently improve the models' accuracy. Furthermore long distance sound propagation over sea has been measured?

The aim of the present paper is to present measurements of sound propagation at 10 km distance[4] and assess the reliability of predictions the sound transmission with numerical models which use detailed knowledge of the meteorological and geographical conditions, by comparing the numerically predicted transmission loss (TL) with the experimental data.

[a)] Electronic address: kbolin@kth.se

FIG. 1. Map of the Southern Baltic Sea with the Kalmar straight shown by the red square.

II. MEASUREMENTS

The measurements were conducted between the 15:th and the 21:st of June 2005 in the Kalmar strait and the island Öland in the Baltic Sea, see Fig. 1. The measurements were performed in the summer because most annoyance from wind turbine noise could be expected in this season. The source was situated 9 km from the shore on the Utgrunden lighthouse (RT90 coordinates 6249616, 1527939). The receivers were located on the island Öland 750 m from the shore at 7 m above sea level (RT90 coordinates 6251430, 1537445) (see Fig. 2 for the experimental setup). This location was chosen because the facilities available on the lighthouse permitted strong acoustics sources to be mounted and the receiver point was at an appropriate distance from the source.

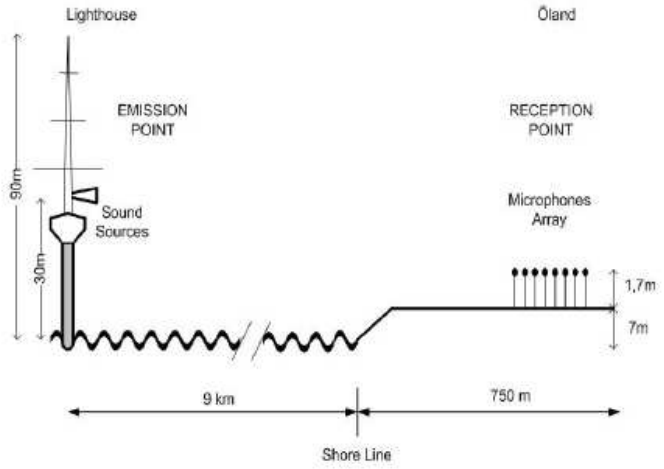

FIG. 2. In situ setup.

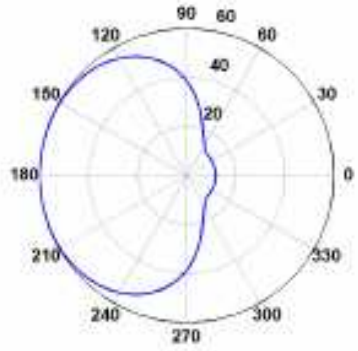

FIG. 3. Directivity of the microphone array for 200 Hz.

A. Acoustical measurements

1. Source location

Two sound sources were mounted on the lighthouse roof at a height of 30 m. The first source was a compressed-air-driven sound source (Kockum Sonics Supertyfon AT150/200 with Valve Unit TV 784). It produced a 10-seconds signal on each occasion. The signal from the source had an average level of 130 dB at the average frequency of 200 Hz. Moreover, the first harmonic, at 400 Hz, was also measured. The siren presented variations of the order of 1% in frequency and about 20 dB in sound level within each signal burst. This alteration were caused by that the compressed air driving the sound source lost pressure during the signal duration. To have a constant and stable sound source and to investigate the behavior of the sound propagation at other frequencies, a second source, consisting of a sound generator coupled to a loudspeaker and a 1.2 m-long resonator tube was used. The loudspeaker produced a 1 minute long signal at 80 Hz giving a constant sound pressure level of 113 dB at 1 m distance. In front of both sources microphones were recording the signals at a 1 m distance. Both sound sources were employed simultaneously.

2. Receiver position

A microphone antenna was designed to increase the signal-to-noise ratio. The receiver point was situated at the houses closest to the shoreline, in a very quiet residential area. Eight -inch microphones were placed on a line parallel to the direction of the source location to create an end-fire microphone array. The microphones were placed at 1.7 m height accordingly to ISO 1996. The distance between the microphones was set to 40 cm to optimize the directivity pattern pointing toward the sound source at 200 Hz. The signals were transmitted through a preamplifier to an UA100 analyzer and then processed in Matlab as explained below. The signals x(t) of the N microphones were added with their respective time delays τ as shown by Eq. (1)

$$s(t) = \frac{1}{N}\sum_{n=1}^{N} w(n)x_n(t-\tau_n) \qquad (1)$$

where $w(n)$ are the binomial coefficients defined by $\frac{N!}{n!(N-n)!}$, N is the total number of microphones,$\tau_n = (n-1)c^{-}1d\cos\phi$ is the time delay of the n-th microphone, x_n the signal recorded by the n-th microphone, d the distance from the source to the microphone, ϕ the angle between the direction of propagation and the direction of the array and c the speed of sound. The directivity patterns for 200 Hz is shown in Fig. 3. When atmospheric conditions were unfavourable, the delay-and-sum beamforming in 1 had to be combined with a frequency tracking algorithm as descibed in[4] (Ch. 4) to ensure detection of the signal against the background noise.

B. Meteorological measurements

1. Source point

The wind speed was measured at 38, 50, 65, 80 and 90 m above sea level on a meteorological mast at the source location. The wind direction was determined with wind vanes at 38 m and 80 m heights. The temperatures were measured at five heights: 6, 38, 50, 65 and 80 m. The relative humidity was measured at 38m height. Data from these sensors were registered at 10 minutes intervals. The average average and standard deviations were recorded during the measurement times.

2. Receiver point

Meteorological profiles at the receiver point were measured several times daily during daytime using radio probes and theodolite tracking of free flying balloons[5]. These measurements were performed by staff from the Department of Earth Sciences, Uppsala University. Wind velocity (horizontal components), humidity and temperature were measured up to 3500 m height.

III. SOUND PROPAGATION MODEL

Two principal requirements on a sound propagation model suitable for the experimental scenario described above are, first, that the model must allow for range dependence in the atmospheric parameters as well as the height of the lower boundary to sea and ground and, second, that it must be able to handle propagation of sound into shadow zones (diffraction effects) since the atmospheric conditions were such that the receiver was in sound shadow during more than 60 % of the trial week. The first requirement is met by both ray tracing and parabolic equation (PE) methods, whereas the second requirement makes ray tracing methods less suitable because they predict the sound pressure to be zero in shadow zones[?] . For this reason, a PE-method was considered appropriate for current application.

A. The GFPE method

The Green's function parabolic equation (GFPE) method was developed by Gilbert an Di[6,7] and later been improved by Salomons[8,9]. The method is particularly designed for atmospheric sound propagation and can use considerably longer range-steps than conventional PE methods. Because of its computational efficiency, the GFPE model was used in this study.

The method computes a 2D field in the rz- plane where r is the radial distance from the source and z is the height. From the 3D Helmholtz equation for the sound pressure, p, in cylindrical coordinates combined with a variable substitution $\phi = exp(-ik_0 r)pr^{1/2}$ two expressions (2) and (3) can be derived[6,8]

$$\begin{aligned}\phi(r+\Delta r, z) = &\exp\left(i\frac{\Delta r \delta k^2(z)}{2k_r}\right)\\ &\times\left[\frac{1}{2\pi}\int_{-\infty}^{\infty}(\Phi(r,k') + R(k')\Phi(r,-k'))\right.\\ &\times exp(i\Delta r(\sqrt{k_r^2 - k'^2} - k_r))e^{ik'z}dk'\\ &+ 2i\beta\Phi(r,\beta)\\ &\left.\times exp(i\Delta r(\sqrt{k_r^2-\beta^2} - k_r))e^{-i\beta z}\right]\end{aligned} \tag{2}$$

where Δr is the horizontal step size, $k(z) = \omega/c(z)$ is the wave number, k_r is a reference wave number ($k_r = k_0 = k(0)$ in this paper[8]). $R(\acute{k}) = (k'Z_g - k_r)/(k'Z_g + k_r))$ is the plane-wave reflection coefficient, Z_g is the normalized ground impedance, $\beta = k_r/Z_g$ is the surface-wave pole in the reflection coefficient and $\Phi(r,k)$ is given by

$$\Phi(r,k) = \int_0^{\infty} exp(-ikz')\phi(r,z')dz' \tag{3}$$

Equations (2) and (3) combined constitute the fundamental step in the GFPE-algorithm. In our implementation the integrals are computed by the midpoint rule, and the propagation factor, first term on the RHS of Eq. (2), is substituted by (4)

$$exp(i\Delta r[k(z) - k_r]) \tag{4}$$

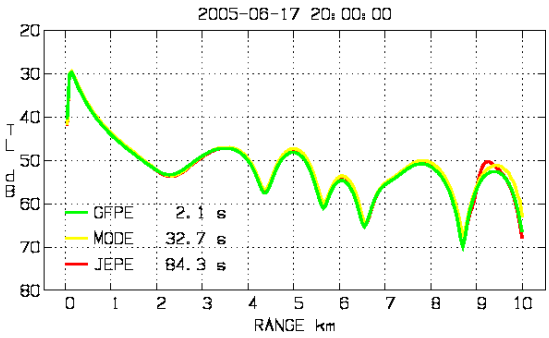

FIG. 4. TL to the sea surface and the ground at 80 Hz as a function of distance to the source. Predictions with JEPE (red), normal mode (yellow) and GFPE (green). The computation times are also shown.

The starting sound pressure profile is a Gaussian function of height z at range $r = 0$

$$\phi(0,z) = k_0^{1/2}\left[e^{-k_o(z-z_s)^2/2} + \frac{Z_g - 1}{Z_g + 1}e^{-k_o(z+z_s)^2/2}\right] \tag{5}$$

where z_s is the source height.

B. Parameter selection/Modifications

The parameters of the GFPE method were selected guided by suggestions in Refs. 6, 8, 9. Thus, the horizontal and vertical step sizes Δr and Δz were set to 10λ and 0.1λ, respectively, where λ is the sound wavelength at the ground, in accordance with recommendations in Ref.8. To suppress spurious reflections from the upper boundary of the computational domain an artificial absorption layer with thickness 75λ was imposed, with absorption parameter A calculated according to Ref.8. The coefficient of attenuation of sound in air was calculated according to ISO/DIS 9613-1[10].

C. Validation

Our implementation of the GFPE model was validated by comparisons with the reference cases considered in Ref.6, and showed perfect agreement with the results published there. To assess the efficiency of the GFPE method and further validate our implementation it was compared to a normal-mode (NM) method and the PE method JEPE[11], in a range-independent approximation of the geometry of the current application and with the atmospheric parameters observed experimentally at 20:00 on June 17. Fig. 4 shows the transmission loss for 80 Hz sound to the sea surface and the ground as function of range computed by the GFPE, JEPE and NM methods, together with the required computation times.

D. Turbulence

Effects of turbulent wind and temperature fields were included in the GFPE model following the approach outlined in Ref.9. Thus, the turbulent components of these fields are modelled as homogeneous random fields with von Karman type horizontal wavenumber spectra. The effect of such turbulence on the GFPE solution is represented by including a random z-dependent phase factor in the GFPE propagator, without requiring explicit computation of a realization of the fields [Appendix I and J] in Ref.9. According to this turbulence model the transmission loss to the receiver is a stochastic variable, and the statistics of the transmission loss were determined by carrying out 50 Monte Carlo runs for each frequency at every hour during the measurement period.

E. Atmospheric/Meteorological assumptions

Meteorological input to the GFPE model were both the balloon measurements (horizontal wind velocity), radio balloon (relative humidity and temperature) and the anemometers on the mast (standard deviation of wind speed). The balloon measurements were used as meteorological parameters for the stationary parameters $(\mathbf{U}(z), rh, T, p)$ while the mast data were used to estimate the turbulence intensity. Linear interpolation was used between measurement points in the vertical direction as well as in time.

IV. RESULTS

As previously stated the objective of the paper is to investigate the accuracy of numerical predictions of the transmission loss compared to measurements. The results are shown in figures 5 and 9 using an atmospheric model without and with turbulence, respectively.

A. Turbulence excluded

The black diagrams in Fig. 5 show the simulated TL, the average values during measurement periods are shown as green lines. Measured TL are shown as red dots and average values are shown as yellow lines. A dotted red line shows the TL calculated by the recommendations from Ref.12 with the transition point between spherical and cylindrical spreading at 700 m distance from the source. The Dn values shown in the lower left corner are normalized differences between measured and predicted TL. These are defined as the average difference between measured and predicted TL divided by the measurements' standard deviation at each day. It can be clearly seen that the prediction shows larger differences in TL than the measured results. The cases with high TL show good agreement with the measured TL. However, the periods where the measured TL is low are are severely underestimated by the predictions. The low TL values occur when the sound speeds are monotonically or

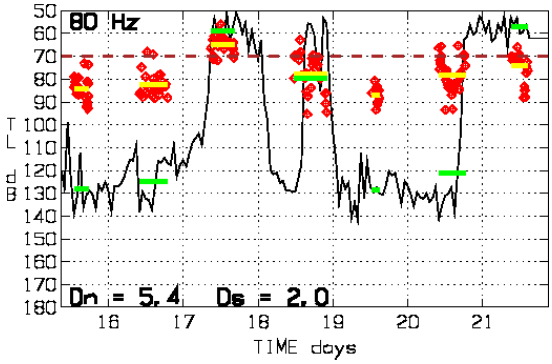

(a) 80 Hz

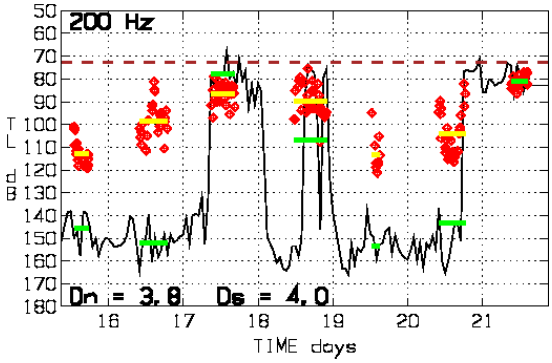

(b) 200 Hz

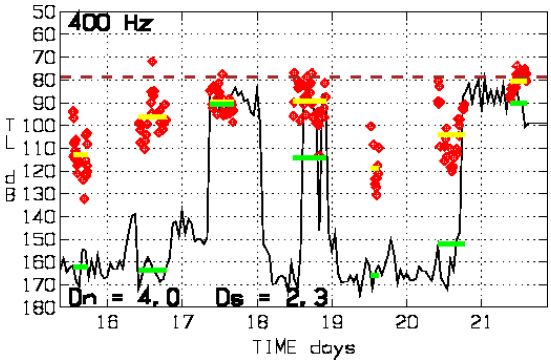

(c) 400 Hz

FIG. 5. Measured and predicted TL for the laminar simulation.

nearly monotonically decreasing with increasing height. The emitted sound is then refracted upwards and shadow zones occur by the receiver location. A typical occasion showing this condition is shown in Fig. 6. The high TL values occur when the sound speed has a local maximum at relatively low height (for instance caused by a low level jet[5]). Such meteorological conditions were prevalent e.g. during the afternoon of June 17. At these circumstances the sound is refracted downwards and trapped within a channel restricted by the local wind maximum as can be seen in Fig. 7.

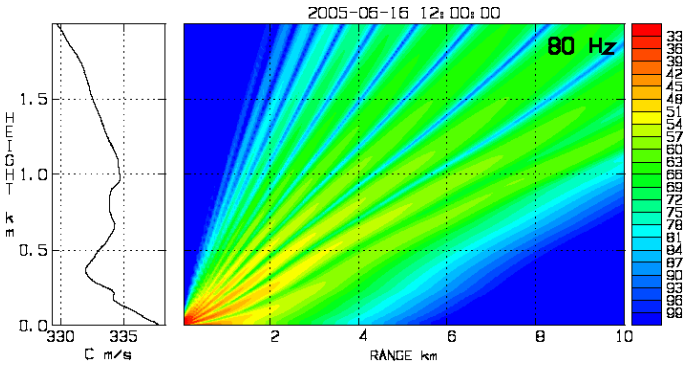

FIG. 6. Sound speed profile (left figure) and simulated 80 Hz sound field (right) at 12 am the 16 June. Upwards decreasing sound speed can be observed. The shadow zone at the receiver location is also clearly seen.

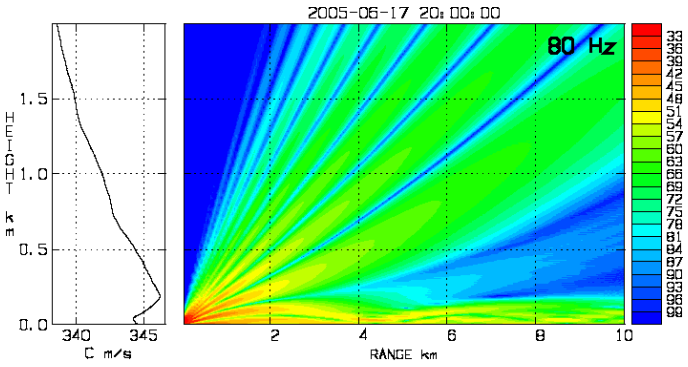

FIG. 7. Sound speed profile (left figure) and simulated 80 Hz sound field (right) at 12 am the 17 June. A local maximum of the sound speed can be observed at 200 m height. The sound channel below the local maximum can be observed at the low heights in the right figure.

B. Turbulence included

Simulations including a turbulent field were observed in Ref9 to decrease the amount of refraction, especially in the upward refracting case. In Fig. 8 the turbulence has been included in the sound speed profile used for the Fig. 6. The difference between the sound fields is mainly that the shadow zone is less pronounced for the sound field in a turbulent atmosphere. In Fig. 9 the simulations including turbulence are shown. The thick black diagram shows the average value of the TL from the Monte Carlo simulation and the thinner black lines surrounding these show the interval of the standard deviations, thereby showing the sensitivity of the predicted TL with respect to small disturbances in the wind field. Other symbols in the figures are defined as in Figs. 5. Comparing Fig. 5 and Fig. 9 it can be seen that the most prominent effect of turbulence on the predictions is a significant decrease of the TL during periods of sound shadow at the receiver. This is explained by the random scattering of the sound by the turbulence-caused random inhomogeneities in the sound-speed, leading to an increased sound propagation into the shadow zones. As seen in the figures and indicated by the

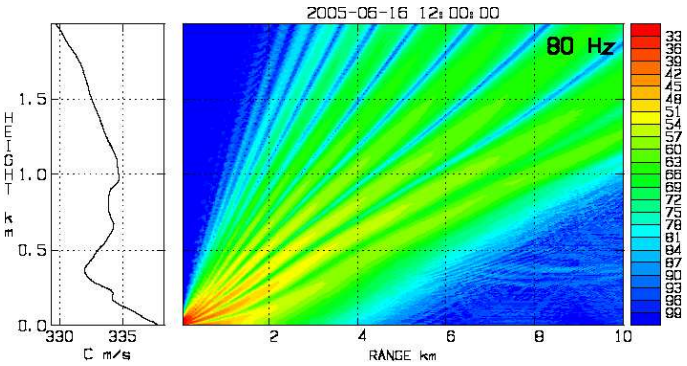

FIG. 8. Sound field shown as TL of the 16:th June at 12 am including turbulent wind field.

Dn values shown, the agreement between the model predicted and the experimentally observed transmission loss has thereby is significantly improved by including effects of turbulence in the predictions.

V. DISCUSSION/ CONCLUSION

The results support that sound propagation modelling including effects of detailed meteorological data can be used for reliable prediction of transmission loss. In particular, the predicted TL remains reasonably accurate under varyning meteorological conditions, and follows the variations observed in the TL measurements in a realistic way. The results further indicate that the sound propagation model must include effects of turbulence in the atmosphere for accurate predictions of the TL into shadow zones.

It should be noted that the largest remaining differences between measured and predicted (including turbulence) TL can be observed around noon and early afternoon at the 16:th and 20:th. This could probably be explained by the higher turbulence intensities around these times[13] compared to other times during the day. The high turbulence levels would cause the balloon measurements to deviate further from the assumed laminar flow. However, turbulence intensities are quite weak over sea surfaces and therefore this would probably not affect the results to a large extent. Furthermore the inertia of the balloon would also reduce the influence of the smallest eddies. Most important eddy sizes around wavelength[9] (0.8-4 m) some influence due to balloon's inertia should be possible/probable in this range.

VI. ACKNOWLEDGEMENTS

The authors wish to thank Prof. Sten Ljunggren, Dr. Hans Bersgström and Civ. Ing Hans Olsson for helpful comments and discussions. The Swedish Energy Authority is ackowledged for its financial support through the Vindforsk II program.

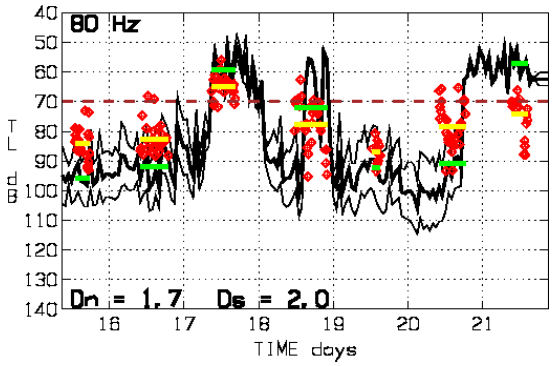

(a) 80 Hz

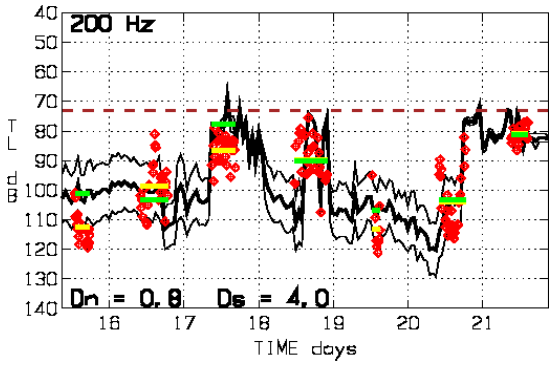

(b) 200 Hz

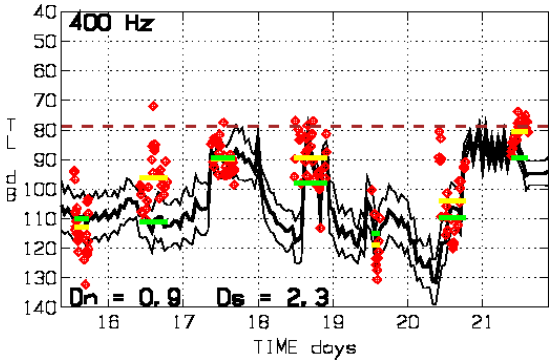

(c) 400 Hz

FIG. 9. Measured and predicted TL for the turbulent simulation.

[1] E. W. E. Association, "Ewea's response to the european commission's green paper", Technical Report, (COM (2006) 275 Final) (2007).

[2] Z. M. K. Konishi, Y. Tanioku, "Long time measurement of a long range sound propagation over an ocean surface", Applied Acoustics **62** (2000).

[3] Z. M. K. Konishi, "Interpretation of long term data measured continuously on long range propagation over sea surfaces", Applied Acoustics **62** (2001).

[4] M. Boué, "Long-range outdoor sound propagation over sea, applications to wind turbine noise", Technical Report TRITA-AVE 2007:22, KTH (2007).

[5] K. Törnblom, "Thermally driven wind modification in coastal areas and its influence on sound propagation with application to wind power", Technical Report, Department of Earth Sciences, Uppsala University (2006).

[6] K. E. Gilbert and X. Di, "A fast green's function method for one-way sound propagation in the atmosphere", Journal of the Acoustical Society of America **94**, 2343–2352 (1993).

[7] X. Di and K. E. Gilbert, in *Proceedings of the Fifth International Symposium on Long Range Sound Propagation*, 128–146 (Milton Keynes, England) (24-26 May 1992).

[8] E. M. Salomons, "Improved greens function parabolic equation method for atmospheric sound propagation", Journal of the Acoustical Society of America **104**, 100–111 (1998).

[9] E. M. Salomons, *Computational Atmospheric Acoustics* (Kluwer Academic Publishers) (2002).

[10] International Organization for Standardization, Geneva, Switzerland, *ISO/DIS 9613-1: Attenuation of sound during propagation outdoors- Part 1: Atmospheric absorption* (1995).

[11] I. Karasalo and A. Sundström, "JEPE - a high-order PE-model for range-dependent fluid media", in *Proc. 3rd European Conference on Underwater Acoustics*, 189–194 (Heraklion, Crete, Greece) (1996).

[12] Naturvårdsverket, "Ljud från vindkraftverk", Technical Report 6241, Naturvårdsverket, Sweden (2001).

[13] H. Panovsky and J. Dutton, *Atmospheric Turbulence* (John Wiley & Sons, New York) (1984).

Modeling of transient wave propagation in Comsol

Anders Løvstad, IET, NTNU

Abstract

This paper evaluates the use of simple exponential damping layers as perfectly matched layers (PMLs) for transient wave propagation analyses in Comsol Multiphysics v.3.5, as time domain implementation of PMLs presently is unavailable. Dispersion curves for the fundamental transversal mode are calculated, in addition to error estimation in time-space plots.

Introduction

Conventional methods such as point-to-point measurements using pulse-echo techniques are used successfully to monitor structures locally at high accuracies. However it is a slow process, which becomes expensive when larger areas are to be inspected. By employing guided wave techniques, longer ranges can be inspected as complete coverage of the waveguide is enabled. Inaccessible areas can be reached, as guided waves can propagate within the structure even if it is buried, coated, fluid filled or located subsea.

Guided waves consist of multiple independently propagating modes, existing in smaller or larger extent in the waveguide. With a few exceptions all modes of propagation are dispersive, i.e. the velocity is frequency dependent. Despite careful excitation of a wanted mode, other modes can also appear as a wave propagates through refraction at boundaries or from interaction with discontinuities or defects [1].

For simple geometries like plates and cylinders, analytical expressions exist for calculation of dispersion curves [2]-[4]. However, with more complicated geometries this is not the case, and employment of Finite Element (FE) software is then useful for simulation and evaluation of physical properties of the structure as defect detection and location. This paper discusses a few challenges with time domain calculations in Comsol Multiphysics [5]. To obtain dispersion curves using a time domain approach, signals at two points are obtained and FFTs are subsequently carried out to evaluate in the wanted frequency range. A problem arises as perfectly matched layers (PML) are not available in the time domain in Comsol, so an ad hoc approach for creating a PML is performed and evaluated.

Dispersion relations

The dispersion relation of a medium is determined from the phase spectrum of the propagating pulse as

$$\beta(\omega) = L^{-1}\left(\varphi(\omega) - \varphi_0(\omega)\right) \tag{1}$$

where L is the distance between two measurement points and φ denotes the phase spectrums. The phase velocity can then easily be found [6] as

$$v_{ph}(\omega) = \frac{\omega}{\beta(\omega)} = \frac{\omega L}{\varphi(\omega) - \varphi_0(\omega)} \tag{2}$$

As the main concern of this paper is to evaluate simple custom implemented perfectly matched layers in the time domain, only the fundamental transversal mode, A_0, is investigated. If the time

signal is composed of a number of propagating modes, a two-dimensional FFT of waves received at equally spaced positions along the structure must be performed, as described by Alleyne and Cawley [7].

Time stepping and meshing

A simple plate with dimensions similar to typical cross sections of a pipe wall is chosen as example structure. The plate is excited with prescribed transverse displacements, as shown in figure 1.

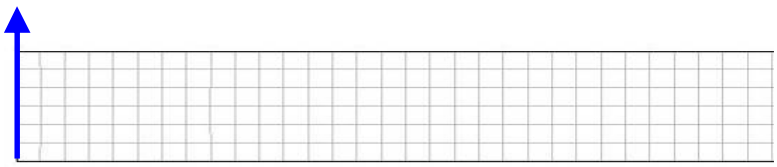

Figure 1: Transverse excitation. Thickness of the pipe wall is 11 mm.

A Ricker pulse is used as excitation signal, with a central peak at 100 kHz and delayed 1e-5 seconds. The Ricker is uniquely specified through its peak frequency. With the time delay, t_0, included, the Ricker is mathematically given as

$$R(t) = \left(1 - 2\pi^2 f_0^2 (t - t_0)^2\right) \cdot e^{-\pi^2 f_0^2 (t-t_0)^2} \tag{3}$$

Sufficient temporal and spatial resolution of the model is critical for its convergence. By applying the minimum time step criterion proposed by Moser et. al. [8]

$$\Delta t \leq 1/(20 f_{\max}) \tag{4}$$

a time step of 1e-7 seconds accounts for frequencies up to 500 kHz. A quadratic mesh is employed throughout the calculations, with a maximum element size of 4 mm, as depicted in figure 1. Comsol Multiphysics recommends a minimum of 5 nodes / λ, while more than 10 nodes / λ are proposed in [7]. Thus the spatial resolution limits the obtainable resolution to a larger extent than the temporal resolution.

Comsol recommends generalized-α [9] solver when solving transient problems with the structural mechanics module (SME). A problem arises when results are exported to MatLab for post-processing as the solver occasionally performs two calculations at the same time step. The time vectors thus consist of uneven time steps and an FFT cannot be performed. The duplicate values must be deleted in post processing.

Perfectly Matched Layers (PML)

Reflections from impedance steps at model boundaries affect calculations unless they are taken properly care of. This is commonly done by various implementations of perfectly matched layers (PML). However such layers are not available in the time domain in Comsol, i.e. for transient analysis and calculations. An ad hoc approach to obtain suitable PMLs is to use damping layers at model boundaries, typically increasing quadratically or exponentially with distance. If the damping increase to rapidly with distance, the damping layer will be seen as an impedance step by the incoming wave, while to slowly increasing damping results in reflections from the end wall.

PML length of >3λ at the peak frequency is chosen as limit requirement. As this relates the length of the PML to the frequency content of the signal, the exponential damping is simply scaled by the damping factors so that they are equal at the boundary, i.e.

$$\alpha_{dM}\left(x - x_{boundary}\right)e^{Lx} \quad \text{and} \quad \beta_{dK}\left(x - x_{boundary}\right)e^{Lx} \tag{5}$$

Results

The resulting phase velocity for the A0 mode is calculated using both the quasi PML approach, and the dummy solution of a semi-infinite structure, as can be seen in figure 2. The results can be seen to be very similar. Using a finer mesh results in more accurate results at high frequencies, as the mesh captures shorter wavelengths.

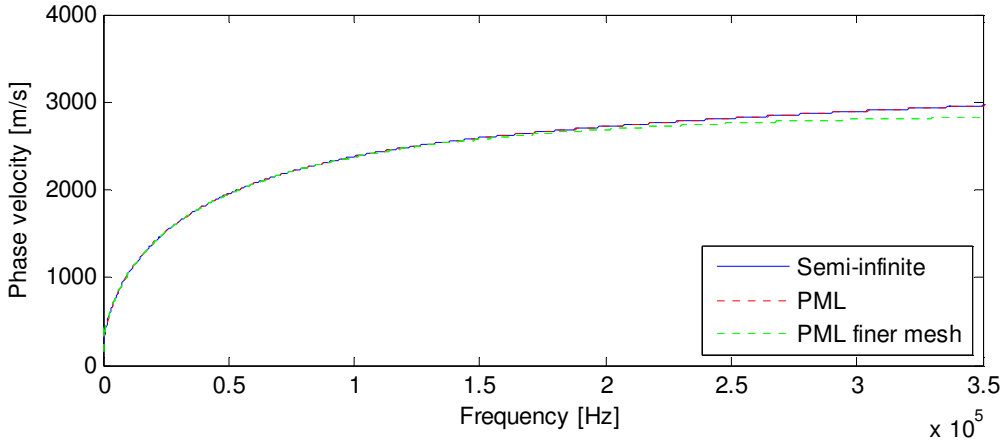

Figure 2: Phase velocity of A0 mode.

Time-space diagrams show the wave propagation and attenuation as the wave propagates along the structure and into the damping region. Figure 3 show the amplitudes (normalized) of a) the structure with PML, and b) the semi-infinite implementation. The black line marks where the PML begins when it is present. As can be seen, the propagation is dispersive, as the wave packet spreads out in time. The PML can be seen to damp the signal out within its length.

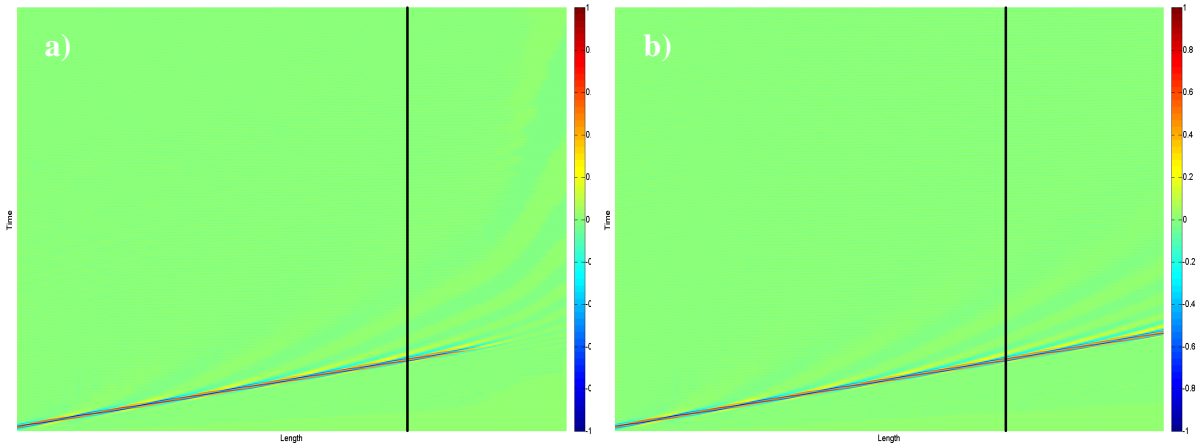

Figure 3: Time-space diagram of wave propagation; a) PML b) Semi infinite.

By subtracting the amplitude levels of the PML solution from the semi-infinite one, the calculation error is obtained. Errors are found to be in the range of 1:1e-4 compared with the amplitude levels of the incident waves to the PML. Figure 4 shows resulting error level, scaled by 1e-3 and 1e-4 relative to the incident amplitude in plot a) and b), respectively.

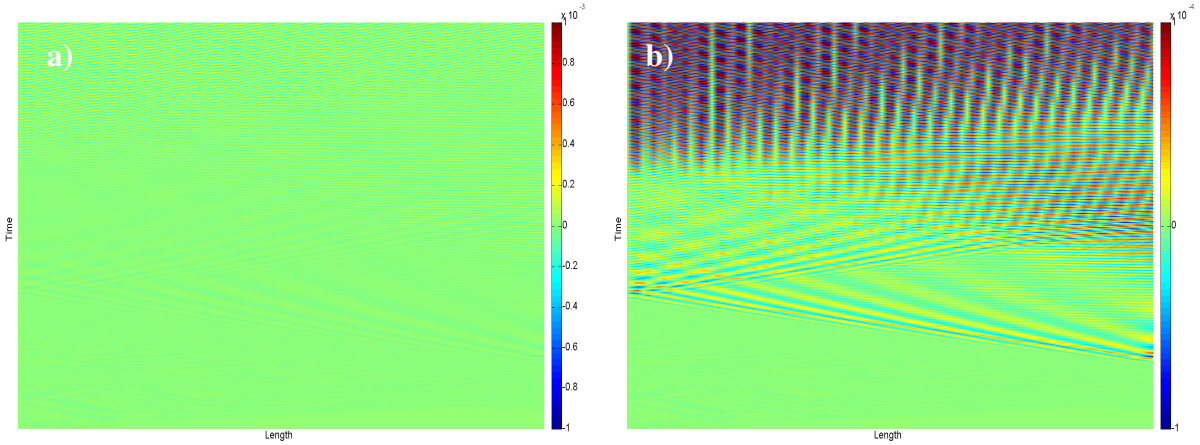

Figure 4: Time-space diagram of wave propagation; a) Scaled by 1e-3 b) Scaled by 1e-4.

Results

As time domain PML implementations are not available in Comsol Multiphysics, the ad hoc approach described above seems to give reasonably good results, despite not being optimized to any larger extent. Accurate dispersion curve was calculated for the A_0 mode with use of the procedure.

References

[1] Lowe, Alleyne and Cawley, "The Mode Conversion of a Guided Wave by a Part-Circumferential Notch in a Pipe", J. Appl. Mech 65, 1998, 649-656.

[2] Lamb, "On waves is an elastic plate", In Proc. R. Soc. London, Ser. A, 1917, p. 114-128.

[3] Viktorov, "Rayleigh and Lamb waves", Plenum Press, New York, 1970.

[4] Gazis, "Three dimensional investigation of the propagation of waves in hollow circular cylinders. I. analytical foundation.", J. Acoust. Soc. Am. 31, 1959, p. 568-578.

[5] Comsol Multiphysics, v.3.5, 2008.

[6] Sachse and Pao, "On the determination of phase and group velocities of dispersive waves in solids", J. Appl. Phys. 49 (8), 1978, p. 4320-4327.

[7] Alleyne and Cawley, "A two-dimensional Fourier transform method for the measurement of propagating multimode signals", J. Acoust. Soc. Am. 89 (3), 1991, p. 1159-1168.

[8] Moser, Jacobs and Qu, "Modeling elastic wave propagation in waveguides with the finite element method", NDT&E International 32, 1999, p. 225-234.

[9] Chung and Hulbert, "A Time Integration Algorithm for Structural Dynamics With Improved Numerical Dissipation: The Generalized-α Method", J. Appl. Mech. 60, 1993, p. 371-375.

Invited talk at 32th Scandinavian Symposium on Physical Acoustics
Finse Norway, 8-11 February 2009

Parametric acoustic arrays 50 years!
A personal account, with viewpoint: Bergen, Norway

Halvor Hobæk

Department of Physics and Technology

University of Bergen

halvor.hobak@ift.uib.no

Introduction

I have chosen this topic for the talk since this is probably my last chance to tell the history, and since my academic career is closely related to the parametric acoustic array. The parametric acoustic array represents a turning point in the interest for nonlinear physical acoustics world wide, and therefore has a strong impact on the evolution of acoustics in general. My intention is to tell the story from my personal viewpoint, not the least because it also has had a great influence on the activity in acoustics at the University of Bergen, and therefore also on the acoustics community in Bergen more generally. The story is, of course, incomplete. It is not possible to include everything that happened in these 50 years. My personal engagement in the field was only for the first 20 years. I must apologize to those who contributed to the field which I have not included, like for example parametric arrays in air. I have concentrated on activity directly influencing my own work. Therefore, the bibliography is far from complete.

Some of you may be unfamiliar with the concept of parametric acoustic arrays. I shall not start by defining it, but it will become clear in a while what it is about. I also shall try to avoid equations – even if I shall not resist the temptation completely.

Prehistory

I shall start a little time before the parametric acoustic array enters the scene. The history of nonlinear acoustics can be traced back to the time of Euler and Lagrange, but the modern evolution started in the 1950s. There were two dominating centers of such activity: USSR (Moscow State University) and USA (Brown University at Rhode Island). In the Sovjet names like Burov, Krasil'nikov, Zarembo, Zverev, Kalachev, Gol'dberg (does the Goldberg number sound familiar?), and later Naugol'nykh, Soluyan and Khokhlov comes to my mind, and in USA in particular Eckart, Westervelt and Beyer, among others. Robert Beyer, in addition to being a very clever experimentalist, also did a great job as a translator from Soviet journals.

In 1956 Ingard and Pridmore-Brown at MIT [1] performed an experiment on nonlinear interaction of two highly directional sound beams crossing each other perpendicularly, and found that sound actually was present at the difference frequency, the frequency which is the difference between the two original ones. Shortly after this Westervelt published theoretical results [2,3] concluding that outside the interaction region no sound due to the interaction should be detected. This caused a controversy which to this day has not been completely settled – I heard Westervelt argue about this as late as in 1995, in spite a lot of experimental evidence to the contrary. Some simple arguments

may be of interest here: Two conditions must be fulfilled in order to obtain constructive nonlinear interaction. In addition to the simple relation between the generated and the original frequencies, also the wave-vectors must correspond. Since they are vectors, and their lengths are proportional to frequency, this cannot be fulfilled unless the medium is dispersive if the original waves propagate perpendicularly to each other. However, in an experiment perfect collimation will not be achieved, and the possibility of constructive interaction still remains. Anyway, this controversy excited a lot of attention.

Enter the parametric array

Then, in 1959, Westervelt launched the idea of the parametric acoustic array [3], by aligning the two sound beams of different frequencies along the same axis. This concept was presented at an ASA meeting in 1959, and concluded with an expression for the difference frequency directivity in terms of a function formally related to the Rutherford scattering formula for electrons scattered by an atomic nucleus. Of course this was exciting! Moreover, he referred to this as being confirmed by experiments by Beyer and colleagues.

Avoiding formulas the concept may be described as follows. Westervelt assumed two well collimated, high frequency, axially aligned sound beams propagating in the same direction. The beam diameter was assumed to be less than the wavelength of the difference frequency, so in practice the primary sound beams were like confined to a line ("pencil beam"). The high frequency primary waves become absorbed, and after some distance (the array length) they disappear. Before this they interact nonlinearly, and generate a wave of difference frequency, which is able to propagate much further. This wave acquires a directivity much higher than one should expect from the narrow beam diameter. Instead, it is determined by the length of the interaction region, which may be much larger than the difference frequency wavelength.

The details were published quite some time after: The experiments by Bellin and Beyer [5] in 1962, and the theory by Westervelt [6] in 1963. By the way, the notion of "Parametric Acoustic Arrays", or "Parametric End-Fire Array" as Westervelt first introduced, may need some explanation. The phrase Parametric comes from an electromagnetic analogy. In microwave technology a certain amplifier type was well known, based on using a high energy high frequency wave as a pump wave together with nonlinear elements like capacitors in a waveguide to amplify a weak wave by frequency conversion as the waves propagate. Such devices were called Parametric Amplifiers.

At this time Sigve Tjøtta enters the scene. He had spent a year at Brown University before coming to Bergen about 1960, with a keen interest i nonlinear acoustics, which also was the topic of his doctor thesis [7]. He soon took up the idea of Westervelt and wanted to develop the theoretical description in full detail. Typical of his approach was a clear analysis based on fundamental equations, and a complete evaluation of the unavoidable approximations made. Together with Viggo Lauvstad he presented the first results [8] already in 1963 – in the same issue of JASA as Westervelt's paper was published - and a more developed paper [9] came in 1964.

Note also the third author in the last paper: Jacqueline Naze. At this time she was a post. doc. at the institute of Applied mathematics, with plasma physics as a speciality. Sigve had started a research group in plasma physics while building up the institute, and attracted several researchers and master students. More on plasma physics below. Anyway, Jacqueline was soon to become Sigve's wife, and they were later to be known as a leading team in non linear acoustics. However, it took many years before Jacqueline actually switched to acoustics after this brief interlude.

In this paper they derived the governing equations describing the parametric acoustic array more rigorously than Westervelt did, and applied them to different models, among which were collimated plane primary waves, not restricted to Westervelt's «pencil beams» or «line array». The directivity then turned out to be even higher, because the effect of the finite aperture on the difference frequency was included! They also calculated for a model where the primary beams were interacting only in their far field. Results from their analysis of collimated plane beams were also published[10] in a short communication in JASA in 1965.

Some basics

So far I have not mentioned much about the physics behind the parametric acoustic array. It is not time to go in much detail either, but certain facts need to be established. Basically we need two high power sound beams radiated from the same source, or at least so that most of the beams overlap in space. At high power the nonlinearity of sound propagation causes the waves to deform: if they are initially sinusoidal they deform to sawtooth-like shape. This can be expressed as if energy is transformed from the fundamental wave to higher harmonics. If two primary frequencies are present also combination frequencies appear, like difference frequency and sum frequency. Since the absorption coefficient of sound is proportional to the frequency squared, the higher harmonics and the sum frequency become absorbed even faster than the primary frequencies, but the difference frequency may propagate further than the primary waves. Thus, this arrangement acts like a sound source for the difference frequency. However, the efficiency is rather low since most energy disappear to the higher harmonics.

One way to describe this is as if the beam volume consists of virtual sources, and the resulting field can be obtained by summing the contribution of these. The phase of the virtual sources propagates with the sound speed, and accordingly constructive interference exists in the beam direction. One may thus regard this as an extended source, phased to radiate along its direction, what in radio antenna theory is called an «end-fire array».

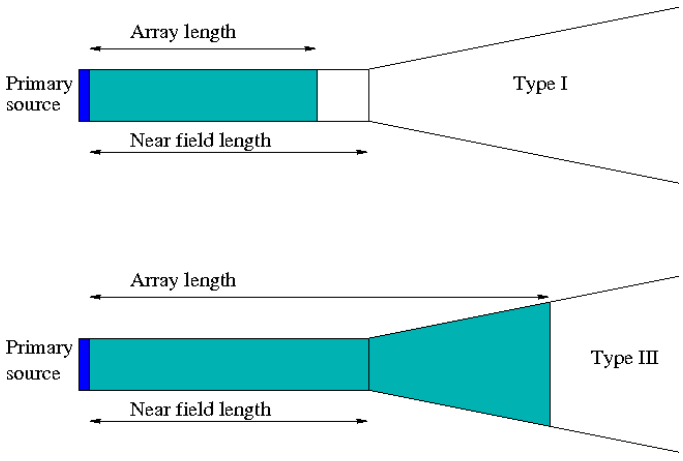

Figure 1: Two of the basic types of parametric arrays

The length of the array may be long compared to the difference frequency wavelength, and therefore a high directivity may be obtained, even if the beam diameter may be less than the wavelength. The length of the array depends on absorption. The phase of the primary waves changes by □/2 as one passes from the near-field to the far field. This does not affect the phase of the virtual sources for the difference frequency (but it does for the sum frequency and second harmonics!). But in the farfield the wavefront curvature induces a phase shift between contributions from the beam centre and the beam edge. The result is a less efficient conversion than in the nearfield, and it also effects the directivity pattern. We shall refer to arrays with main interaction in the farfield as "Type III" arrays, while "Type I" are those with interaction only in the near-field. The original pencil beam Westervelt type is Type II. The difference between the two main types of parametric arrays is illustrated in Figure 1.

First experiment in Bergen

In want of experimental confirmation Tjøtta wished to encourage measurements to be made on parametric arrays. This is where I enter the scene. At this time the University of Bergen was quite young – barely 15 years old. At the Physics Department - actually 3 sub-departments - the research activity was rather limited: nuclear physics, high energy particle physics (CERN activity), cosmic rays and ionospheric physics, theoretical physics (nuclear, atomic) and plasma physics. The latter was largely unknown to most students. Due to lack of space at the institute they had to rent rooms at Institute of Marine Research about half an hour walking distance away. I was about to finish my bachelor degree in 1963, and succeeded to get a job as a technical assistant in the Plasma physics group, planning to proceed with a master thesis. However, already in 1964 it was decided to dismantle the experiment and move it to the Norwegian Technical University in Trondheim. So, I had to find a new project for my further studies, and thus became an easy target for Tjøtta, who perhaps felt to some degree a responsibility for the closure of the plasma physics group. By the way, theoretical plasma physics has been a main activity at Institute of applied mathematics in Bergen since then, almost to these days.

It was a slow start. The Institute of Mathematics had no experimental facility to offer. Professor Trumpy, the head of the Physics department, showed no interest in starting a new activity in acoustics. I approached the physics department at University of Oslo, with the same result. Also the people at Norwegian Underwater Defense Research institute in Horten turned me down. And I don't blame these people. Here comes a prospective master student with no previous experience in acoustics and wants to start an experiment in almost un-thread grounds?

To make the story short: Tjøtta and Trefall (newly appointed professor in cosmic physics at Department of Physics) joined forces, applied to the University council for funding, and got it! NOK 15 000 was made available (the present day equivalent is about NOK 250 000). Professor Trefall was about to expand his department, and I was to build up the tools necessary to perform the experiment. From scratch! Both Tjøtta and Trefall were to act as supervisors.

Soon after, Jacqueline and Sigve Tjøtta, on their honey-moon, were subject to a serious car accident. They just barely survived, and it took several months for recovery. They had left me with the report from 1963 and a preprint of their new article (1964). For me, with only a general physics students knowledge of acoustics, this was tough material to penetrate. Luckily, I also had Bellin and Beyer's experiment to rely on.

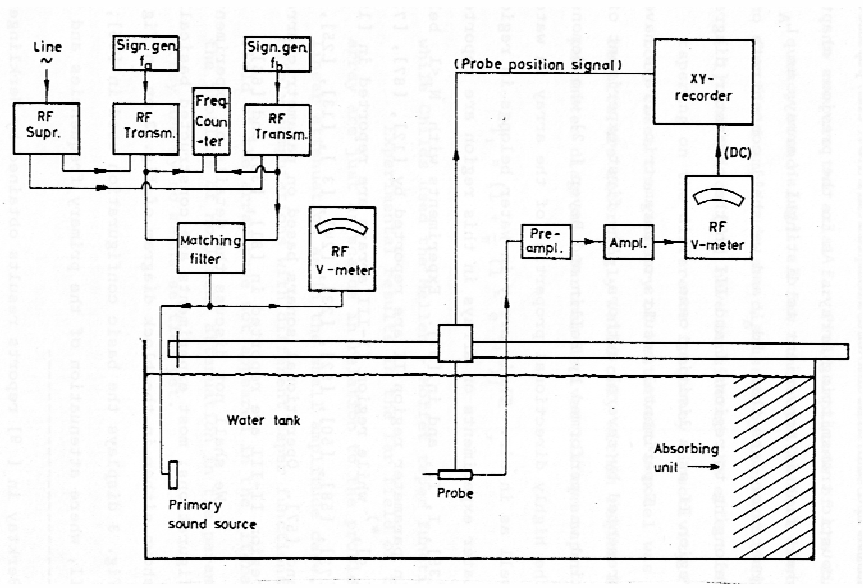
Line
Sign.gen. f_a
Sign.gen. f_b
RF Supr.
RF Transm.
Freq. Coun -ter
RF Transm.
(Probe position signal)
XY-recorder
(DC)
Matching filter
RF V-meter
Pre-ampl.
Ampl.
RF V-meter
Water tank
Absorbing unit
Primary sound source
Probe

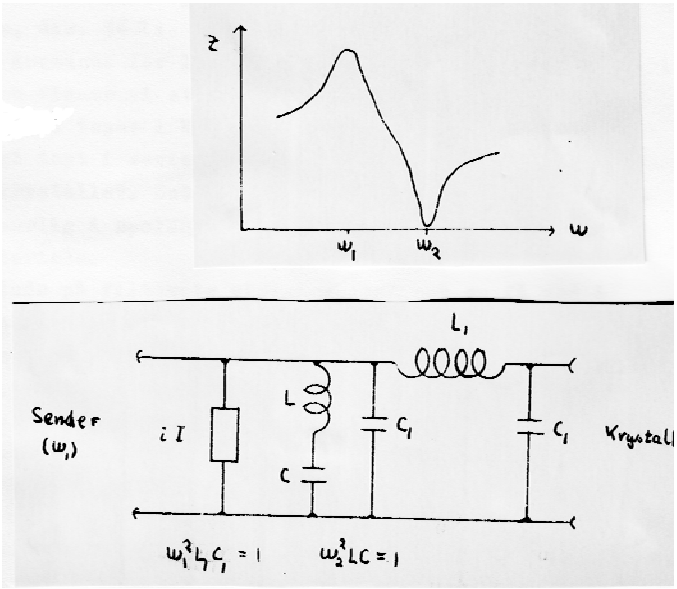
Z
ω_1
ω_2
ω
L_1
L
C
C_1
C_1
Krystall
Sender
(ω_1)
$\omega_1^2 L_1 C_1 = 1$
$\omega_2^2 LC = 1$

crystal was a PI-filter tuned to frequency 1, and characteristic impedance adjusted to match to the crystal impedance. For frequency 2 the PI-filter transformed the short circuit provided by the series resonance to a very high impedance. This stopped frequency 2 from penetrating the filter, while frequency 1 passed to the crystal with near optimal conditions.

Figure 3 is copied from my master thesis. The curve indicates the impedance of the series resonance for the lower frequency. A similar filter was built and tuned to the other frequency, and both were connected at the terminal of the crystal. In those days the impedance analysers available today was only something we could dream of. Instead we bought a Marconi Q-meter, which turned out to be very useful. In addition to help building the filter, it's oscillator was used to generate one of the primary frequencies.

Nonlinearities can be generated everywhere, and to avoid the primary frequencies to enter the other transmitter through the power line an isolation filter using ferrite beads and capacitors was constructed for the power line. Also note that the radio transmitters were used in continuous mode – it turned out to be too difficult to key them with accurately timed pulses.

I'd like to say some words about the sound source as well. Recall that this was my first attempt to build such a device, and there were no-one around to ask for advice. The workshop people were very helpful in making the parts, of course. Figure 4 shows a cross section. It was housed in a brass container mounted on a copper tube, letting the coaxial cable pass through. The crystal was glued to a lucite (plexiglass) disk, and the front face and back electrode was silvered by vacuum deposition of silver. Such equipment is regrettably no longer available to us. The back electrode of the crystal was connected trough a spring contact to an inductance, whose purpose was to cancel out

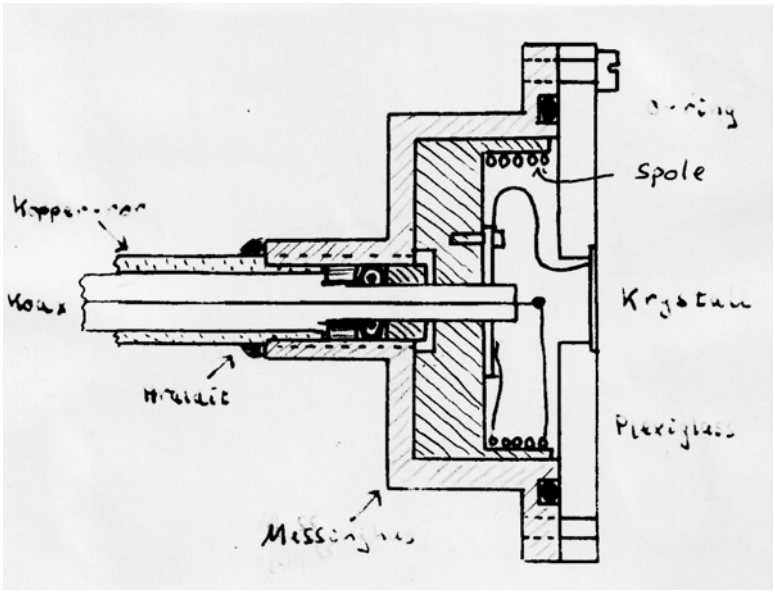

Figure 4: Cross section of the primary sound source

the parallel capacitance of the transducer disk.

The tank was built of plywood and made waterproof by covering the inside with artificial resin ("Beo-dit" – related to Araldite). It was 2 m long and half a meter in cross section, both height and width. The sound source was mounted in one end at middle depth, and a suspension system consisting of an aluminium bar of square cross section was used to hold the receiving probe, allowing it to glide along the bar, and also measuring the directivity by rotating the bar. The bar was arranged to rotate about an axis passing through the front face of the crystal. The position of the

slide could be monitored electrically by a single resistance wire acting as a potentiometer, connected to an XY-recorder. A similar system monitored the rotation angle.

Since continuous waves were used an absorbing device was mounted in the far end of the tank to reduce reflections. It took about half a meter of the available tank length

The probe itself consisted of a coaxial needle hydrophone with a BaTi element, 1mm diameter, resonant at 1 MHz, and a cathode follower (miniature electron tube) mounted inside a brass tube to which the needle hydrophone could be screwed. Later several different needle hydrophones were build, using the same probe holder and electronics. A complicating factor was the need for both high voltage and filament supply to the tube, along with the signal cable.

The rest of the experimental set-up is fairly standard. The signal from the probe was amplified and led to a RF-Voltmeter, whose output was brought to the XY recorder together with the positioning signal.

The experiment did produce some new results. The build-up of the amplitude along the axis, and later fall off, was demonstrated, and the directivity was mapped in quite some detail. The results were published [11] in Journal of Sound and Vibration in 1967, soon after I had finished my master degree.

Figure 5 shows the measured amplitude along the axis of a parametric acoustic array of frequency 1 MHz, generated by primary waves of 16.6 and 17.6 MHz. The so called array length, which is a measure of the efficient length of the interaction region, mainly determined by absorption of the primary waves, is about 6.5 cm. The near field length of the primaries are about 0.5 m, so

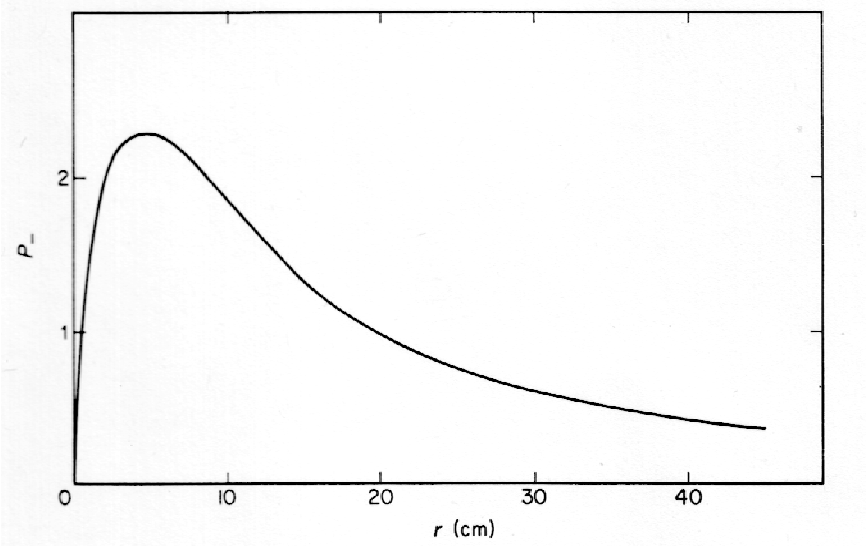

Figure 5: Axial pressure as a function of distance. k_a=27.5.

interactions take place well inside the near field of the primaries (Type I array).

The fact that the sound field vanish as one approaches the source is assuring that the difference frequency sound is not radiated by the source. Actually electromagnetic radiation at the primary frequencies could be detected very close to the source, but this caused no problem at the difference frequency. Later we shall see that the details very close to the source is a bit more subtle, but that was not discovered in the first measurements.

The position of the maximum turned out to depend on the intensity of the primary waves, moving closer to the source with increasing intensity. Trying to explain what determined the position of the maximum, and its dependence on intensity, became a challenge for the following years. Instead of presenting the directivity patterns directly, Figure 6 shows the half pressure angle, Θ_{6dB}, as a function of ka (the beam radius times the difference frequency wavenumber) , compared with theoretical predictions. However, as with all the models available at this time, only far field results could be calculated – that is far field in terms of the array far field, the extent of which was not easy to estimate. My measurements were definitely in the near field of the array.

The beam radius was changed by putting apertures of different diameter in front of the source. The accuracy of this procedure may be questioned, and was not used later, but at least some indication of the tendency was obtained.

What is evident is that the beam-width is more narrow than predicted by the Westervelt formula, and plane collimated primary waves (Tjøttas). The last curve (C) is predicted for direct radiation of the difference frequency from the source.

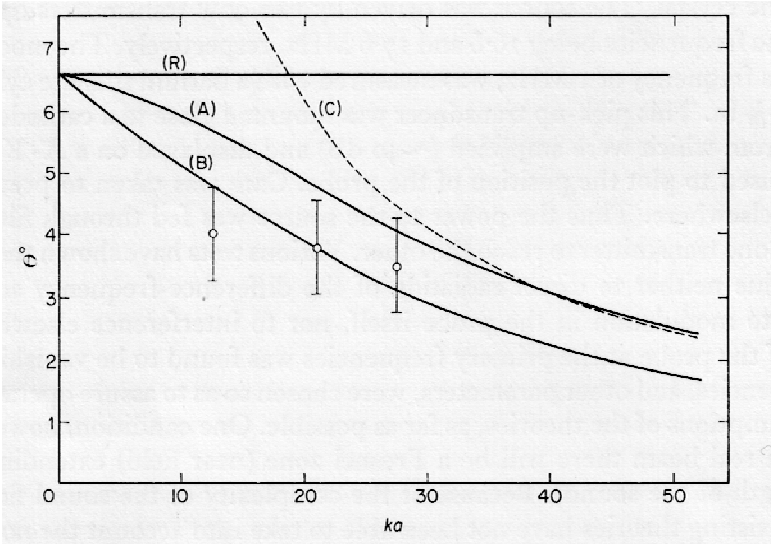

Figure 6: Measured half-pressure angles and theoretical models: A - collimated plane waves, B - diverging primary waves (Type III), C - directly radiated from the piston, R - Westervelt model.

Contemporary activity

Before this, at about the same time as I started on putting up the experiment, another research group entered the scene. In 1965 Orhan Berktay at University of Birmingham published[12] a model similar the Tjøttas, but with a square beam cross section instead of a circular, using the argument that the near field in a square beam is more regular than in a circular. I shall comment on this issue below.

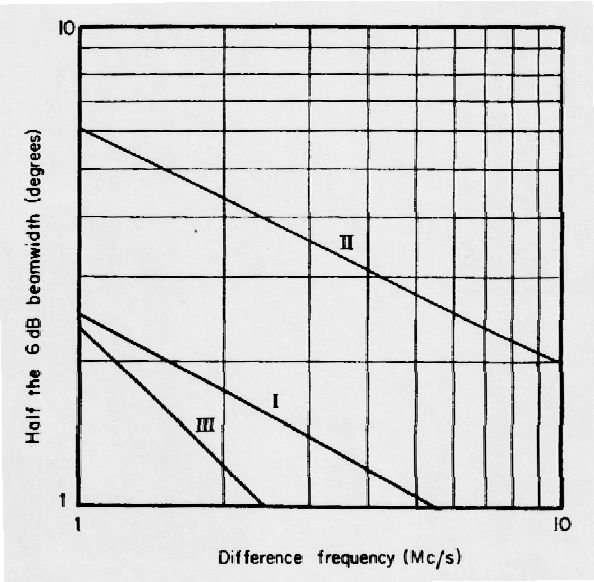

Figure 7: Beamwidth after Bellin and Beyer. Curve I - experimental results, Curve II - Westervelt's model, Curve III - directly radiated from piston. After Berktay [13].

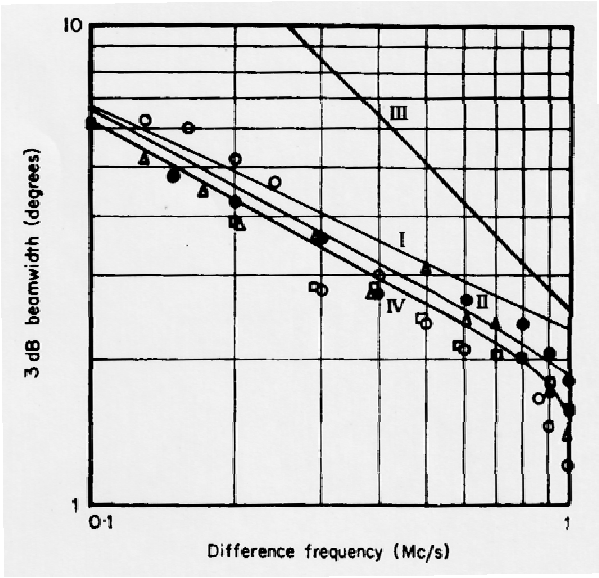

Figure 8: Beamwidth after Berktay [13]. Curve I - Westervelt's model, Curve II - collimated plane waves, Curve III - directly radiated from piston, and several measured points.

Berktay also presented some experimental results of the beam-width of the square beam parametric array. Figures 7 and 8 are borrowed from Berktay's paper [13] in 1965, where Bellin and Beyer's results were reproduced. Both plots are in log-log scale, and difficult to get accurate data from. The horizontal axes are difference frequency in MHz, vertical: half pressure angle in degrees.

The frequency dependence of Bellin and Beyer's measurements follows that of Westervelt's model, but the half power angles are much smaller. Curiously they are broader than if the difference frequency was radiated directly from the source! I shall return to this in below. In contrast, Berktay's results seem to follow Westervelts model rather close, although even here with a more narrow beam-width. But now directly radiated difference frequency is much broader! Their experimental set-up is poorly described, so a comparison between their experiment and mine is difficult. For example, it is impossible to determine to which extent interaction took place in the near-field or in the far field (or both).

Berktay's paper also contains another interesting study, related to the parametric array: namely the nonlinear demodulation of a high frequency sound burst, finding that after propagating so far that the high frequency wave was damped out there would be a remainder which can be described as the second time derivative of the envelope of the original burst. This was later confirmed experimentally, first by Moffett in 1969 [14].

As mentioned above, the nonlinear acoustic community was small and wide spread, but it started to grow after 1960. Of considerable importance were the papers by D. Blackstock in Rochester, and later Austin, where he managed to bridge various models and concepts from the past to show a unified understanding. They are of outstanding quality, and has had a great impact on the teaching of nonlinear acoustics up to these days.

The first occurrence of parametric acoustic arrays in USSR was, I think, by Zverev and Kalachev in 1968 [15], describing their experiment. At the time of the cold war interaction with east was delayed a lot because Russian publications had to be translated and typically were published a year

later. The original paper was actually submitted in 1965. They presented axial amplitude variation and higher than predicted directivity of the difference frequency, similar to the findings in Bergen.

In these years considerable interest was also focused on the possibility to use the parametric interaction to amplify acoustic waves directly, in analogy with the electromagnetic process mentioned initially. It soon became clear that this is not easy. Amplification requires third order interaction, incorporating both the difference and sum frequencies. However, their combination with the fundamental frequencies act in opposition to each other, and the sum frequency needs to be blocked in order to obtain amplification [16]. This would not be the case in the presence of dispersion, but as you know dispersion is in general very weak in acoustic waves. Another problem is logistics: the distance from the source of the pump wave to the receiving hydrophone needs to be many wavelengths, and may be impractical to handle.

Acoustic streaming is another of Sigves Tjøtta's favourite nonlinear effects. Both theoretical and experimental investigations on boundary layer streaming and streaming due to sound waves in a stratified medium (related to radiation pressure) was made during the 1970ies. This, however lies outside the scope of this account.

The earliest ISNAs

The first symposium devoted to nonlinear acoustics was arranged in 1968, by US Navy. It was almost closed, but is still counted as the first ISNA (International Symposium on Nonlinear Acoustics). The proceedings was published in 1970 and contained 5 presentations, but only one on parametric arrays, by Berktay.

In 1969 the next symposium was arranged in Austin, Texas, with 10 presentations, two of which were devoted to parametric arrays: Berktay, and for the first time Muir along with Blue. Both presented experimental results, mainly with beams interacting in the farfield. A wide variety of nonlinear acoustic phenomena were discussed, and the proceedings [see 14], which appeared some two years later, gives an interesting cross section of the activity in USA in the late 60-ties. This was the second ISNA, which has since been followed almost regularly every 3 year, with a few exceptions with a 2 year cyclus.

Tom Muir, at that time a PhD student at Applied Research laboratory (ARL), University of Texas at Austin, was to become one of the leading persons in nonlinear acoustics, not only on parametric arrays. Muir's experiment was made in fresh water, in lake Travis, where the laboratory had a research float. The frequencies were much lower than in previous experiments, and accordingly the ranges involved longer. They measured the field along the axis of the beam, where the array length was much larger than the nearfield length. These were to my knowledge the first results for a Type III parametric array. Figure 9 [17] shows one of their plots – note logarithmic scales on both axes. Here the build up of the difference frequency field may be seen.

Figure 10 shows directivity of difference frequency, compared to Westervelt's model and Naze-Tjøtta's (1964). The half pressure angle is wider than Westervelt's prediction in this case.

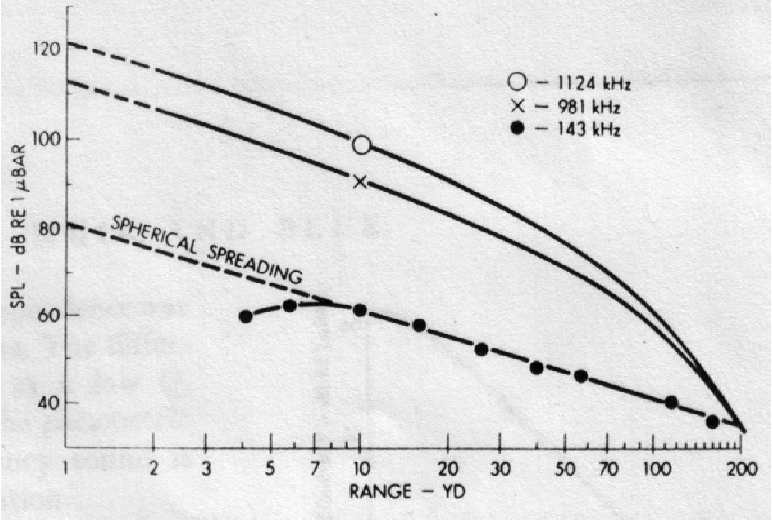

Figure 9: Axial SPL versus range for the two high frequencies and the difference frequency.

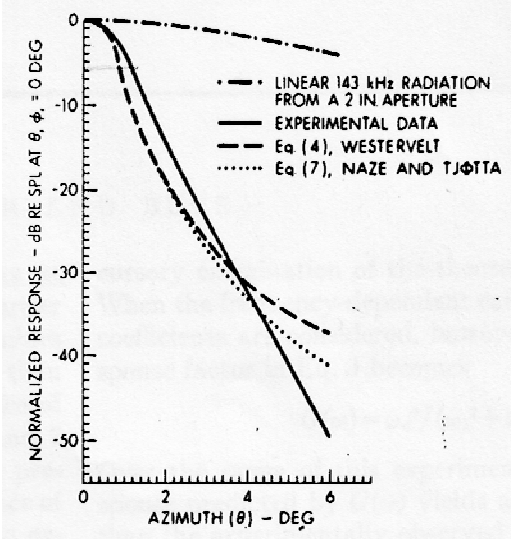

Figure 10: Beam patterns

What does not appear from this figure is that it is approximately equal to the half pressure angle of the primaries. We shall return to this issue subsequently.

Next activity in Bergen

After finishing my master degree I was awarded a fellowship to go on with investigations on the parametric array. By 1968 University of Bergen had got a new IBM 360 computer, the wonder of its time, and this inspired attempts to compute the parametric array by first computing the primary nearfields, and then the interaction leading to the difference frequency. It was soon found that this was beyond the computer's capacity (far less than a modern PC!).

Thus, the nearfield had to be approximated, and the task to get more information on this was undertaken. Up to that time the nearfield was only calculated for ka values less than about 5. In addition some very approximate solutions existed for the region near the axis. In our case ka values for the primaries were near 80. A numerical code was developed, which showed that the field out to half the last axial maximum (at $a^2/\bullet$) behaved very much like a collimated plane wave, except for a narrow region about the axis. The model and results were printed in a report [18] in 1970, but never sent to a journal for publication. Just a little time after this Zemanek [19] published a similar study in JASA.

I could spend quite some time discussing the nearfield alone, but not this is not the place. Just one comment. Along the axis the pressure amplitude in a circular cross section beam, due to the symmetry, oscillates a lot, and it was believed that this dominated most of the near field outside the axis also. The numerical results demonstrated, however, that these oscillations were confined to a very narrow region around the axis. Further away from the axis a plane wave is a good approximation. A beam of rectangular cross section lacks some of the symmetry, and as calculated by Freedman [20], the axial fluctuations are much smaller. This was the argument Berktay used for selecting rectangular primary beams. In practice the difference may be ignored when parametric arrays are concerned.

As a consequence of these findings a simple model to compute the axial pressure in the array was developed, assuming a well collimated circular sound beam. One simply had to integrate the axial field of a continuous distribution of spherical pistons, accounting for amplitude reduction due to absorption.

Figure 11 is a plot of the simulation of the axial field of the array compared with experiment (dashed). The correspondence is not perfect but rather assuring. Note the tiny details at the start of both curves. They were not seen in the initial experiment, but appeared when the diameter of the needle hydrophone was reduced. They are due to the nearfield of the difference frequency «virtual» sources, not the primary wave field. If the radius of the simulated beam is reduced by 5% the curves fit even better.

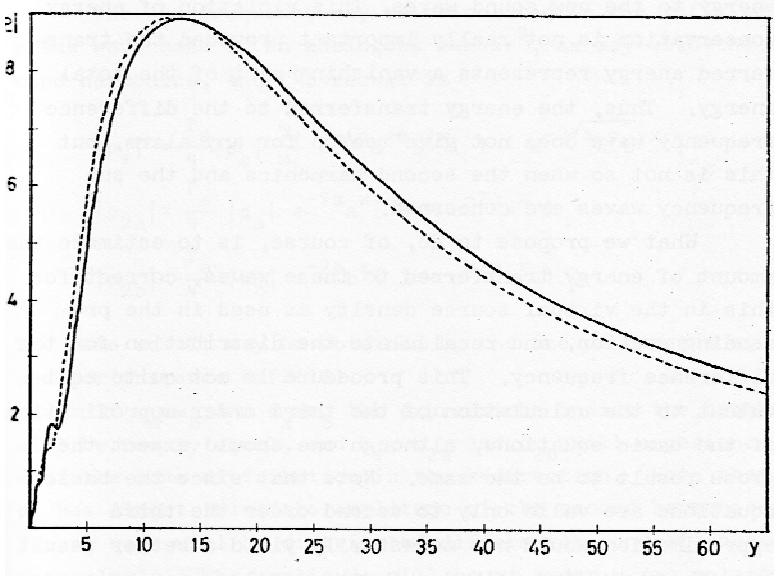

Figure 12: Measured (dashed) and computed (line) axial pressure in a collimated array. y is distance divided by source radius

This computer code allowed a numerical study of the behaviour of the axial field while varying parameters like frequency, radius, absorption etc. The information thus collected aided in finding a parameter description of the properties of this type of array, which led the way to a general parameter description for parametric acoustic arrays in general: the "Vestrheim parameters" [21] - to be discussed below.

Figure 11: Directivity of 3 MHz difference frequency, collimated plane waves.

Figure 13: Variation of half pressure angle with range in a parametric array - the "Bergen effect".

In his master project Magne Vestrheim continued experimenting on the collimated plane wave array, and succeeded to calibrate the amplitudes, as well as performing a detailed study of the directivity as a function of distance. The numerical code was, however, not extended to cover directivity.

Figure 12 shows an example to illustrate the misconception that the parametric acoustic array is devoid of side lobes. This example shows that this is not always the case, but admittedly sidelobes are rare, and occur only for Type I arrays.

Figure 13 illustrates what was later known as the «Bergen effect». It was a puzzling fact that the directivity seemed to depend on the distance from the primary source. In this plot Vestrheim showed why: since the interaction takes place in an extended volume the natural origin to use for the directivity lies in front of the primary source. Very close to the source no origin is established – it seem to move slowly outwards with range of observation, but some distance outside the interaction region it seems to become fixed. When this was realized it was not difficult to extend the measured beamwidth to the one expected in the very far field, which was necessary to compare with theoretical models only valid in the far field. A similar effect is observed for Type III arrays, as noted by Muir and Willette [22] in 1972, but then the directivity increases with distance, and no minimum in half pressure angle occurs.

The Bergen effect also throws some light on the peculiar result of Bellin and Beyer, in that the beamwidth of the parametric array was wider than if the sound was radiated from the primary piston directly. This could be explained if the beamwidth was measured rather close to the primary source, see Figure 13.

ISNA in Birmingham

The next international symposium on nonlinear acoustics took place in Europe, arranged by

Berktay's group in Birmingham, UK, in 1971. For us this was a big event, allowing us to meet for the first time many of the great names in the field. Truly, previous occasional visits had found place – in 1968 R. Mellen, at US Navy, honoured us with a surprise visit by suddenly turning up at the laboratory. He probably wanted to meet the Tjøttas, who were away at the time, and had to be content with me. Around 1970 Blackstock and Muir had a tour to Europe, including Bergen. It was really exciting to have them in our laboratory with us. In Birmingham were both Beyer and Westervelt, and also Leif Bjørnø made his entrance in the field for the first time. To mention just a few. We had hoped that representatives from the Soviet groups would be there too, but the political situation put a stop to that, unfortunately. For the first time an application of the parametric array was presented: G.M. Walsh at Raytheon demonstrated sub-bottom profiling with a 200 kHz array producing 3.5 to 12 kHz at beamwidths 2-5 degrees, and high resolution depth sounding down to 2000 fathoms. I do not know if this was ever commercialized. In Birmingham altogether 14 presentations were given, 8 of which on the parametric array.

Vestrheim and myself presented the results just shown, which were well received. Unfortunately the proceedings, which appeared a year later was in the lousiest technical condition. We were promised a rectifying new version, but this was never produced, and the consequence is that the material presented at that symposium remain a secret for those not present. We reprinted our work as local reports some years later, but also those were distributed rather sparsely [23,24].

The Vestrheim parameters

The Vestrheim parameters appeared as a result of an attempt to categorize the properties of parametric arrays in a simple way, and was presented at ISNA in Copenhagen in 1973 [21]. Basically there are two parameters, but it is also convenient to use two derived ones. The basic parameters are defined as follows:

$$N_f = \frac{f_-}{f_1}$$ (frequency number, "downshift ratio")

with f_=difference frequency and f_1 the highest primary frequency.

$$N_F = \frac{k_1 L_A}{k_1 a} = \frac{L_A}{2R_1}$$ ("field number").

The field number is a measure of the array length, L_A, relative to the primary beam Rayleigh length, $R_1=½k_1a^2$, k_1 is the wave number of the highest primary frequency and a is source radius,.

Any array specified by frequencies, primary source radius, sound velocity and medium absorption coefficient will be designed definite N_f, N_F values accordingly, and thus represent a point in the N_f-N_F plane, often referred to as the Vestrheim parameter diagram.

The derived parameters are:

$N_D = N_f N_F$ ("divergence number"), and

$N_A = N_f / N_F$ ("aperture number").

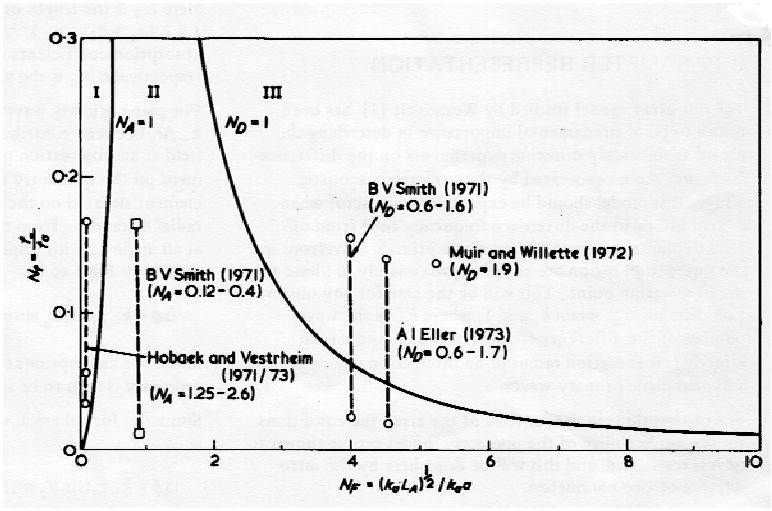

Figure 14: The Vestrheim parameter diagram with some experimental arrays plotted in. From [20].

Of the derived parameters N_D gives a measure of the maximum destructive phase shift within the array due to curved wavefronts. N_A may be interpreted as a measure of the ratio of difference frequency nearfield length to the array length. In the parameter diagram curves with constant N_A or N_D may be drawn, dividing the diagram in regions. An example is shown with N_A=1 and N_D=1 in Figure 14.

In this diagram also some experimental arrays reported in the literature are included.
The collimated plane wave array of Type I is found in the left region. Arrays with interaction in the farfield of the primaries, Type III, is located in the right region. The central region corresponds roughly with Type II, the Westervelt model, e.g. pencil beam type. Since this diagram was presented by Vestrheim in 1973 many more realizations of parametric arrays have been made, mostly in region III.

Next experiment in Bergen

In 1974 a new project started in Bergen in cooperation with Simrad and Jens Hovem at Norwegian Technical University in Trondheim. This led to the construction of an array which is the mother of the TOPAS [25] array, commercialized many years later. Another outcome was a laboratory experiment on Type III arrays. Here measurements out to almost 4 array lengths were obtained, which was much further out than previous experiments on this type of arrays. Directivity and amplitude as a function of range was studied. The results are too detailed to be discussed here. However, one important conclusion need to be presented.

Figure 15 shows measured beamwidths (half power angles) as a function of the parameter N_D. Westervelt's model is used for normalization, and is represented by the horizontal line marked W, and is not dependent on the divergence number. Measured data is collected from a lot of sources, including our own measurements (circles). For $N_D>1$ the beamwidth becomes wider than Westervelt's, but we see that it can be more narrow for $N_D<1$. The line marked B corresponds to the product of the primary beam directivities. Several analytical models had this as a limit if N_D becomes large. We see no experimental evidence of this. Instead the measurements seem to follow line A, which is the directivity of the primary beam (the highest frequency). This is an important result, making it relatively simple to predict the directivity of the array!

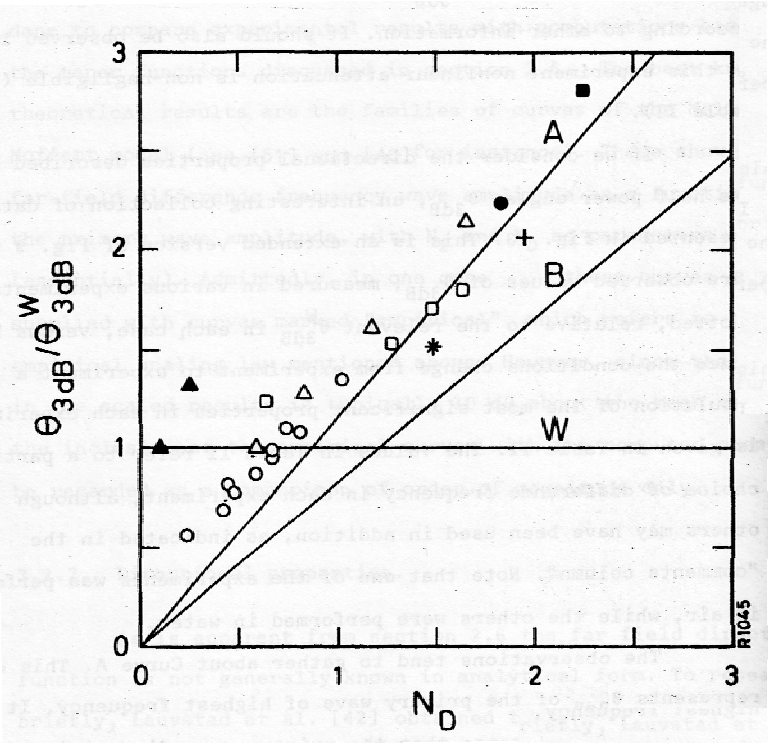

Figure 15: Normalized half power angles versus N_D. Symbols - Various experimental data. Curve A - primary directivity, Curve B - source density directivity, Curve W - Westervelt directivity.

At this time a number of approximate models attempting to describe the parametric array had been suggested, with varying degree of success. I cannot go into detail about these here. The most widely used was the Mellen-Moffett [26] model. Unfortunately the derivation of the model contained several short-cuts which made it extremely difficult to access the limits of validity of the model. The real improvement came with the KZK-equation, which is a parabolic approximation of the wave equation including nonlinearity and absorption, derived some 10 years earlier in USSR by E.A. Zabolotskaya and R.V. Khokhlov [27], and later extended by Kuznetsov [28]. S. Tjøtta and I used it in 1978 [29] to simulate the «Bergen effect» in Type I arrays.

Personally this was my last effort in investigating parametric acoustic arrays. Later it we have used it as a laboratory tool in an experiment on reflection/transmission of near critical incidence sound beams at interfaces between two fluids. But in Bergen theoretical modeling continued. Jacqueline Tjøtta returned to acoustics in the late 1970ies working on the KZK-equation, and during a sabbatical stay at ARL the Tjøttas became engaged in numerical calculations on a specific array designed by Tom Muir. This work subsequently led to the the development of a very general computer code, later termed "The Bergen Code" [30], which applies to a number of propagation problems in nonlinear acoustics, including the parametric acoustic array. Although more recent variations have been developed it is still in use today.

Epilogue

The parametric acoustic array has entered a niche where the need for its special properties compensate for the relatively low amplitude. I tried to sell the concept to researchers in fisheries early in the 1970ies, but without much success. Only recently has a genuine interest for the use of parametric arrays in that area been aroused. The applications found today are mainly where narrow, low frequency sound beams are needed, such as in sub-bottom profilers, or where sound-sources with almost frequency independent directivity is needed, since this is governed by the primary

directivity. As such it is also a very versatile laboratory tool.

In the period 1980-88 Jacqueline and Sigve Tjøtta published 27 papers, where more than half were on nonlinear acoustics. In Bergen a large number of master and PhD students had nonlinear acoustics as a topic for their thesis work, and it is not too strong to say that all of these, as well as the subsequent activity at University of Bergen in linear acoustics, originated with the parametric acoustical array.

References

1. U. Ingard and D.C. Pridmore-Brown, *Scattering of sound by sound*, J. Acoust. Soc. Am. 28, 367 (1956)
2. P.J. Westervelt, *Scattering of sound by sound*, J. Acoust. Soc. Am. 29, 199-203 (1957a)
3. P.J. Westervelt, *Scattering of sound by sound*, J. Acoust. Soc. Am. 29, 934-935 (1957b)
4. P.J. Westervelt, *Parametric End-Fire Array*, J. Acoust. Soc. Am. 32, 934A (1960)
5. J.L.S. Bellin and R.T. Beyer, *Experimental investigation of an End-Fire Array*, J. Acoust. Soc. Am. 34, 1051-1054 (1962).
6. P.J. Westervelt, *Parametric End-Fire Arra*y, J. Acoust. Soc. Am. 35, 535-537 (1963)
7. S. Tjøtta, *On some non-linear effects in sound fields, with special emphasis on the generation of vorticity and the formation of streaming patterns*, Archiv for Mathematik og Naturvidenskap B.LIV. nr. 1 og 2, (1959)
8. V. Lauvstad and S. Tjøtta, *Nonlinear interaction of two sound beams*, J. Acoust. Soc. Am. 35, 929-930(L)(1963).
9. V. Lauvstad, J. Naze and S. Tjøtta, *Nonlinear interaction of two soundwaves,* Acta Universitatis Bergensis series Mathematica Rerumque Naturalium, No. 12 1964.
10. J. Naze and S. Tjøtta, *Nonlinear Interaction of Two Sound Beams*, J. Acoust. Soc. Am., 37, 174-175 (1965).
11. H. Hobæk, *Experimental investigation of an acoustical end-fire array*, J. Sound. Vib. 6,460-463 (1967).
12. H.O. Berktay and B.V. Smith, *End-fire array of virtual sound sources arising from interaction of sound waves*, Electronics Letters, 1, 6 (1965).
13. H.O. Berktay, *Possible exploatation of non-linear acoustics in underwater transmitting applicaitons*, J. Sound. Vib. 2,435-446 (1965).
14. M.B. Moffett, *Large-amplitude pulse propagation, a transient effect, in "Nonlinear Acoustics"*, proceedings of a Conference held at Applied Research laboratories, The University at Texas, Austin, 10-11 november 1969, ed. T.G. Muir.
15. V.A. Zverev and A.I. Kalachev, *Measurement of the scattering of sound by sound in the superposition of parallel beams*, Soviet Physics – Acoust., 14, 173-178 (1968).
16. S. Tjøtta, *Some non-linear effects in sound fields*, J. Sound.Vib. 6, 255-267 (1967).
17. T.G. Muir and J.E. Blue, *Experiments on the acoustic modulation of large amplitude waves*, J. Acoust. Soc. Am. 46, 227-232 (1969).
18. H. Hobaek, *On the acoustical near field of a circular piston source. Results from a numerical investigation*. Scientific/Technical report no. 32, Department of Physics, University of Bergen, 1970.
19. J. Zemanek, *Beam behaviour within the nearfield of a vibrating piston*, J. Acoust. Soc. Am. 49, 181-191 (1971).
20. A. Freedman, *Sound field of a rectangular piston*, J. Acoust. Soc. Am. 32, 197-209 (1960).
21. M. Vestrheim, *A parameter representation of the parametric acoustic array*, in Finite-amplitude wave effects in fluids, proceedings of the 1973 symposium, Copenhagen, ed. L. Bjørnø, 140-144 (1974).

22. T.G, Muir and J.G. Willette, *Parametric acoustic transmitting arrays*, J. Acoust. Soc. Am. 52, |481-1486 (1972).
23. H. Hobæk and M. Vestrheim, *Axial distribution of difference frequency sound in a collimated beam of circular cross section*, Scientific/Technical report No 94, Department of Physics, University of Bergen, 1976.
24. M. Vestrheim and H. Hobæk, *Angular distribution of nonlinearly generated difference frequency sound*, Scientific/Technical report No 95, Department of Physics, University of Bergen, 1976.
25. P. Pettersen, J.M. Hovem, A. Løvik and T. Knudsen, *A new sub-bottom profiling sonar using a nonlinear sound source*, in Proceedings of the Joint Conference on Instrumentation in Oceanography, University of North Wales, Bangor (1975)
26. R.H. Mellen and M.B. Moffett, *A model for parametric sonar radiation design*, Naval Underwater Systems Center, Technical Memorandum No. PA4 229-71 (1971).
27. E.A. Zabolotskaya and R.V. Khoklov, *Quasi-plane waves inthe nonlinear acoustics of confined beams*, Soviet. Phys. Acoust., 15,35-40 (1969).
28. V.P. Kuznetsov, *Equations of nonlinear acoustics*, Soviet. Phys. Acoust., 16, 467-470 (1971).
29. H. Hobaek and S. Tjøtta, *Theory of parametric arrays*, Colloque C8, supplement au no 11, tome 40, novembre, C8 101-109 (1979).
30. S.I. Aanonsen, T. Barkve, J. Naze Tjøtta and S. Tjøtta, *Distortion and harmonic generation in the nearfield of a finite amplitude sound beam*, J. Acoust. Soc. Am. 75, 749-768(1984).

Nonlinear sound propagation effects in fisheries research echo sounders

Audun Pedersen[1], Per Lunde[2,1], Rolf Korneliussen[3], Magne Vestrheim[2], Frank Tichy[4], and Andrew Baker[5]

[1] Christian Michelsen Research AS, Fantoftveien 38, N-5892 Bergen, Norway
[2] University of Bergen, Department of Physics and Technology, Allégaten 55, N-5007 Bergen, Norway
[3] Institute of Marine Research, P. O. Box 1870 Nordnes, N-5817 Bergen, Norway
[4] Kongsberg Maritime AS, Strandpromenaden 55, N-3183 Horten, Norway
[5] Christian Michelsen Research AS, Fantoftveien 38, N-5892 Bergen, Norway (Present address: Schlumberger, Sandsliåsen 40, N-5254 Sandsli, Norway)

Abstract

Echo sounders are commonly used for abundance estimation of fish and plankton, supported by biological sampling. The most common operating frequency in traditional single-frequency fish abundance estimates is 38 kHz, but increasingly used multi-frequency methods for identifying and quantifying zooplankton and certain species of fish typically operate in the range 10 kHz–500 kHz. The acoustic methods rely on calibrations using backscattering targets at relatively short distances from the echo sounder transducers. The linear wave equation is generally applied to compensate for the transmission loss for scatterers at other distances than the calibration distance. Nonlinear sound propagation effects have however been found to introduce significant errors in backscatter measurements in the upper part of the frequency range used in multi-frequency methods, using standard echo sounder drive levels. In the present work nonlinear sound propagation effects for common scientific echo sounders operating at 120 kHz and 200 kHz are investigated experimentally and theoretically. Such effects are shown to occur at both frequencies when high power settings are used. Nonlinear sound propagation effects are a feature of sound propagation through water and therefore occur independently of what acoustic equipment is used. Recommendations for reduced drive levels in order to reduce nonlinear errors are discussed. Moreover, a method based on numerical simulations is proposed for compensating for errors in biomass estimation, including consideration of possible nonlinear effects in on-ship echo sounder calibration. The proposed method may have potential for use on historical time series data as well as for new acoustic surveys.

32nd Scandinavian Symposium on Physical Acoustics, 8-11 Feb 2009, Finse, Norway

Adaptive Ultrasonic Transducer

Array Module

Adam Suleiman, Halvor Hobæk, Lars G. Johansen
contact: adam.suleiman@student.uib.no

Department of Physics and Technology
University of Bergen

Introduction

- Piezoelectric array (Pz27) to be used in time-reversal applications
- Transducer has been cut (from one piece) so that the elements are connected by a 4mm thick mid-plane
- Excitation of one element will result in coupling effects
- So, how will these coupling effects influence the directivity?

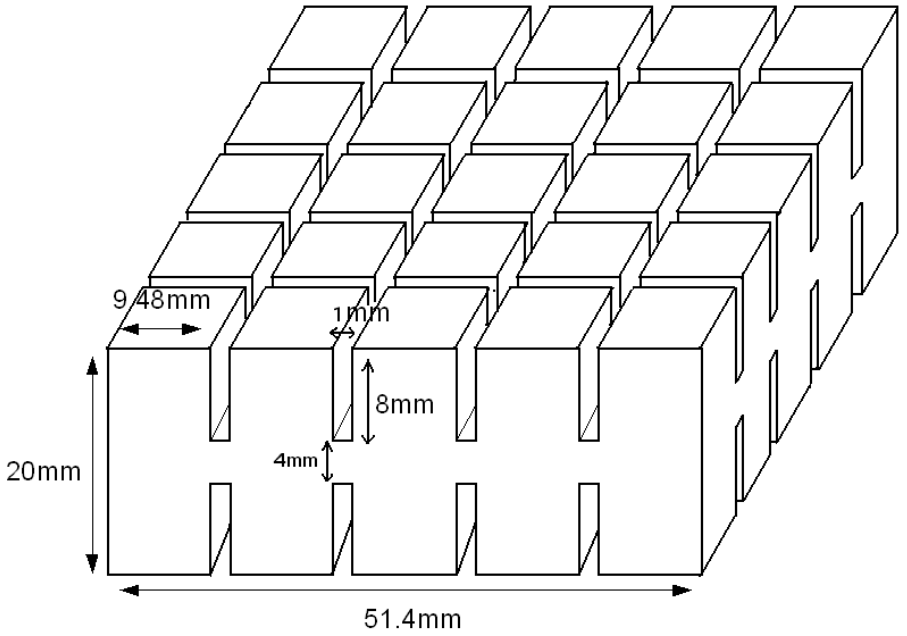

- Element-dimensions: $A \approx 1\text{cm}^2$, T=2cm.
- Resonance frequency: 73-76kHz, (before cutting: 100kHz)

Contents

- Coupling measurements in air surroundings
- Coupling measurements in water surroundings
- Directivity measurements in water surroundings
- Conclusion

First: Some pictures

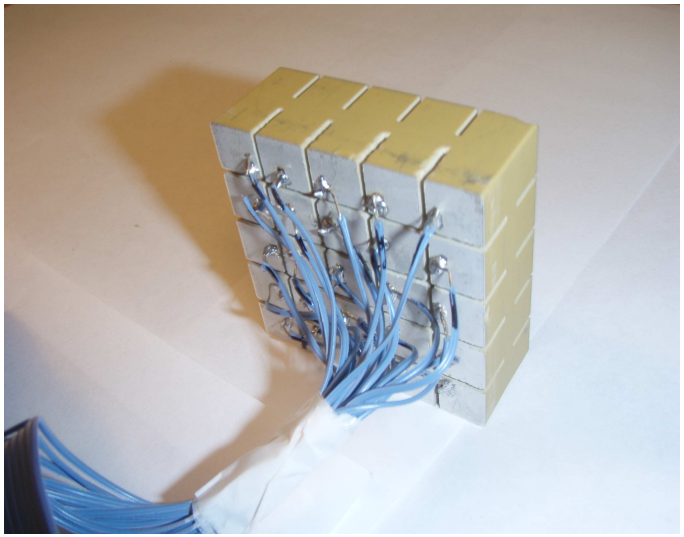

Wires connected to each element pre to applying voltage

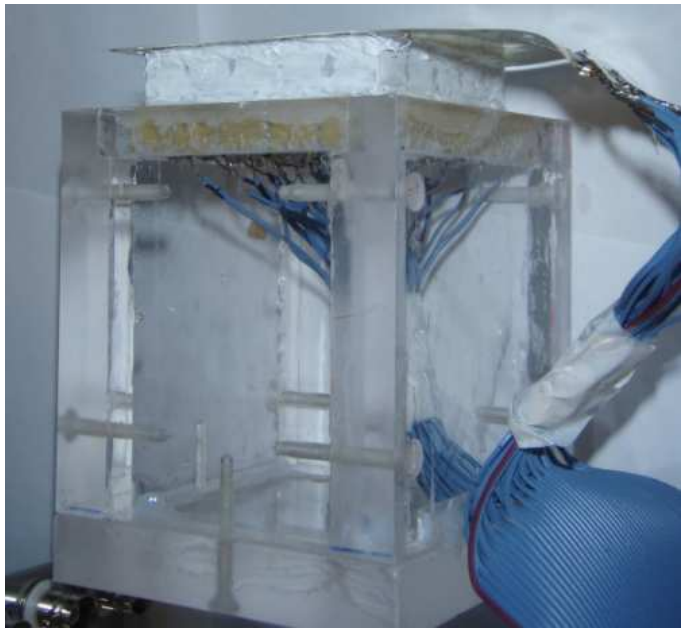

Making the array waterproof

Pictures

Transducer-construction

- Bracket containing coaxial cables, one for each element.
- Brass foil on top of array, gathering ground signals.

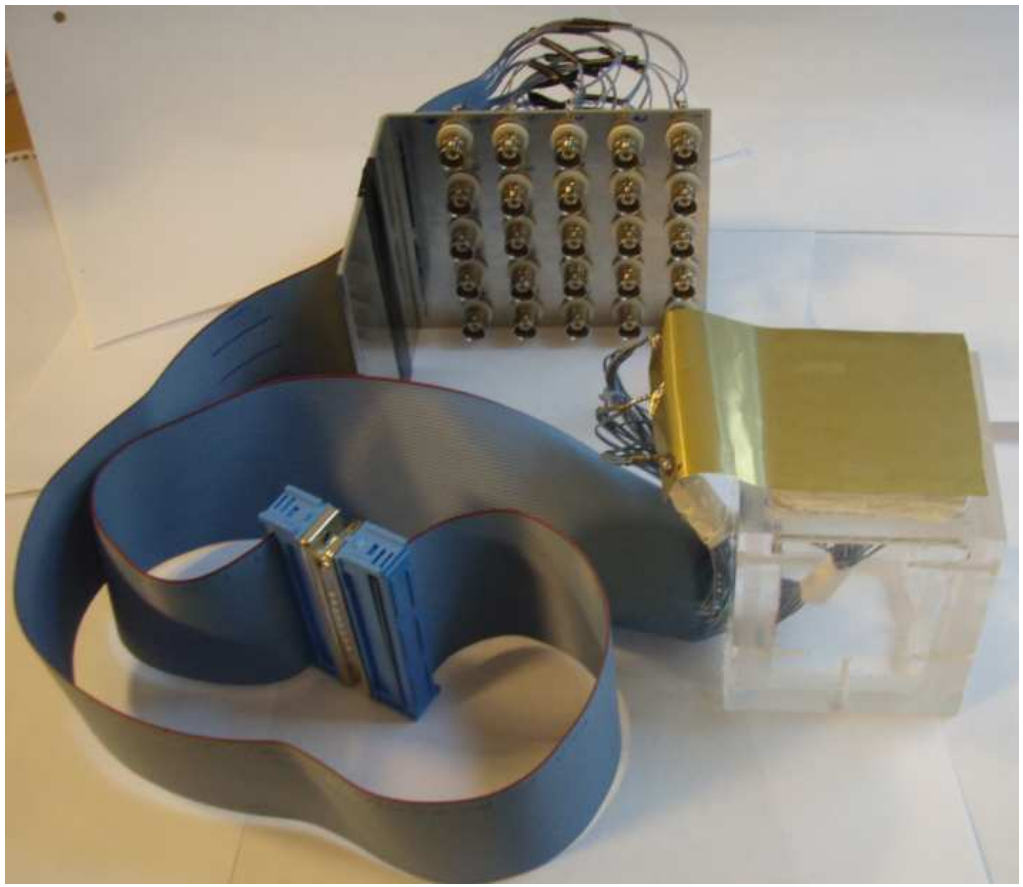

Coupling measurements in air surroundings

Methods:

1. Excitation of one element by applying a burst of its resonance frequency, with voltage, 2V peak-to-peak.
2. Measuring the response occurring from the 24 other elements.
3. Mapping the results.

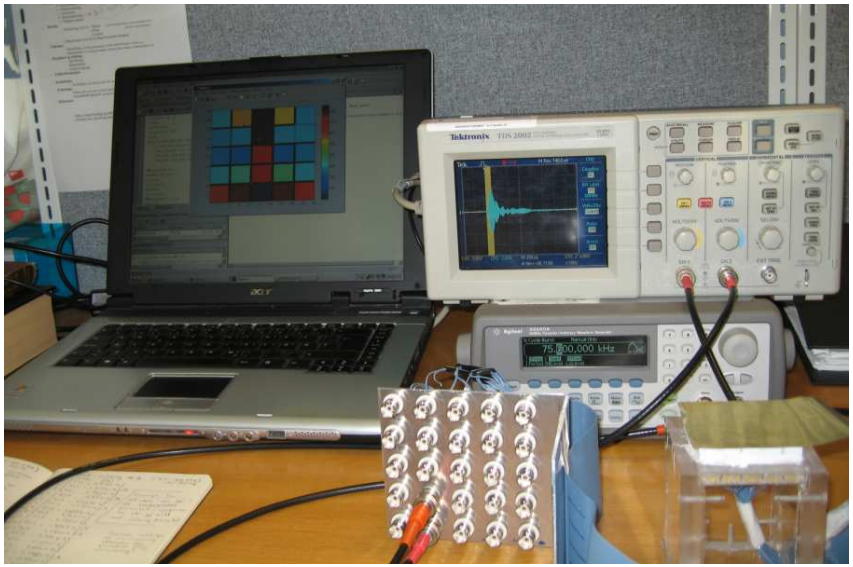

Coupling measurements in air surroundings

Results:

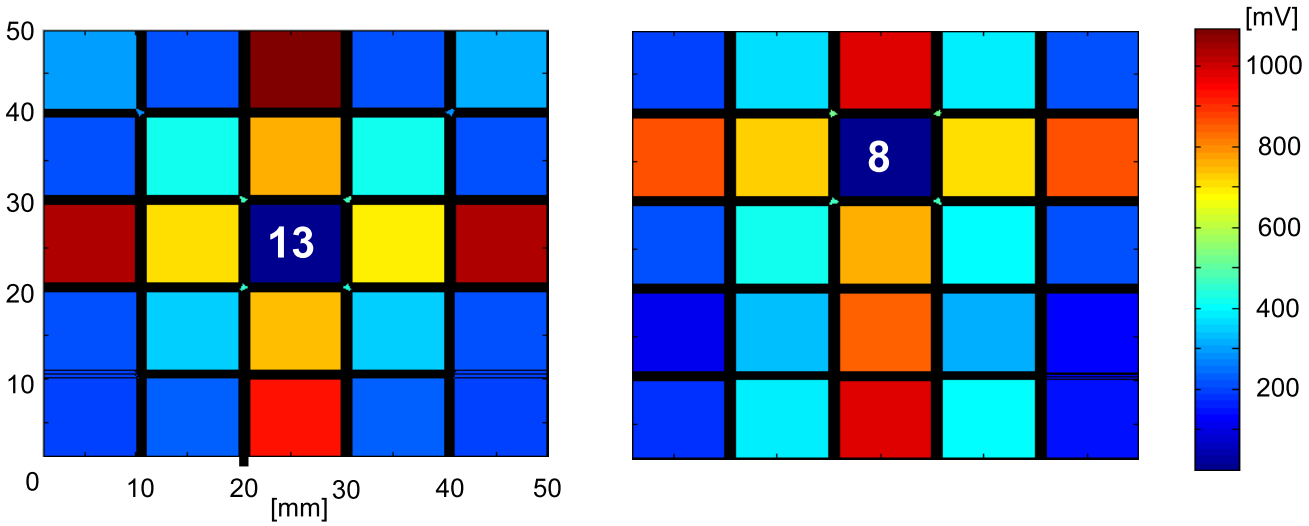

Left matrix shows results regarding an excitation of the center element. Right matrix shows same measurements regarding element number 8. These measurements shows larger responses in lateral directions relative to the operating element. The largest response occur from the edge-elements (due to their frequency response?).

Coupling measurements in air surroundings

More results:

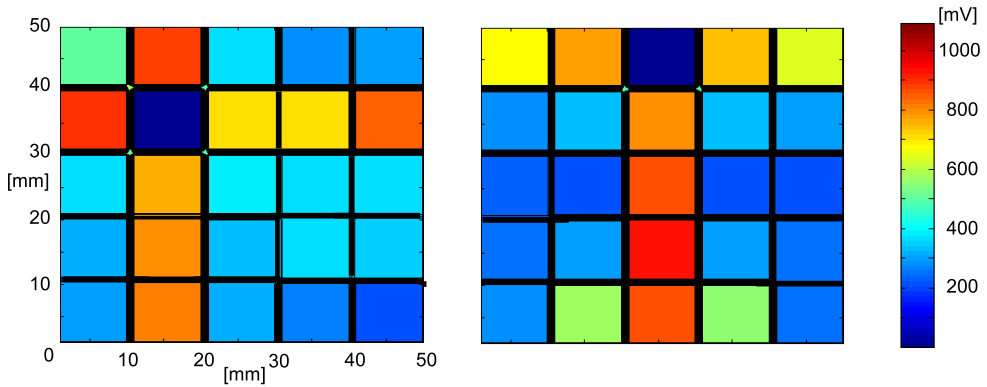

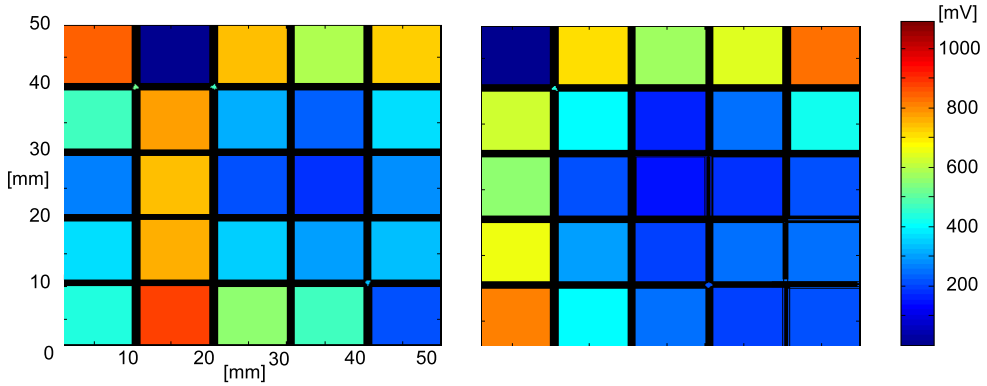

Coupling measurements in water surroundings

Why water?

- Because the directivity was chosen to be measured in water due to satisfying sound transmission.
- Therefore, by first measuring the coupling in water, we may perhaps obtain an indication of expected disturbance in the pressure field.

Methods:

- Array is now placed 30 cm below watersurface in a barrel.
- Same procedures as in air measurements.

Coupling measurements in water surroundings

Results:

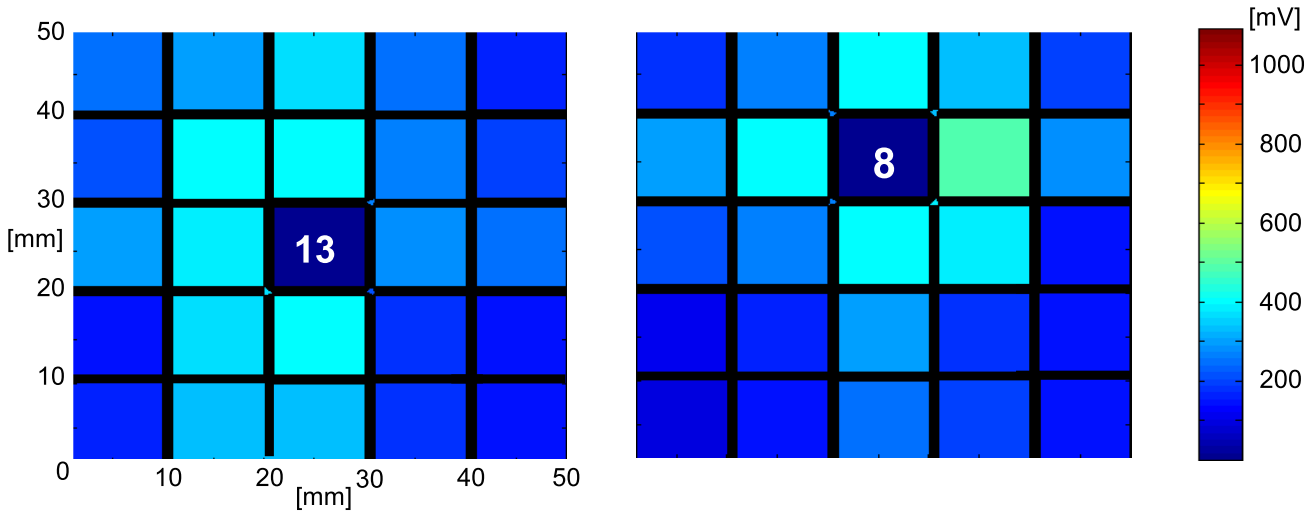

- Less response compared to air measurements.
- Infact, if $\bar{U}$ = average respons, then $\bar{U}_{\text{water}} \lesssim \frac{1}{2}\overline{U}_{\text{air}}$

Reason:

- Larger impedance in water (opposed to air) is causing more acoustic energy to be transmitted off the array.
- Water puts pressure-load on elements, resulting in less vibration.

Directivity

Methods:

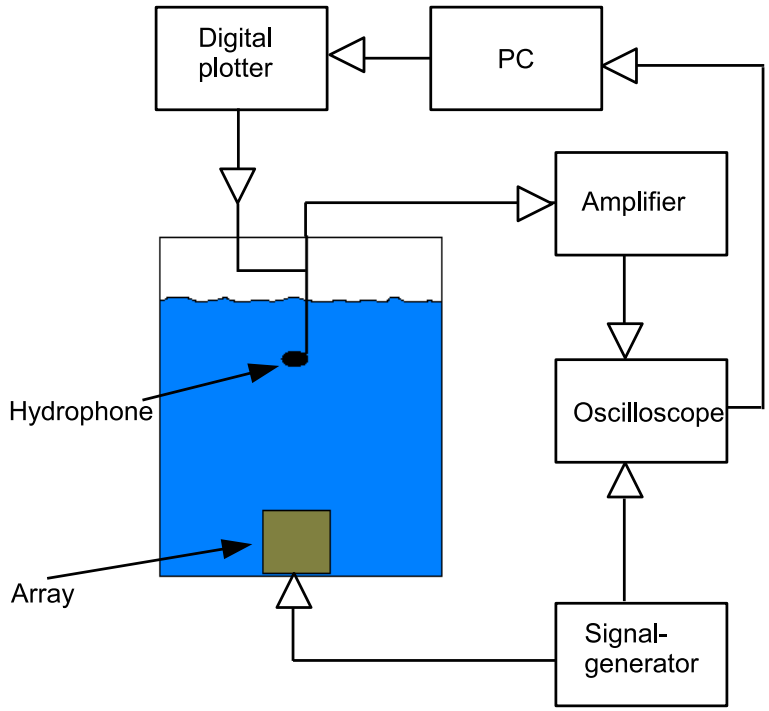

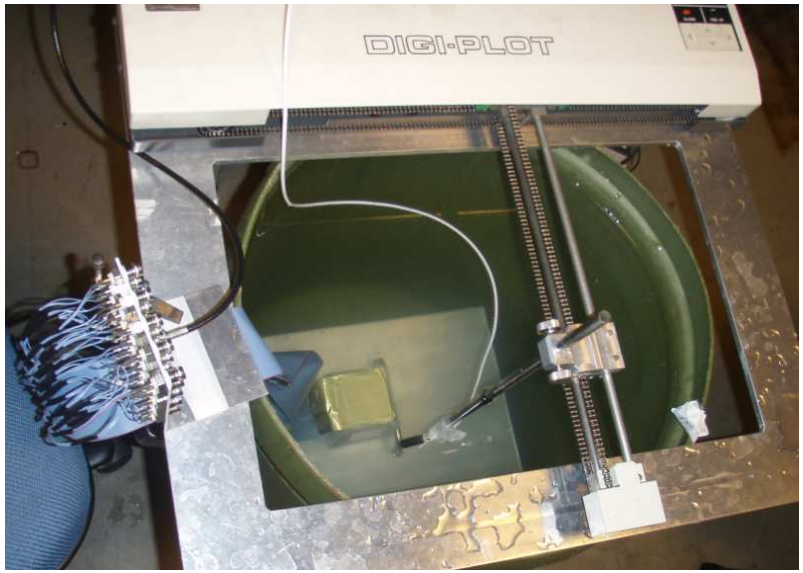

Directivity is measured while excitating one element only.

Directivity

Theory [1,2] **:** *one element, one dimension*

- The source-distribution of a square transduser-element, with surface side-lengths, L_x, is given by
  - $T_1(x) = \text{rect}(L_x)$
- The directivity-function, $f(u)$, is obtained by applying the convolution-theorem on T:
  - $f_1(u) = \text{sinc}(\pi u L_x), \qquad u = \dfrac{\sin\theta}{\lambda}$

Directivity

Theory [1,2] **:** *array, one dimension*

- The source-distribution of multiple square array-elements, each with surface side-lengths, L_x, and mutual center-distance, d_x,
  - is given by $T_5(x) = [\text{comb}(d_x) * \text{rect}(L_x)]\text{rect}(R_x)$

    where R_x is the total side-length of the array.

- By using the convolution-theorem, we get the directivity-function:
  - $f_5(u) = [\text{sinc}(\pi u L_x) \cdot \text{comb}(1/d_x)] * \text{sinc}(\pi u R_x)$
  - **PS:** All elements are emitting same phase and amplitude!

Directivity

Results:

As expected, the measured field does seem to have smaller beamwidth than the calculated field, most likely due to the coupling effects. This will limit the possibilities regarding phase shifting.

Disturbance in measured field is assumed related to airbubbles occurring on hydrophone, and aberration from symmetry in boundary conditions.

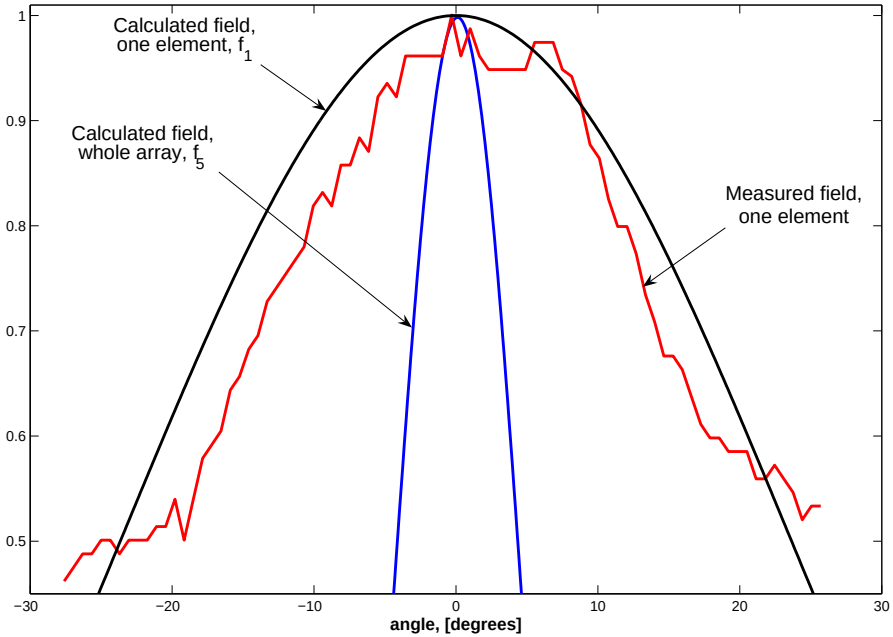

$$f = f(\theta), \quad \theta = \theta(u) = \sin^{-1}(u \cdot \lambda)$$

Conclusion

- Coupling effects are smaller in water compared to air (by factor $\lesssim 0.5$).
- and does seem to have an impact on the beam width in water-environment.

Future tasks

- Applying the external, modified electronics system, and try to make array usable for time reversal applications.
- Test the array on an oil/gas separator.
- Try to reduce the coupling effects by modifying the array construction.

References

[1] : H. Hobæk, ”Akustisk avbildning og arrayteknologi”, 2005.

[2] : B.D. Steinberg ”Principles of aperture and array system design”, 1976.

Diffraction management with sonic crystals

Isabel Pérez-Arjona[1], Víctor Espinosa[1], Víctor J. Sánchez-Morcillo[1], Javier Redondo[1] and Kestutis Staliunas[2]

[1] Institut d'Investigació per a la Gestió Integrada de Zones Costaneres, Universitat Politècnica de València, E-46730 Grau de Gandia (Spain)
[2] ICREA - Departament de Fisica i Enginyeria Nuclear, Universitat Politècnica de Catalunya, Colom 11, E-08222 Terrassa (Spain)

ABSTRACT
Sonic crystals are media with a periodic modulation of the acoustic parameters, as the density and the bulk modulus. They have recently attracted a great interest, because of their potential applications in the control of sound propagation, used as reflectors, focusers or waveguides. All these properties are related with the dispersion introduced by the crystal anisotropy. We report on the propagation two phenomena related with the spatial dispersion properties of the crystal: we show experimentally the nondiffractive propagation of sound in three-dimensional sonic crystals (inside the crystal) and we analytically evaluate, numerically (FDTD) calculate, and experimentally measure the focusing properties of the propagated sound beam behind two-dimensional sonic crystals. Support from Spanish MEC, project FIS2008-06024-C03 and C02 and from Universitat Politècnica de València through Project 20080025, are acknowledged.

PROPAGATION INSIDE THE CRYSTAL: SELFCOLLIMATION IN 3D.

Wave beams diverge when they propagate in homogeneous materials due to diffraction. Nevertheless, a particular regime where diffraction spreading vanishes, the so-called self-collimation, was predicted a decade ago for electromagnetic waves propagating in optically periodic materials (photonic crystals) [1]. Inside a photonic crystal the dispersion relations for propagation (Bloch) modes are modified, and the envelopes of electromagnetic waves can propagate without diffraction broadening [2]. The vanishing of diffraction in the wave propagation along periodic crystals has been so far experimentally demonstrated for electromagnetic waves in optical [1] and microwave [3] frequencies, and recently, for the ultrasonic beam propagation inside a sonic crystal [4]. Most of the beam propagation effects, in particular the self-collimation effect, have been addressed mainly in two-dimensional (2D) systems. The three-dimensional (3D) systems are more complicated not only for the experimental study but also in the numerical level, where the FDTD calculations are extremely time consuming. From the experimental point of view, the 3D self-collimation has been observed only for microwaves [3] but never for the optical frequencies neither other than electromagnetic waves, i.e. the matter waves, or the sound waves. We demonstrate the 3D self-collimation effect in acoustics, i.e. the nondifractive propagation of an ultrasonic beam through a 3D sonic crystal.

The sonic crystal used in the experiment can be considered as formed by two squared 2D structures like that studied in [4,5], rotated by 90 degrees and interlaced one into another (Figure 1). Each of them are formed by 20x20 steel cylinders with a radius r =

0.8 mm. The lattice constant is $a_x = a_y = a = 5.25$ mm where a_x, a_y are the spatial periods along x and y direction respectively. The beam is propagated along the z direction inside the crystal.

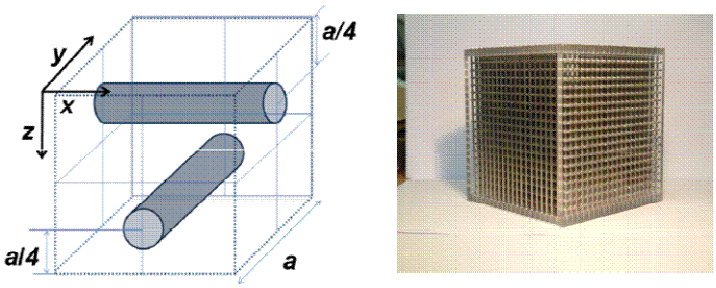

Figure 1- Unit cell scheme (left) and photograph (right) of the crystal used in the experimental setup.

Figure 2 shows the effect of the crystal on the propagation of the beam. Fig. 2(a) shows the sound intensity distributions in the transversal planes just after transducer, i.e. at a distance of 3 mm from the transducer plane. Fig. 2(b) shows the distributions in a free (without crystal) propagation over the distance of 115 mm, respectively. The propagated beam is slightly anisotropic, i.e. is slightly broader in the horizontal direction because the adapting layer of the emitting transducer has a certain curvature (astigmatism) in that plane, acting as a cylindrical diverging lens. Fig. 2(c) shows the amplitude profile of the sound beam at the rear face of the crystal, measured at the same 115 mm distance as in Fig. 2(b). The diameter of the central part of the beam remains nearly of the same order than the input (just slightly broadened), clearly indicating the effect of self-collimation. Besides the central self-collimated beam, the side-lobes appear which correspond to the diverging wave vectors. The side-lobes are related with the excitation of the additional Bloch modes (in addition to the basic subdifractive one), and require a separate study. We note that these side-lobes disappear after the larger distances behind the sonic crystal (not shown).

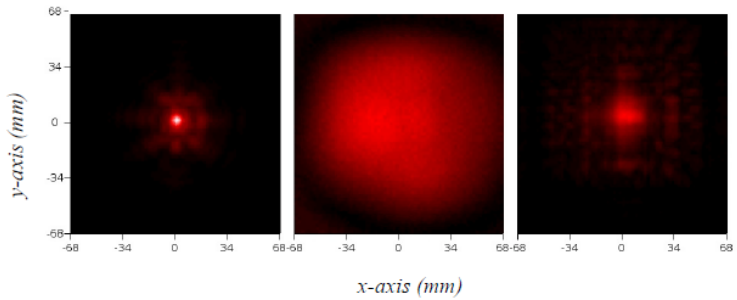

Figure 2.- Transverse profile of the ultrasonic beam measured at (a) 3 mm from the trasducer, (b) at 115 mm from the trasducer in free propagation and (c) at the crystal output located at 115 mm from the trasducer, after propagating through the crystal.

PROPAGATION BEHIND THE SONIC CRYSTAL: FOCUSING AND FILTERING OF THE BEAM.

The modification of the spatial dispersion can also lead to the super-refraction, and to the lensing and super-lensing (subwavelength focusing), of light [6] and sound [7].

The effects of lensing and super-lensing are, however, often treated inconsistently, in optics, as well as in acoustics. Usually the band structure and spatial dispersion curves (isolines of frequency) are first calculated, basing on the Bloch-wave theory. Then, depending on the slopes of the spatial dispersion curves the effective refraction index is calculated. Based on the calculated effective refraction index the geometric ray approach is applied, and the images of point sources are obtained.
Some clarity must be brought into the problem of the lensing effects in PC or SC materials. This work aims to clarify the questions related with the focusing of sound beams behind the sonic crystal. Considering the spectral width of the beam and the dispersion curves of the crystal we distinguish three different propagative regimes (Fig.3). In particular we calculate the focal distances, the beam width and the quality of the beam at the waist (in the focal spot). These evaluations are checked by the FDTD calculations, as well as by experimental measurements.

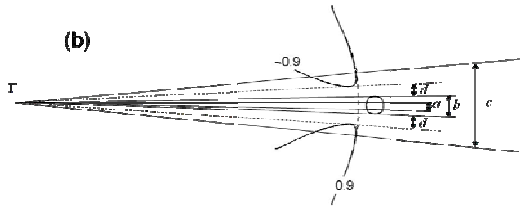

Fig. 3- The width of the spatial spectra of the beams are shown corresponding to the different considered regimes: a) broad beams with spatial spectra inside the "parabolic" area, b) intermediate width, with spatial spectra filling the full isoline of the given band; c) narrow beams with the spatial spectra extending over isolines from the neighboring bands. Finally, the region denoted by d) corresponds to forbidden angles (band gaps in space spectra domain).Continuous lines correspond to a fixed value frequency contour in different bands.

Region a). Broad Gaussian beam. No distortion. The width of the beam at the focal point is always the same as the width of the initial beam.

Region b). Beams of intermediate width. The off axis components acquire a nonparabolic phase shift, so the beam is focused at the same distance as follows from model a, however the width at the waist is not the same as at the incident in the SC.

Region c). Not only the phase of the beam (in the spatial spectrum domain) is distorted, but also its amplitude. The spatial spectrum components are removed (filtered out) at some values, corresponding to the angular band-gap (region *d* in Fig. 1(b)). This results to the complicated waist around the focal point.

These three propagation regimes are shown in figure 4 both from the result of numerical simulations and experimental measurements (D is the diameter of the ultrasonic source)

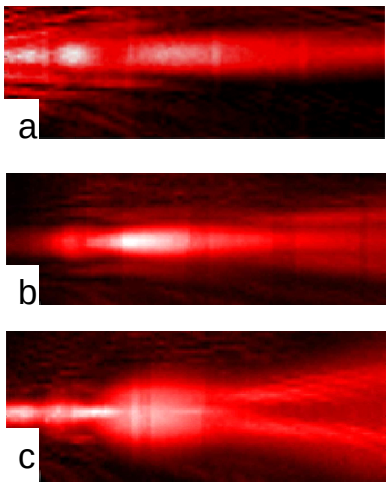

Fig.4a- Experimental measurements for frequencies: 255 KHz (a), 240 KHz (b) and 225 KHz (c). D ~5 a

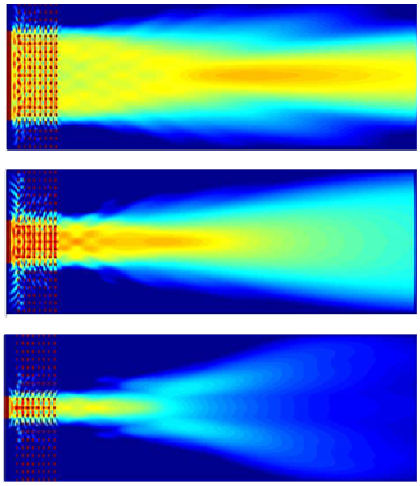

Fig.4b-Numerical simulations at. 240 KHz for different source sizes: D = 8a (a) , D = 4a (b), D = 2a (c) .

REFERENCES

[1] H. Kosaka, et al., Appl. Phys. Lett., **74**, 1212 (1999).
[2] J.Witzens, M. Loncar and A. Scherer, IEEE J. Sel. Top. Quantum Electron.,8, 1246-57 (2002); D.N. Chigrin et al., Opt. Express, **11**, 1203-11 (2003).
[3] Z. Lu et al., Phys. Rev. Lett., 96,173902 (2006).
[4] V. Espinosa et al., Phys. Rev. B, **76**, 140302 (2007).
[5] I. Pérez-Arjona, et al., Phys. Rev. B, **75**, 1098-0121(2007).
[6] Luo, C. *et al.*,*Phys. Rev. B* **68,** 045115 (2003).
[7] V. Laude, et al. , Appl. Phys. Lett. **92**, 094104 (2008).

Finite Element Studies of Permittivity Constants in Piezoceramic Disks

Magne Aanes and Magne Vestrheim
Acoustic group, Department of Physics and Technology, University of Bergen

SUMMARY

Permittivity constants are important for describing electrical and electroacoustical properties of piezoceramic disks. The following permittiviy constants are used in describing piezoceramic disks at high Diameter to Thickness (D/T) - ratios [1] when the material is poled in the thickness direction: the permittivity constant at constant stress, ϵ_{33}^T, the planar permittivity constant, ϵ_{33}^P, and the permittivity constant at constant strain ϵ_{33}^S. For piezoelectric materials such as lead zirconium titanate ceramics these permittivity constants are connected by the planar and the thickness extensional coupling factors, k_p and k_t [1]:

$$\epsilon_{33}^P = \epsilon_{33}^T(1-k_p^2),$$
$$\epsilon_{33}^S = \epsilon_{33}^T(1-k_p^2)(1-k_t^2).$$

Simplified one-dimensional (1D) models for radial modes [1] [2] and thickness extensional modes [1] have been used to describe electrical properties (Z,Y). These models are expressed with the permittivity constants mentioned, in addition to elastic and piezoelectric constants for the material. Z is the electrical input impedance, $Z = R+iX$, and Y the admittance, $Y = G+iB$. Some limiting values for these models can be found: For the radial modes model:
when $f \to 0$, $Y = i\omega C_0^T = i\omega\frac{\pi a^2 \hat{\epsilon}_{33}^T}{T}$, and when $f \to \infty$, $Y = i\omega C_0^P = i\omega\frac{\pi a^2 \hat{\epsilon}_{33}^P}{T}$.
For the thickness extensional modes model:
when $f \to 0$, $Y = i\omega C_0^P = i\omega\frac{\pi a^2 \hat{\epsilon}_{33}^P}{T}$, and when $f \to \infty$, $Y = i\omega C_0^S = i\omega\frac{\pi a^2 \hat{\epsilon}_{33}^S}{T}$,
where complex material constants, denoted by $\hat{}$, have been used to represent also effects of dielectric, elastic and piezoelectric material losses [3] [4]. T is the thickness of the disk and a is the radius. C_0^T, C_0^P and C_0^S are defined from the above expressions. I.e. for the permittivity constants the following notation is used [3] [4] $\hat{\epsilon} = \epsilon' - i\epsilon'' = \epsilon(1 - i/Q^\epsilon) = \epsilon(1 - i\tan\delta)$.

In the present work the electrical properties of piezoelectric disks are studied including the behaviour towards the limiting values mentioned above, by using finite element (FE) simulations and measurements. The FE modelling program FEMP U3.2 [5] is used for the simulations. In order to facilitate such comparisons with the limiting values, the electrical conductance, G, and susceptance, B, are reformulated through a so-called "generalized" permittivity constant and associated Q-value by:

$$\epsilon^{GEN} = B\frac{T}{\pi a^2 i\omega},$$
$$Q_{GEN}^\epsilon = \frac{B}{G}.$$

In the FE simulations adjusted material data [6] [7] [8] for Pz27 [9] disks are used in order to obtain a closer agreement with measurements.

In the results a frequency × thickness (fT) versus D/T type of eigen frequency spectrum is calculated for Pz27 disks for a fT range from 0 to 3000 [kHz mm] and a D/T range from 0 to 35. This represents extended ranges compared to similar plots for other materials presented elsewhere, e.g [5] [7], where a fT range of 0 to 2200 [kHz mm] and a D/T range of 0 to 25 were used. For the spesific results and further discussions it is referred to [10].

Results for ϵ^{GEN} and Q_{GEN}^ϵ as a function of frequency are presented for Pz27 disks of D/T ≈ 10 and 25 with comparisons between the theoretical models and measurements. For low frequencies ($f \to 0$) a good agreement with the limiting values can be found for both D/T - ratios. FE simulations in the range between the first radial mode and the edge mode demonstrate a variation of ϵ^{GEN} around the ϵ_{33}^P value,

and where the average of the peak and lowest value for each resonance can get within a few per cent of the ϵ_{33}^P value. Similar behaviour is not shown for Q_{GEN}^{ϵ} and the $Q_{33}^{\epsilon^P}$. These behaviours are interesting to investigate further. For much higher frequencies than the first thickness extensional mode, both the FE simulations and measurements are too limited to reach the limiting values of ϵ_{33}^S and $Q_{33}^{\epsilon^S}$. However, the tendency of the results covering up to above the third thickness extensional mode is in agreement with that of the 1D model for thickness modes. Thus to get within a few per cent of the limiting values will require results over an extended frequency range. The specific results and further discussions will become available in [10].

References

[1] *IEEE Standard on Piezoelectricity 176-1987.* The Institute of Electrical and Electronics Engineers, Inc 345 East 47th Street, New York, NY 10017, USA, 1988.

[2] A. H. Meitzler, J. Henry M. O'Bryan, and H. F. Tiersten, "Definition and measurement of radiel mode coupling factors in piezoelectric ceramic materials with large variations in poisson's ratio," *IEEE Transactions on sonics and ultrasonics*, vol. SU-20, No. 3, pp. 233–239, July 1973.

[3] R. Holland, "Representation of dielectric, elastic, and piezoelectric losses by complex coefficients," *IEEE Transactions on sonics and ultrasonics*, vol. SU-14, no. 1, January 1967.

[4] M. Vestrheim, "Phys 373 - akustiske målesystemer - forelesningsnotater," Spring 2008, [course at Department of Physics and Technology, University of Bergen].

[5] J. Kocbach, "Finite element modeling of ultrasonic piezoelectric transducers," Ph.D. dissertation, Department of Physics, University of Bergen, September 2000.

[6] K. D. Lohne, "Undersøkelse og utnyttelse av svingemoder i ultralyd transduserkonstruksjoner," Master's thesis, Department of Physics and Technology, University of Bergen, May 2005, [in Norwegian].

[7] R. Fardal, "Endelig element analyse av elektriske egenskaper til piezoelektriske skiver," Master's thesis, Department of Physics, University of Bergen, 9. January 2002, [in Norwegian].

[8] V. Knappskog, "Radiellmode svingninger i piezoelektriske ultralydtransdusere for luft. målinger og endelig element analyser." Master's thesis, Department of Physics and Technology, University of Bergen, October 2007, [in Norwegian].

[9] Ferroperm piezoceramics a/s. [Online]. Available: http://www.ferroperm-piezo.com/

[10] M. Aanes, Master's thesis, Department of Physics and Technology, University of Bergen, May 2009, [in Norwegian].

Analysis of echoes from a plane reflector - steps towards acoustic habitat mapping

What is in an echo?

Halvor Hobæk and Anja Heggen
halvor.hobak@ift.uib.no

Department of Physics and Technology
University of Bergen, Norway

32th Scandinavian symposium on Physical Acoustics, Finse, 10 February 2009

Outline

Introduction
Theory
Simulations
Experiment
Discussion

Motivation

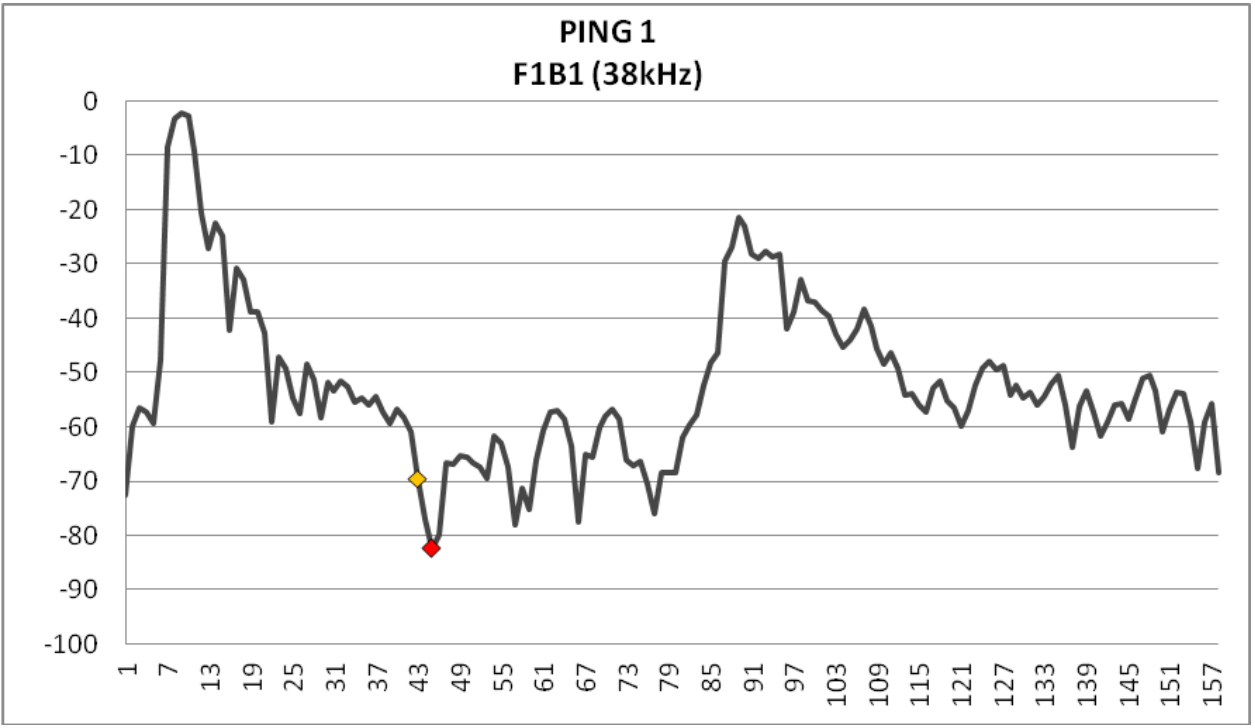

- Sample from vertical echo sounder
  38 kHz, sand bottom at 15m

Motivation

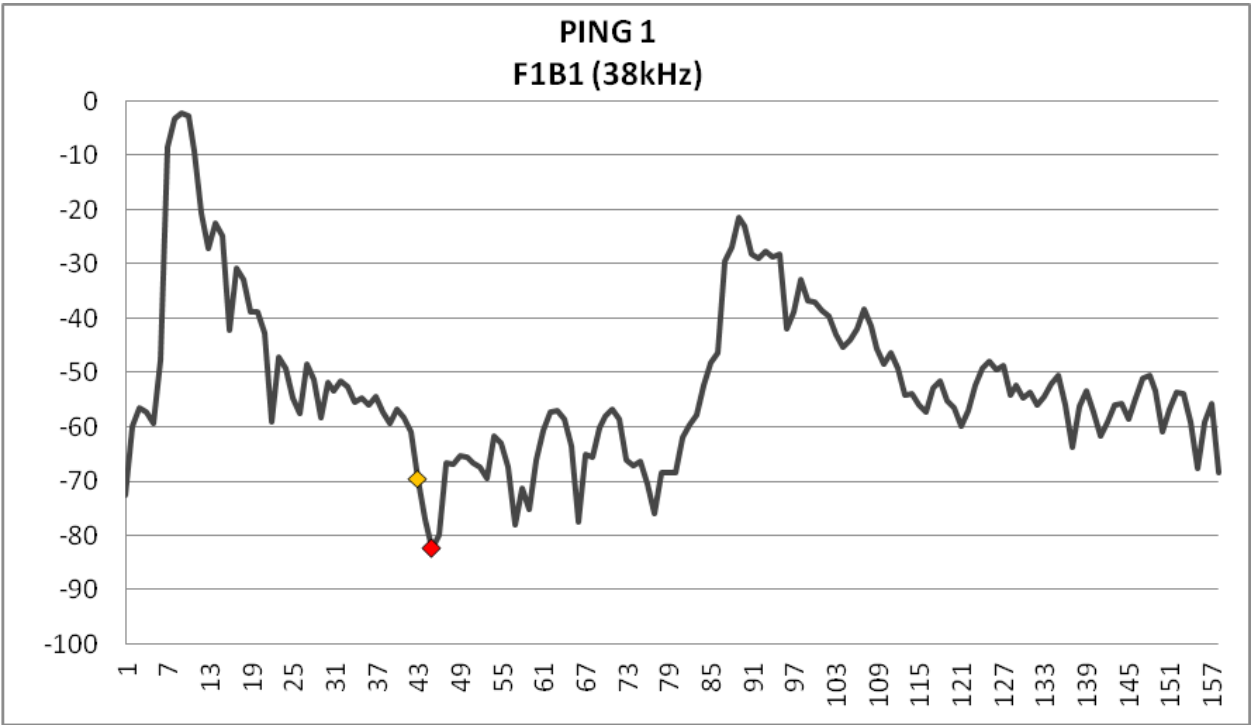

- Sample from vertical echo sounder
  38 kHz, sand bottom at 15m
- The big dips indicate destructive interference: coherent scattering

Motivation

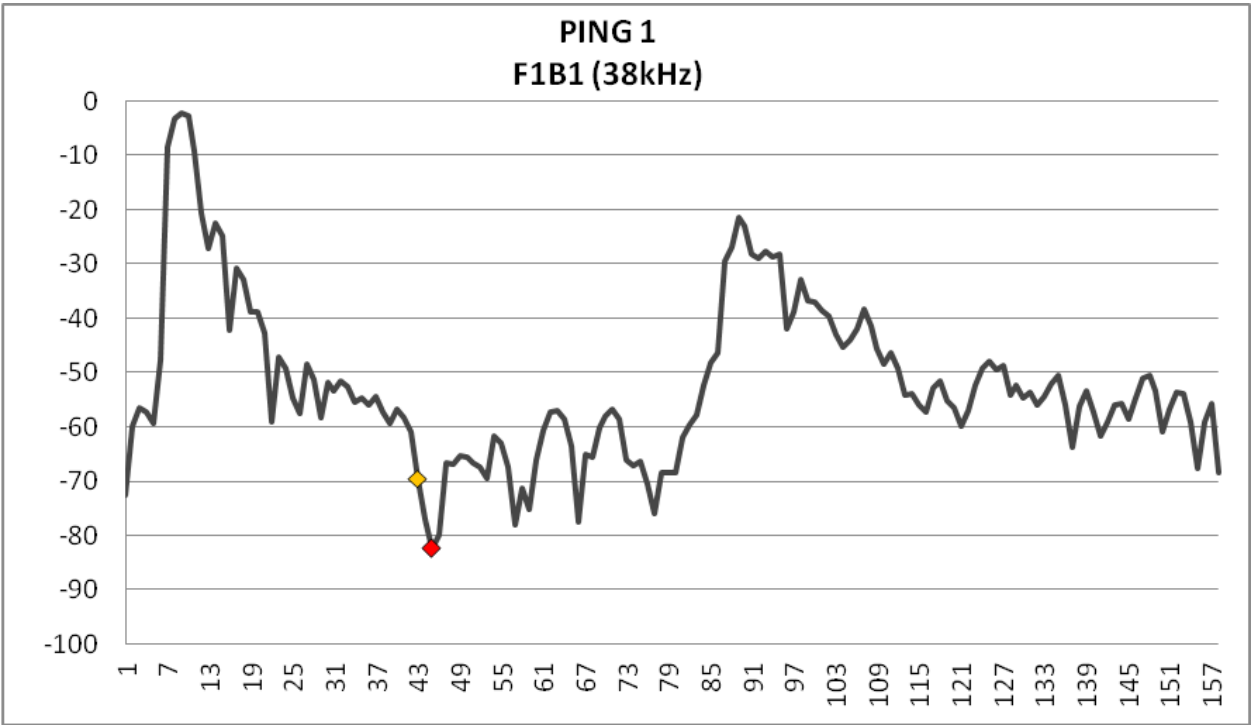

- Sample from vertical echo sounder
  38 kHz, sand bottom at 15m
- The big dips indicate destructive interference: coherent scattering
- In this presentation we focus on modelling and measuring **coherent** reflection

Echo sounder

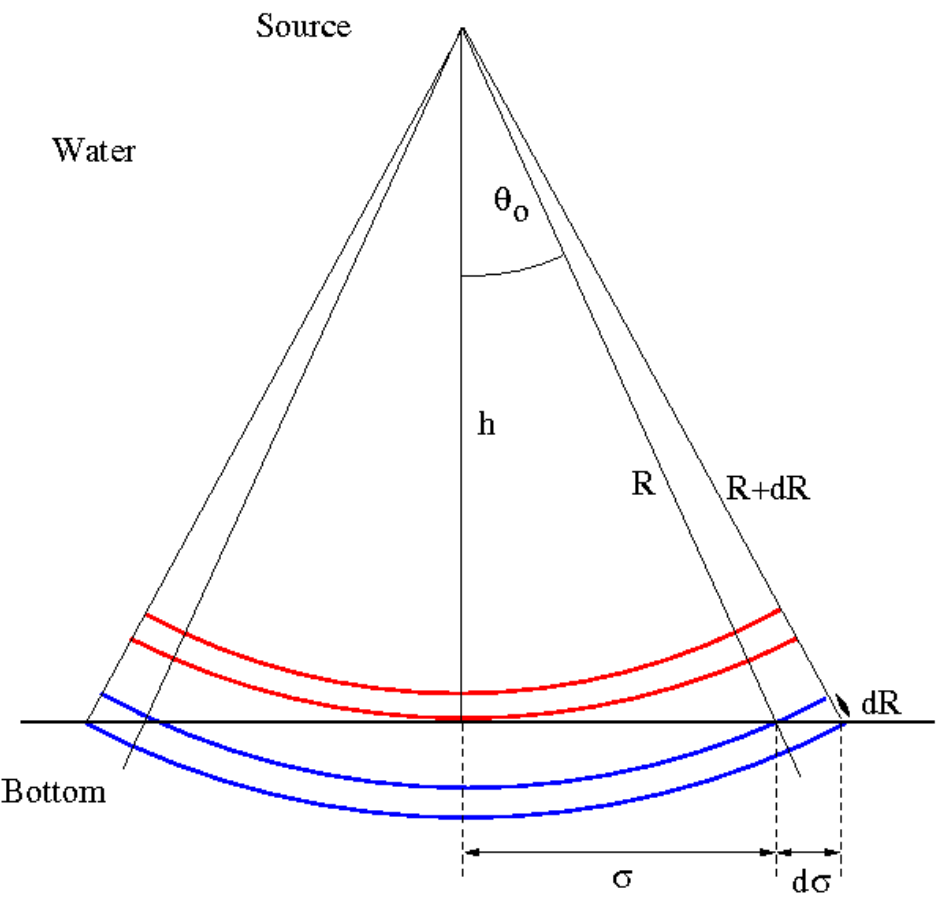

- Schematic of a burst hitting the bottom

Echo sounder

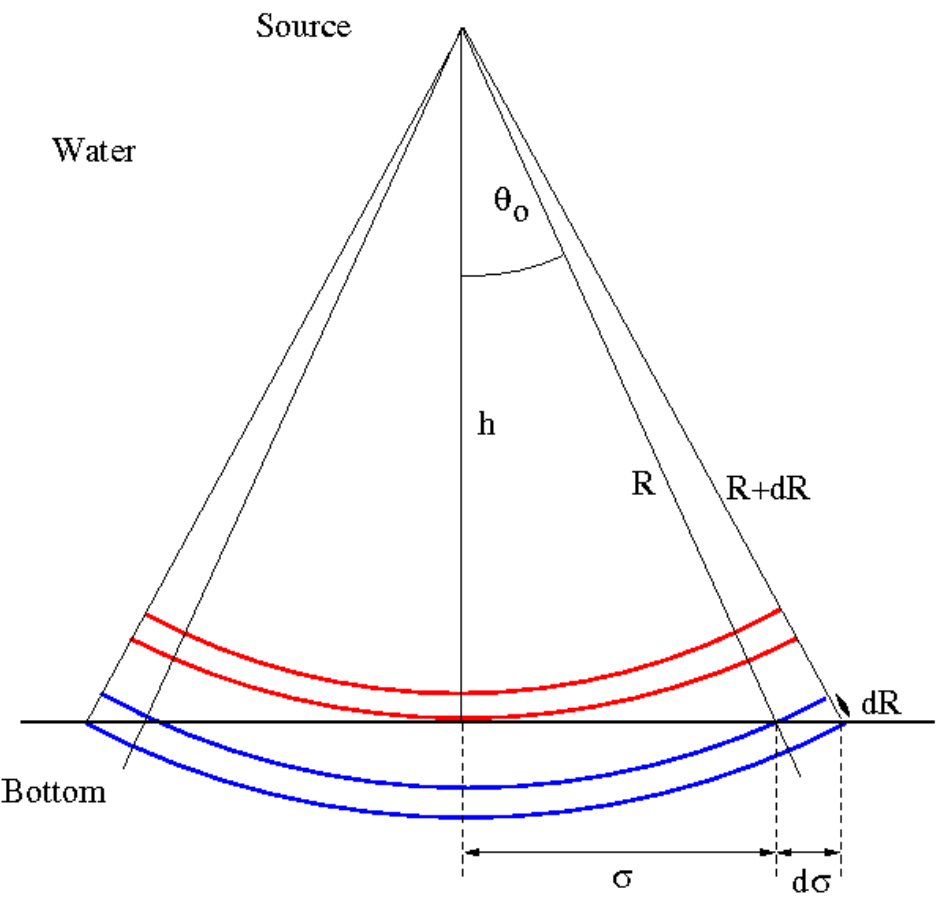

- Schematic of a burst hitting the bottom
- As time passes first a circle is filled with sound

Echo sounder

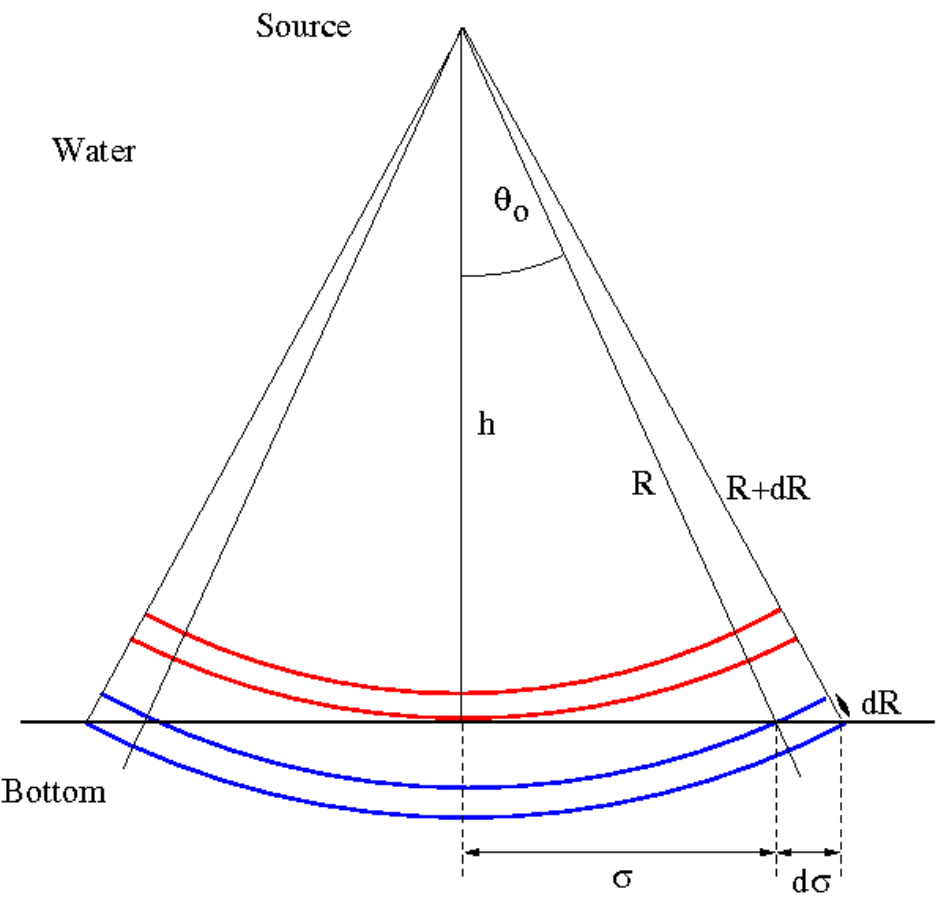

- Schematic of a burst hitting the bottom
- As time passes first a circle is filled with sound
- Then it expands to a widening ring

Echo sounder

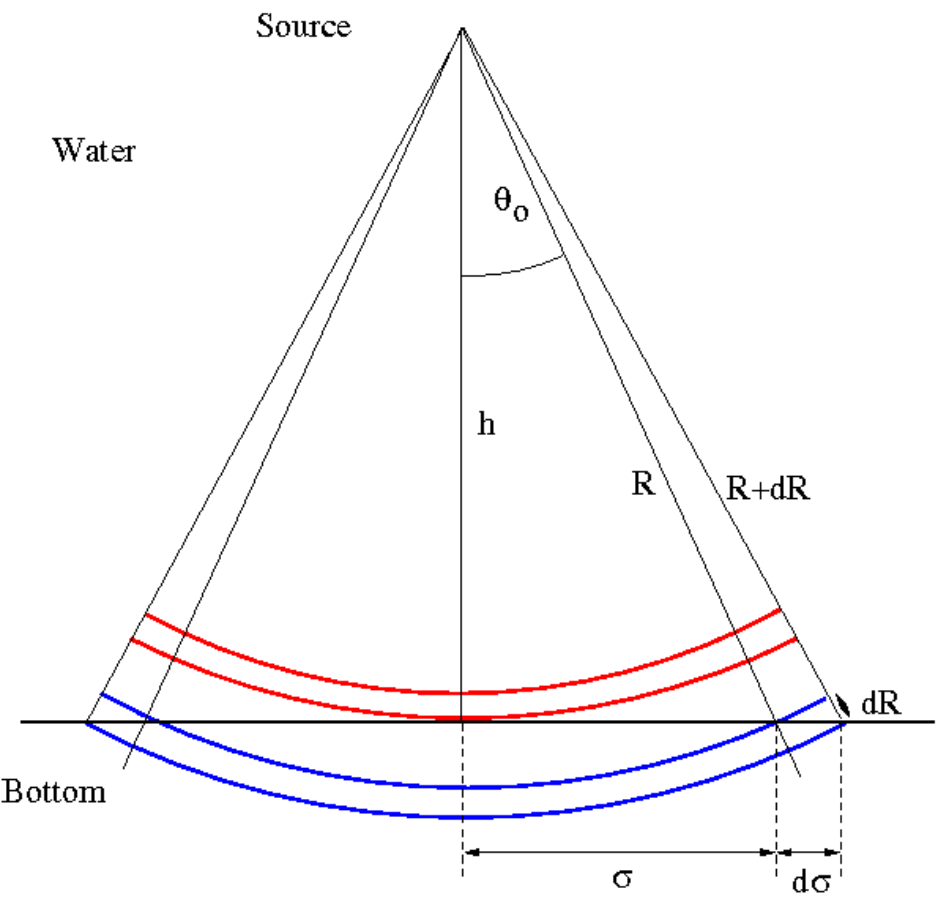

- Schematic of a burst hitting the bottom
- As time passes first a circle is filled with sound
- Then it expands to a widening ring
- Since $\sigma d\sigma = RdR$ the ring area is proportional to R

Echo sounder

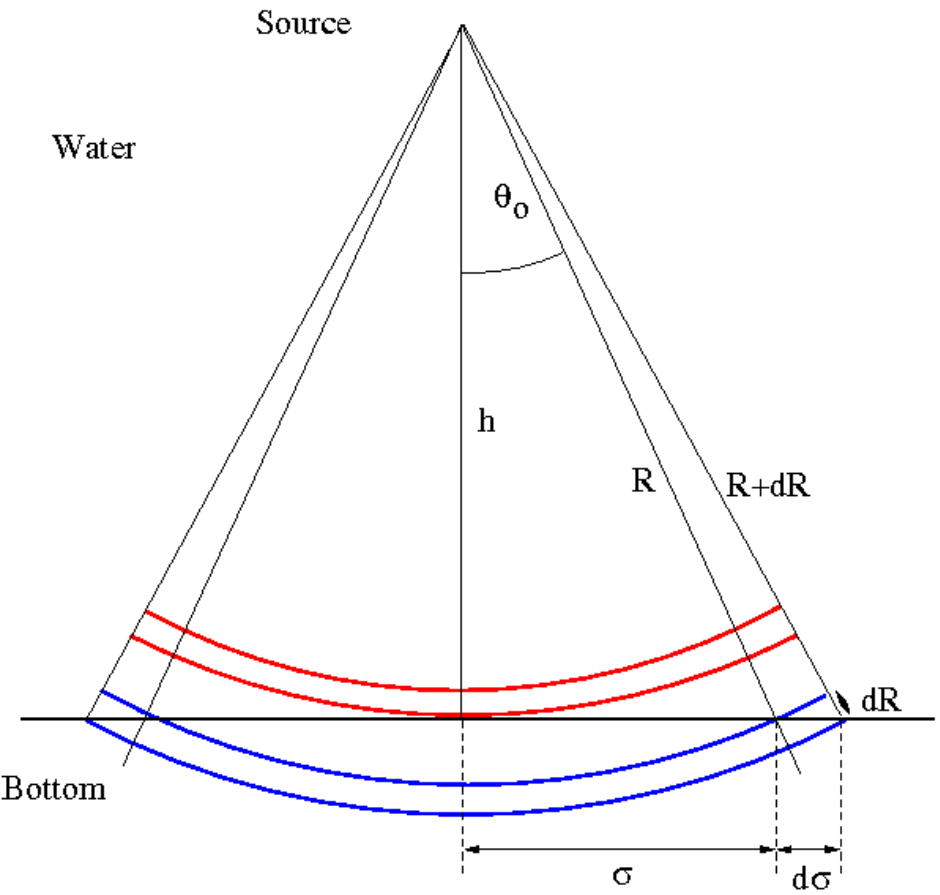

- Schematic of a burst hitting the bottom
- As time passes first a circle is filled with sound
- Then it expands to a widening ring
- Since $\sigma d\sigma = RdR$ the ring area is proportional to R
- Object: to calculate the reflected field at the source

Incident wave

We assume a directive sound beam in the far-field:

$$p_{inc} = p_0 \frac{r_0}{R} D(\theta) e^{i(kR-\omega t)} f(R - ct)$$

where p_0 is pressure at reference range r_0, R is range, $D(\theta)$ is directivity function, $f(R - ct)$ is envelope of the pulse, k is wave number, ω angular frequency and t is time.
It is also useful to substitute $e^{i(kR-\omega t)} f(R - ct)$ with a measured burst when comparing to experimental results.

Reflected field

Helmholtz-Kirchhoff:

$$p(\mathbf{r}) = \int_S (G(\mathbf{r}, \mathbf{r}')\nabla_0 p(\mathbf{r}') - p(\mathbf{r}')\nabla' G(\mathbf{r}, \mathbf{r}')) \cdot d\mathbf{S}$$

where $G(\mathbf{r}, \mathbf{r}')$ is the Greens function, and $\mathbf{r}'$ refers to the surface S, assumed to consist of a plane and a hemisphere (at infinity).
Assuming $G(\mathbf{r}, \mathbf{r}') = 0$ on the plane (Dirichlet condition) the integral reduces to

$$p_{\mathbf{r}} = -\int_S p(\mathbf{r}')\nabla' G(\mathbf{r}, \mathbf{r}') \cdot d\mathbf{S}$$

Greens function

- A suitable Greens function is

$$G(\mathbf{r},\mathbf{r}') = \frac{e^{ikR_1}}{4\pi R_1} - \frac{e^{ikR_2}}{4\pi R_2},$$

where $R_1 = |\mathbf{r} - \mathbf{r}'|$ and $R_2 = |\mathbf{r} - \mathbf{r}''|$. This is found by the "mirror" method: $\mathbf{r}' = \sigma(x', y') + z'\hat{\mathbf{z}}$, and $\mathbf{r}'' = \sigma(x', y') - z'\hat{\mathbf{z}}$. $\hat{\mathbf{z}}$ is unit vector normal to the plane, while σ(x',y') lies in the plane of the reflector.

Greens function

- A suitable Greens function is

$$G(\mathbf{r},\mathbf{r}') = \frac{e^{ikR_1}}{4\pi R_1} - \frac{e^{ikR_2}}{4\pi R_2},$$

  where $R_1 = |\mathbf{r} - \mathbf{r}'|$ and $R_2 = |\mathbf{r} - \mathbf{r}''|$. This is found by the "mirror" method: $\mathbf{r}' = \sigma(x', y') + z'\hat{\mathbf{z}}$, and $\mathbf{r}'' = \sigma(x', y') - z'\hat{\mathbf{z}}$. $\hat{\mathbf{z}}$ is unit vector normal to the plane, while σ(x',y') lies in the plane of the reflector.
- In the plane $z' = 0$, and we get $R_1 = R_2$, so that $G = 0$.

$\nabla' G$

The gradient of the Greens function is straight forward (omitting details): On the plane $R_1 = R_2 = R = \sqrt{z^2 + \sigma^2}$, and

$$\nabla' G \cdot d(\mathbf{S})|_S = \frac{2z}{R} \frac{\partial}{\partial R} (\frac{e^{ikR}}{4\pi R}) dS$$

where we have taken into account that $d\mathbf{S}$ is directed opposite $\nabla' G$.
Thus,

$$p(\mathbf{r}) = -\frac{z}{2\pi} \int_S p(\mathbf{r}') \frac{\partial}{\partial R} (\frac{e^{ikR}}{R}) dS.$$

z is height above the plane. In the integral the pressure is supposed to be that at the plane.

Vertical sound beam

Locating the source above the origin at height h, e.g. $\mathbf{r} = r(0, h)$, $R = \sqrt{h^2 + \sigma^2}$, and substituting for $\nabla' G$, and $dS = 2\pi R dR$ we find

$$p(h, t) = -h \int_h^\infty p(\mathbf{r}', t) \frac{ikR - 1}{R^2} e^{ikR} dR$$

So far no approximations have been introduced, except the assumption of monochromatic wave and semi infinite half space. (Lower limit is h because then $\sigma = 0$).
We want to apply this to a burst from a vertical sound beam.

Kirchhoff approximation

First question: What to put for p in the integral?

Kirchhoff approximation

First question: What to put for p in the integral?

- Kirchhoff approximation: use free field value!

Kirchhoff approximation

First question: What to put for p in the integral?

- Kirchhoff approximation: use free field value!
- This is not obvious. In the case of plane waves the matching conditions used at the interface is continuity of pressure and normal velocity across the interface. Then the pressure **at the interface** is $p = p_{inc}(1 + C)$, where C is the reflection coefficient.

Kirchhoff approximation

First question: What to put for p in the integral?

- Kirchhoff approximation: use free field value!
- This is not obvious. In the case of plane waves the matching conditions used at the interface is continuity of pressure and normal velocity across the interface. Then the pressure **at the interface** is $p = p_{inc}(1 + C)$, where C is the reflection coefficient.
- But this does not work! Here is why:

Elementary case

Assume the source to be omnidirectional, reflection coefficient constant, continuous waves, infinite size of interface. Direct integration gives:

- $p(h) = \frac{p_0 r_0 \mathcal{R}}{2h} e^{2ikh}$

Elementary case

Assume the source to be omnidirectional, reflection coefficient constant, continuous waves, infinite size of interface. Direct integration gives:

- $p(h) = \frac{p_0 r_0 \mathcal{R}}{2h} e^{2ikh}$
- This can alternatively be found using the mirror method!

Elementary case

Assume the source to be omnidirectional, reflection coefficient constant, continuous waves, infinite size of interface. Direct integration gives:

- $p(h) = \frac{p_0 r_0 \mathcal{R}}{2h} e^{2ikh}$
- This can alternatively be found using the mirror method!
- Clearly $\mathcal{R}$ must be the reflection coefficient C, not $1 + C$!

Elementary case

Assume the source to be omnidirectional, reflection coefficient constant, continuous waves, infinite size of interface. Direct integration gives:

- $p(h) = \frac{p_0 r_0 \mathcal{R}}{2h} e^{2ikh}$
- This can alternatively be found using the mirror method!
- Clearly $\mathcal{R}$ must be the reflection coefficient C, not $1 + C$!
- Further, to agree with plane wave incidence, letting $h \to \infty$, it seems natural that C should be reflection coefficient at normal incidence. ???!

Vertical sound beam - 2

Putting $p = p_{inc}$, as given above, in the integral, and substitute $dS = 2\pi R dR$, we find

- $p(h,t) = -hp_0 r_0 \int_h^\infty \mathcal{R}(R) D(R) \{ik - 1/R\} \frac{e^{2ikR}}{R^2} f(R - ct) dR$

Vertical sound beam - 2

Putting $p = p_{inc}$, as given above, in the integral, and substitute $dS = 2\pi R dR$, we find

- $p(h,t) = -hp_0 r_0 \int_h^\infty \mathcal{R}(R) D(R) \{ik - 1/R\} \frac{e^{2ikR}}{R^2} f(R - ct) dR$
- Alternatively, express time in terms of R, e.g. compute $p(R)$ as the sound propagates:

Vertical sound beam - 2

Putting $p = p_{inc}$, as given above, in the integral, and substitute $dS = 2\pi R dR$, we find

- $p(h,t) = -hp_0 r_0 \int_h^\infty \mathcal{R}(R) D(R) \{ik - 1/R\} \frac{e^{2ikR}}{R^2} f(R - ct) dR$
- Alternatively, express time in terms of R, e.g. compute $p(R)$ as the sound propagates:
- $p(h,R) = -hp_0 r_0 \int_h^R \mathcal{R}(R) D(R) f(R) \{ik - 1/R\} \frac{e^{2ikR}}{R^2} dR$

Vertical sound beam - 2

Putting $p = p_{inc}$, as given above, in the integral, and substitute $dS = 2\pi R dR$, we find

- $p(h,t) = -hp_0 r_0 \int_h^\infty \mathcal{R}(R) D(R) \{ik - 1/R\} \frac{e^{2ikR}}{R^2} f(R - ct) dR$
- Alternatively, express time in terms of R, e.g. compute $p(R)$ as the sound propagates:
- $p(h,R) = -hp_0 r_0 \int_h^R \mathcal{R}(R) D(R) f(R) \{ik - 1/R\} \frac{e^{2ikR}}{R^2} dR$
- Here we have kept the possibility that $\mathcal{R}$ depends on the incidence angle

Burst

Even if a monoharmonic wave was assumed, a reasonable approximation is to modulate the amplitude with a shape function $f(r - ct)$. Note that in terms of R this function, if expressed in time domain, must be reversed!

- In our first attemt to compute the reflected pressure the kernel in the integral:

$$K = \mathcal{R}(R)D(R)\{ik - 1/R\}\frac{e^{2ikR}}{R^2}$$

was computed once and for all, and integrated over the burst duration while letting $f(R)$ slide along the kernel

Burst

Even if a monoharmonic wave was assumed, a reasonable approximation is to modulate the amplitude with a shape function $f(r - ct)$. Note that in terms of R this function, if expressed in time domain, must be reversed!

- In our first attemt to compute the reflected pressure the kernel in the integral:

$$K = \mathcal{R}(R)D(R)\{ik - 1/R\}\frac{e^{2ikR}}{R^2}$$

  was computed once and for all, and integrated over the burst duration while letting $f(R)$ slide along the kernel
- This turned out wrong, because then the phase moved through the burst

Burst - 2

Better results were obtained by putting the kernel

$$K = \mathcal{R}(R)D(R)\{ik - 1/R\}\frac{e^{ikR}}{R^2},$$

and combining $e^{ikR}f(R)$ to form the sliding burst

- In the following we shall show simulations made with a rectangular burst shape and a smoothed one, with exponential rise and decay.

Burst - 2

Better results were obtained by putting the kernel

$$K = \mathcal{R}(R)D(R)\{ik - 1/R\}\frac{e^{ikR}}{R^2},$$

and combining $e^{ikR}f(R)$ to form the sliding burst

- In the following we shall show simulations made with a rectangular burst shape and a smoothed one, with exponential rise and decay.
- The amplitude is normalized with respect to the elementary example presented above, assuming total reflection

Simulations

- The rise time was selected in terms of a *Q*-factor. In the example the rectangular burst has 10 cycles of 5 MHz, the *Q*-factor is 5, and the number of samples per wavelength is 20 in the integration.The total length of the smoothed burst corresponds to 18 periods

Simulations

- The rise time was selected in terms of a Q-factor. In the example the rectangular burst has 10 cycles of 5 MHz, the Q-factor is 5, and the number of samples per wavelength is 20 in the integration.The total length of the smoothed burst corresponds to 18 periods
- The half power beamwidth is 7^o

Simulations

- The rise time was selected in terms of a Q-factor. In the example the rectangular burst has 10 cycles of 5 MHz, the Q-factor is 5, and the number of samples per wavelength is 20 in the integration.The total length of the smoothed burst corresponds to 18 periods
- The half power beamwidth is 7^o
- The distance to the copper reflector is 15 cm, and the plane wave reflection coefficient for oblique incidence was used

Simulations

- The rise time was selected in terms of a Q-factor. In the example the rectangular burst has 10 cycles of 5 MHz, the Q-factor is 5, and the number of samples per wavelength is 20 in the integration.The total length of the smoothed burst corresponds to 18 periods
- The half power beamwidth is 7^o
- The distance to the copper reflector is 15 cm, and the plane wave reflection coefficient for oblique incidence was used
- If the source is to act as a receiver, its directivity function on reception must also be accounted for. Thus, in the integral D^2 is used instead of D

Simulation results

Burst shapes: note time reversed, time axis is actually range

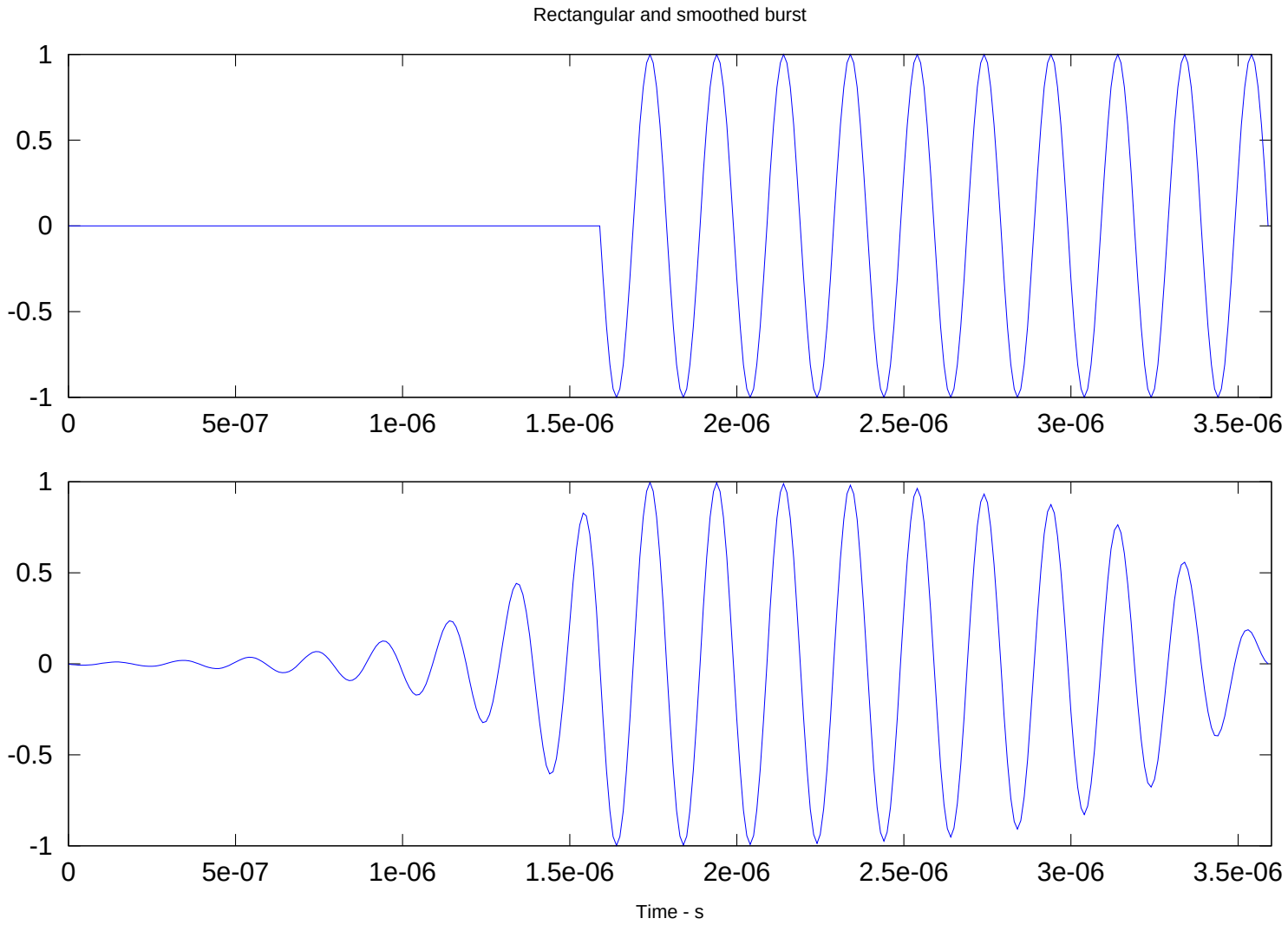

Simulation results

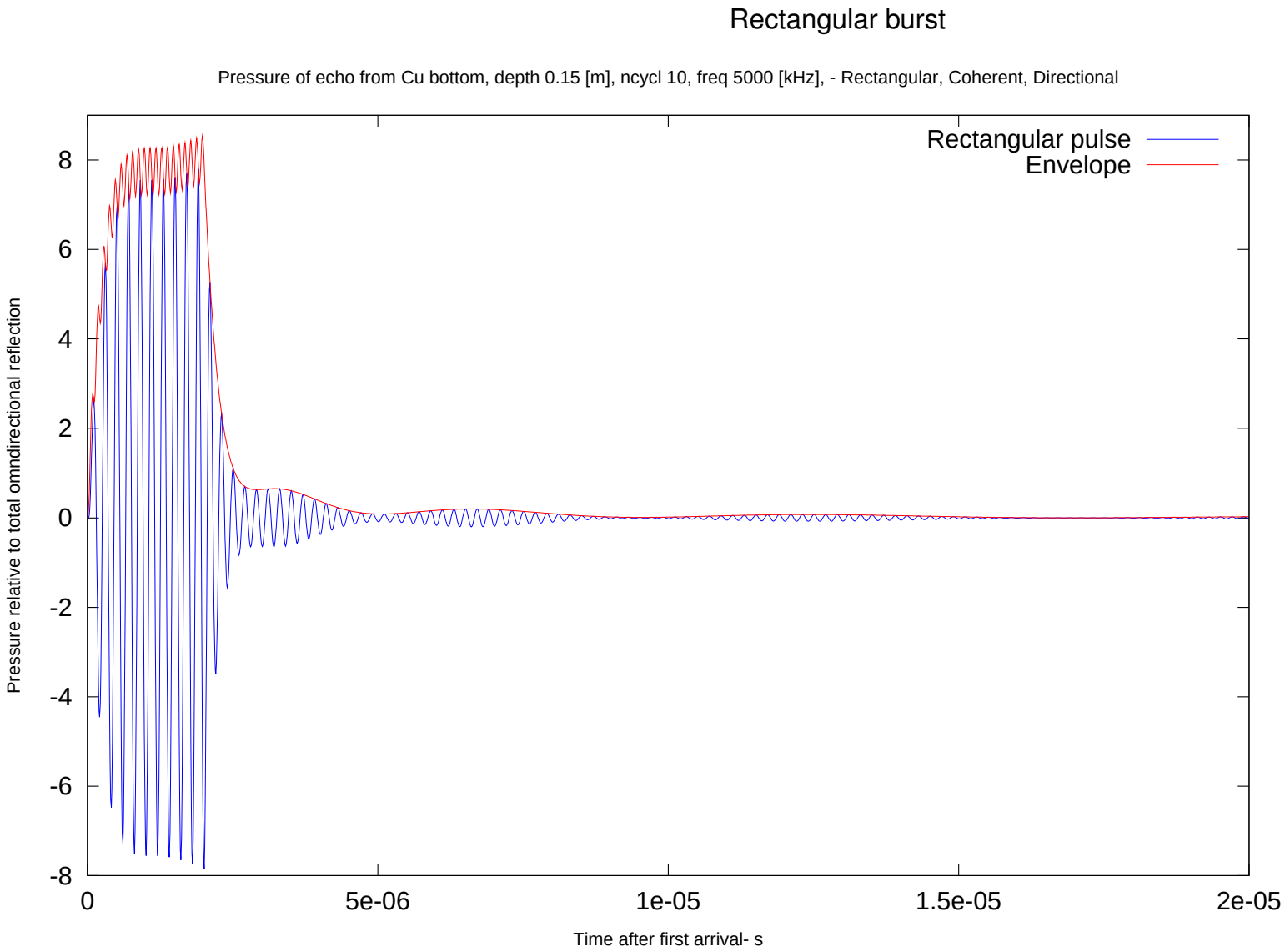

Simulation results

Q-shaped burst

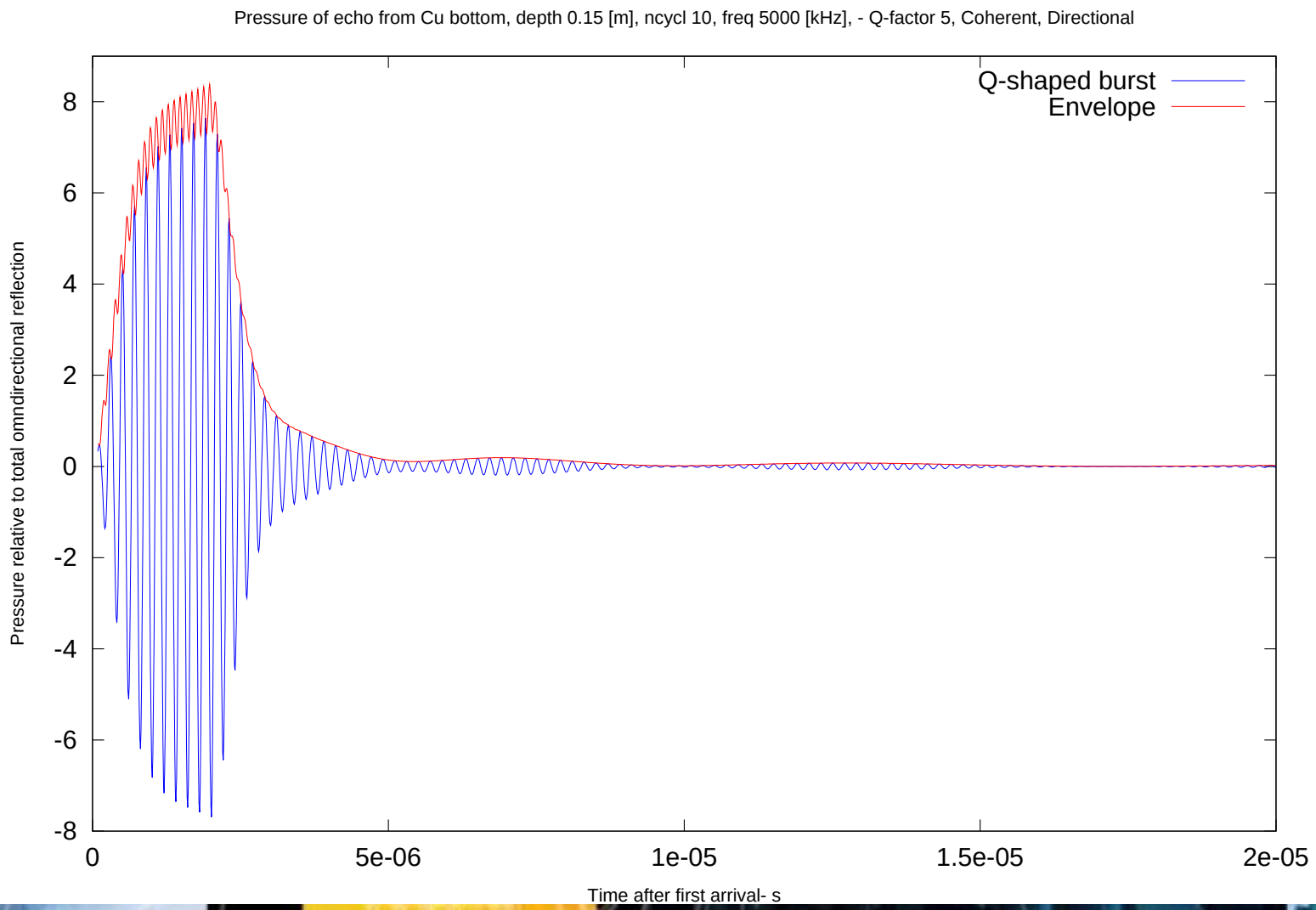

Simulation results

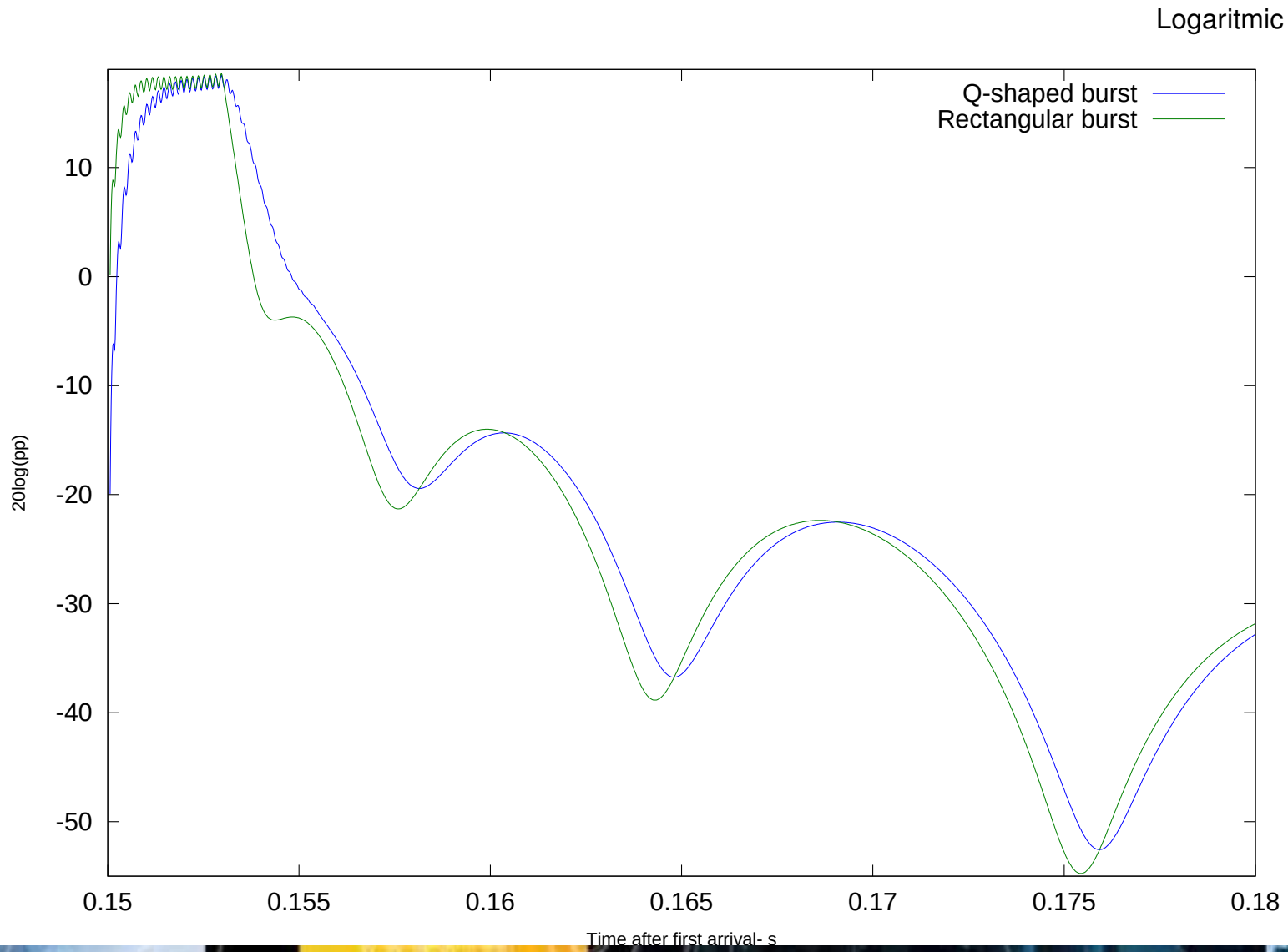

Comments

Are the results reasonable?

Comments

Are the results reasonable?

- No!

Comments

Are the results reasonable?

- No!
- Amplitude is wrong: Should be less than 1 after normalization. Does not vary with burst length, integration stepsize, and only little with directivity, but ...

Comments

Are the results reasonable?

- No!
- Amplitude is wrong: Should be less than 1 after normalization. Does not vary with burst length, integration stepsize, and only little with directivity, but ...
- Amplitude increases with height *h*!! - no explanation found so far.

Comments

Are the results reasonable?

- No!
- Amplitude is wrong: Should be less than 1 after normalization. Does not vary with burst length, integration stepsize, and only little with directivity, but ...
- Amplitude increases with height *h*!! - no explanation found so far.
- Also alarming: Omnidirectional burst -> long lasting reflection:

Comments

Are the results reasonable?

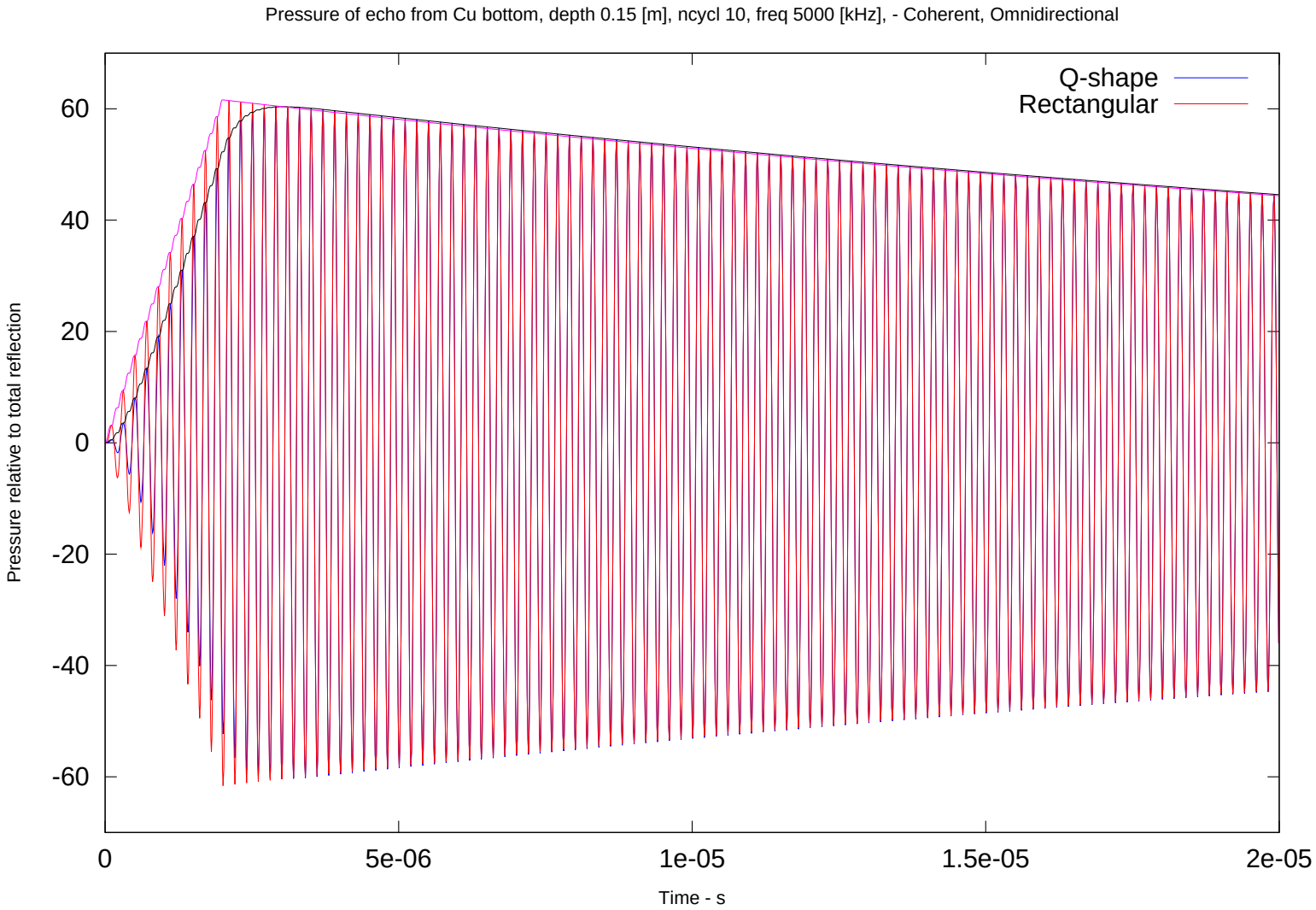

Reflection coefficient

The last plot was with $C = 1$. Plane wave, oblique incidence makes very little difference ($C_\perp = 0.931, \theta_c = 17.4^o$).

Reflection coefficient

The last plot was with $C = 1$. Plane wave, oblique incidence makes very little difference ($C_\perp = 0.931, \theta_c = 17.4^o$).

- Plane wave oblique reflection coefficient is valid in direction θ_r, not in arbitrary directions.

Reflection coefficient

The last plot was with $C = 1$. Plane wave, oblique incidence makes very little difference ($C_\perp = 0.931, \theta_c = 17.4^o$).

- Plane wave oblique reflection coefficient is valid in direction θ_r, not in arbitrary directions.
- What about Lamberts cosine law (intensity)?

Reflection coefficient

The last plot was with $C = 1$. Plane wave, oblique incidence makes very little difference ($C_\perp = 0.931, \theta_c = 17.4^o$).

- Plane wave oblique reflection coefficient is valid in direction θ_r, not in arbitrary directions.
- What about Lamberts cosine law (intensity)?
- No visible effect in our case

Reflection coefficient

The last plot was with $C = 1$. Plane wave, oblique incidence makes very little difference ($C_\perp = 0.931, \theta_c = 17.4^o$).

- Plane wave oblique reflection coefficient is valid in direction θ_r, not in arbitrary directions.
- What about Lamberts cosine law (intensity)?
- No visible effect in our case
- Temporary conclusion: Directivity limits the duration of the reflected signal

Experiment - technical details

- Sound source: Circular, Resonance frequency 5.0 MHz, diameter 2.4 mm, half power angle 7.3^o

Experiment - technical details

- Sound source: Circular, Resonance frequency 5.0 MHz, diameter 2.4 mm, half power angle 7.3^o
- Reflector: polished (to optical quality) Cu disk of thickness 5 cm, diameter 20 cm

Experiment - technical details

- Sound source: Circular, Resonance frequency 5.0 MHz, diameter 2.4 mm, half power angle 7.3^o
- Reflector: polished (to optical quality) Cu disk of thickness 5 cm, diameter 20 cm
- Reflections recorded through high pass filter (2 MHz cut off) on a LeCroy 9350 oscilloscope

Experiment - technical details

- Sound source: Circular, Resonance frequency 5.0 MHz, diameter 2.4 mm, half power angle 7.3^o
- Reflector: polished (to optical quality) Cu disk of thickness 5 cm, diameter 20 cm
- Reflections recorded through high pass filter (2 MHz cut off) on a LeCroy 9350 oscilloscope
- The distance to the copper reflector is 13.24 cm, sound axis not excactly in the center of the reflector

Experiment - technical details

- Sound source: Circular, Resonance frequency 5.0 MHz, diameter 2.4 mm, half power angle 7.3^o
- Reflector: polished (to optical quality) Cu disk of thickness 5 cm, diameter 20 cm
- Reflections recorded through high pass filter (2 MHz cut off) on a LeCroy 9350 oscilloscope
- The distance to the copper reflector is 13.24 cm, sound axis not excactly in the center of the reflector
- Sound burst recorded separately at 14 cm distance with a Precision Acoustics needle hydrophone of diameter 0.2 mm

Experiment - technical details

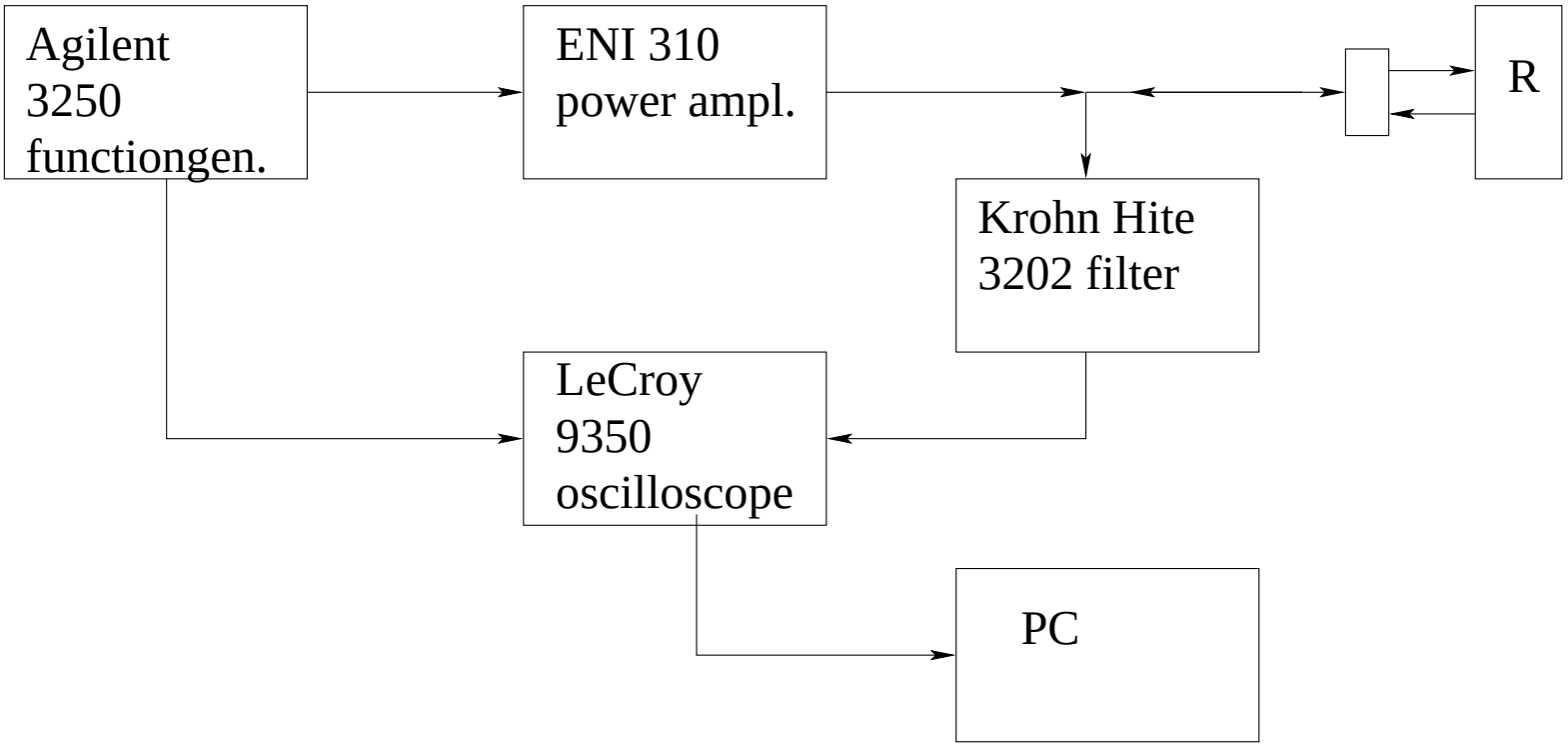

Experiment, compared to simulations

Burst

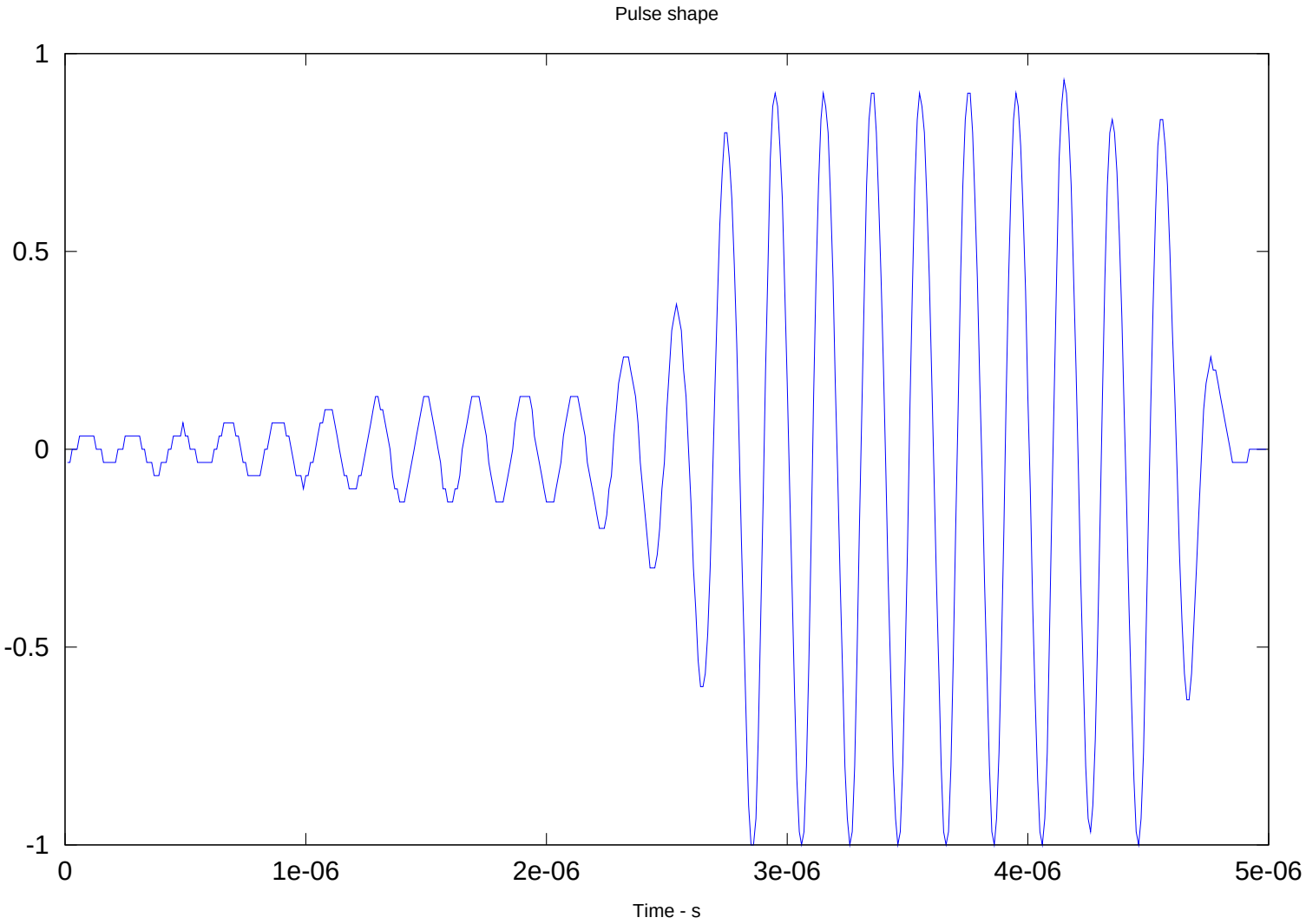

Experiment, compared to simulations

Reflected signal

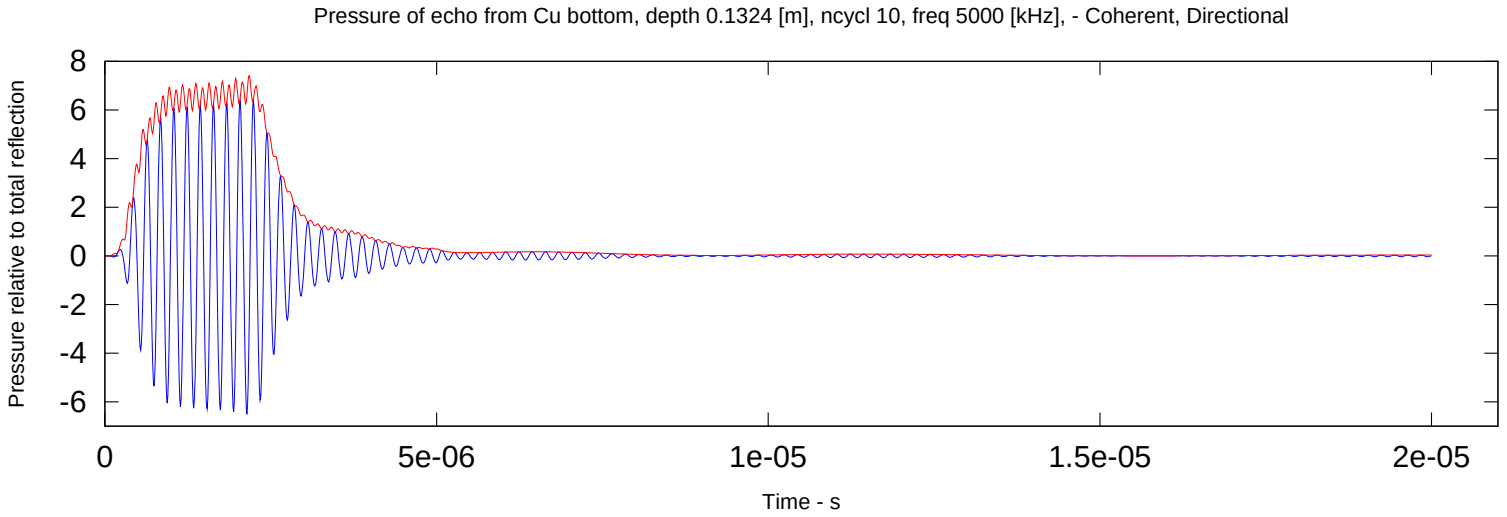

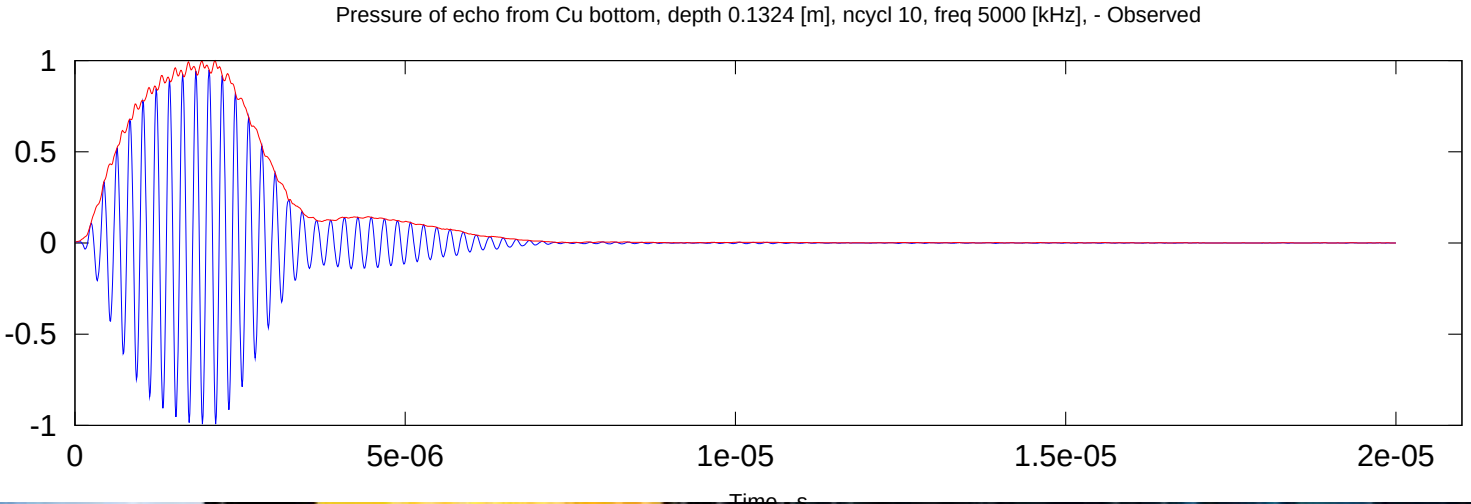

Experiment, compared to simulations

Logaritmic

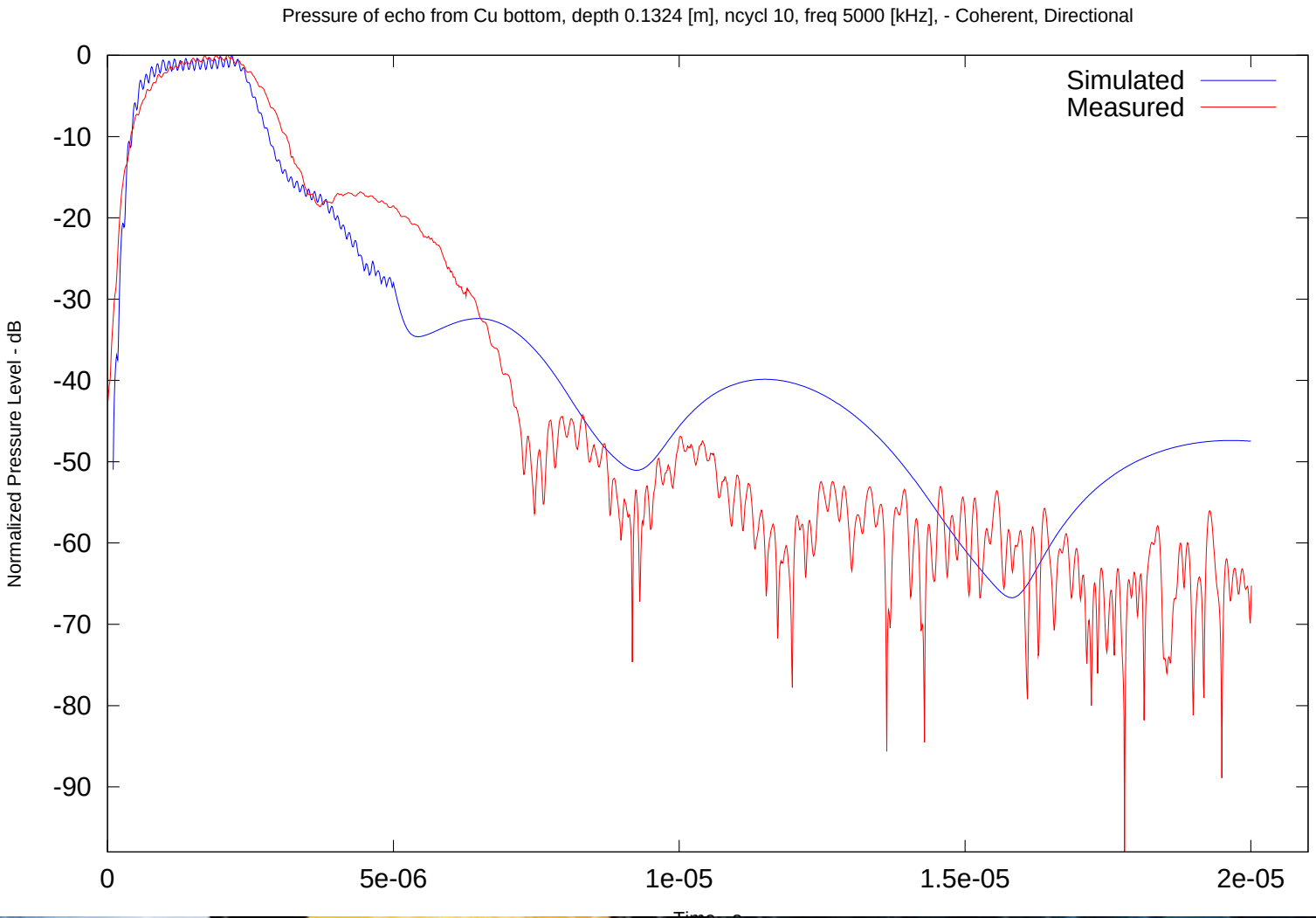

Discussion

- The measured signal has passed once more throught the transducer, while the simulated signal is calculated at the front of the transducer

Discussion

- The measured signal has passed once more throught the transducer, while the simulated signal is calculated at the front of the transducer
- Thus, we need to know the impulse response of the transducer to make a fair comparison

Discussion

- The measured signal has passed once more throught the transducer, while the simulated signal is calculated at the front of the transducer
- Thus, we need to know the impulse response of the transducer to make a fair comparison
- In this example the reflection coefficent does not have a major influence, but the problem of what to use for the reflection coefficient remains, and any suggestion will be well received!

Discussion

- The measured signal has passed once more throught the transducer, while the simulated signal is calculated at the front of the transducer
- Thus, we need to know the impulse response of the transducer to make a fair comparison
- In this example the reflection coefficent does not have a major influence, but the problem of what to use for the reflection coefficient remains, and any suggestion will be well received!
- The amplitude varies with height after normalization: This indicates something is wrong in the model!!

Discussion

- The measured signal has passed once more throught the transducer, while the simulated signal is calculated at the front of the transducer
- Thus, we need to know the impulse response of the transducer to make a fair comparison
- In this example the reflection coefficent does not have a major influence, but the problem of what to use for the reflection coefficient remains, and any suggestion will be well received!
- The amplitude varies with height after normalization: This indicates something is wrong in the model!!
- No conclusions so far - further work needed.

Discussion

- The measured signal has passed once more throught the transducer, while the simulated signal is calculated at the front of the transducer
- Thus, we need to know the impulse response of the transducer to make a fair comparison
- In this example the reflection coefficent does not have a major influence, but the problem of what to use for the reflection coefficient remains, and any suggestion will be well received!
- The amplitude varies with height after normalization: This indicates something is wrong in the model!!
- No conclusions so far - further work needed.

Thank you for your attention!, but there is more ..

Simulation for Noela's experiment

Burst

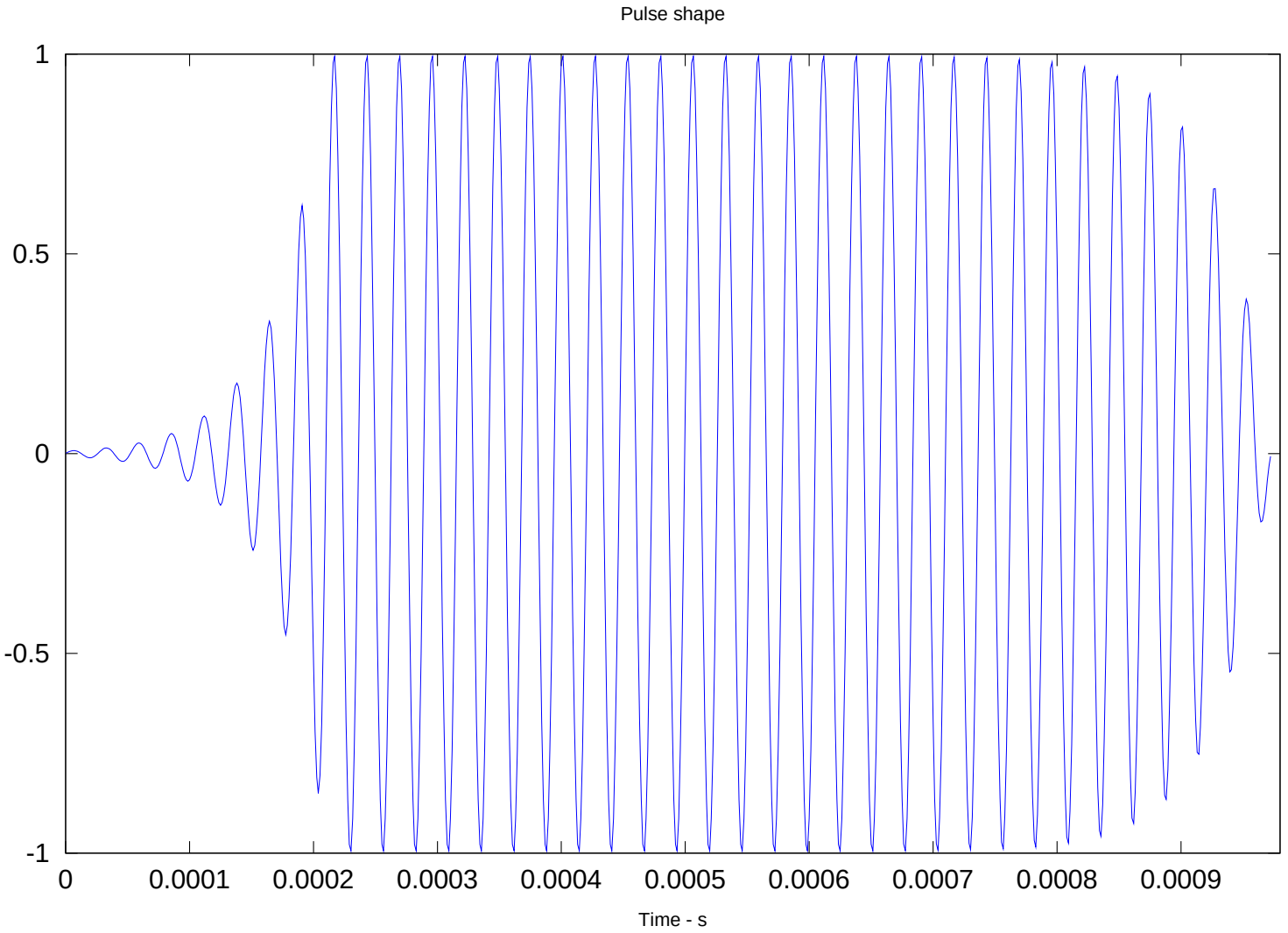

Simulation for Noela's experiment

Reflected signal

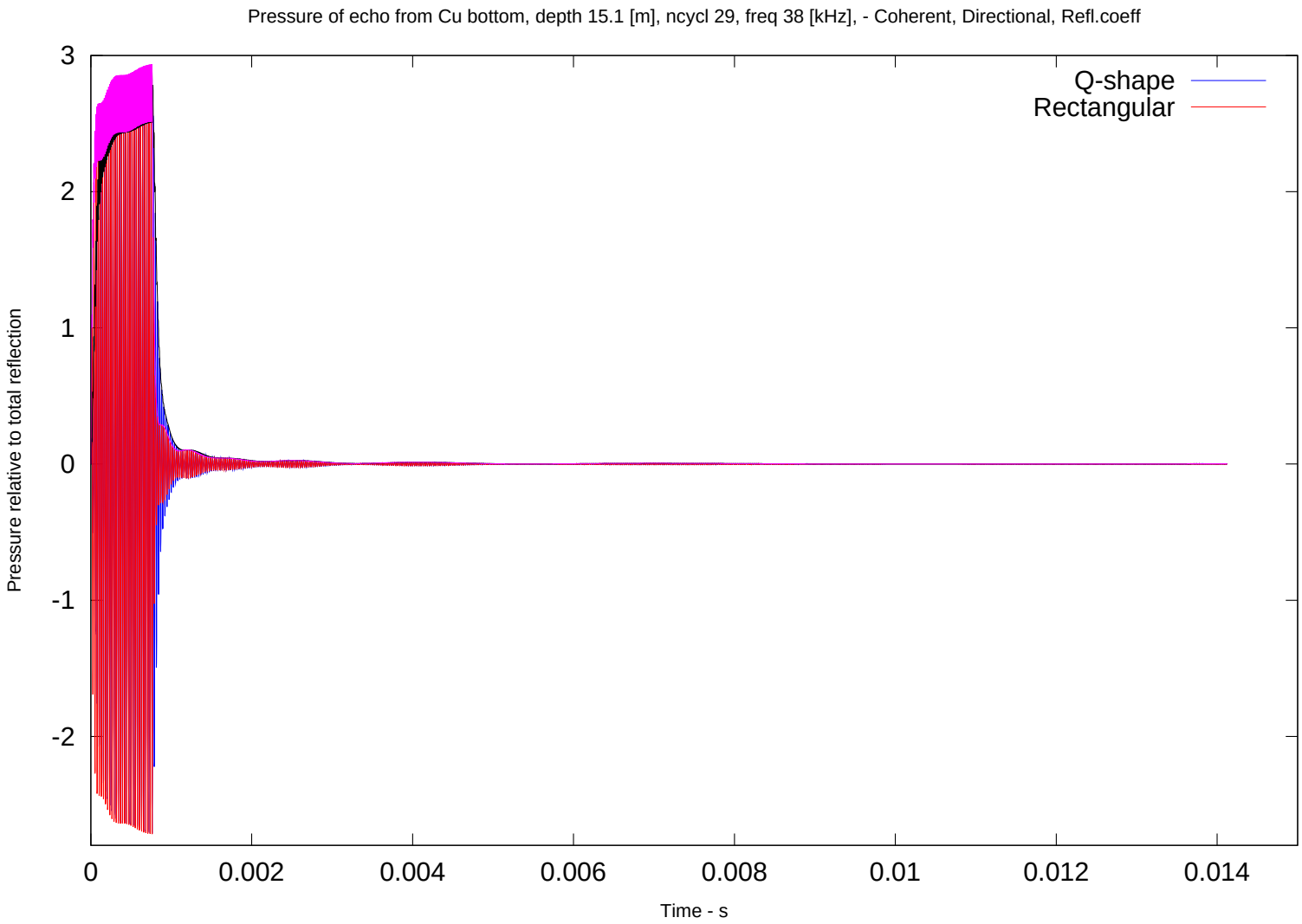

Simulation for Noela's experiment

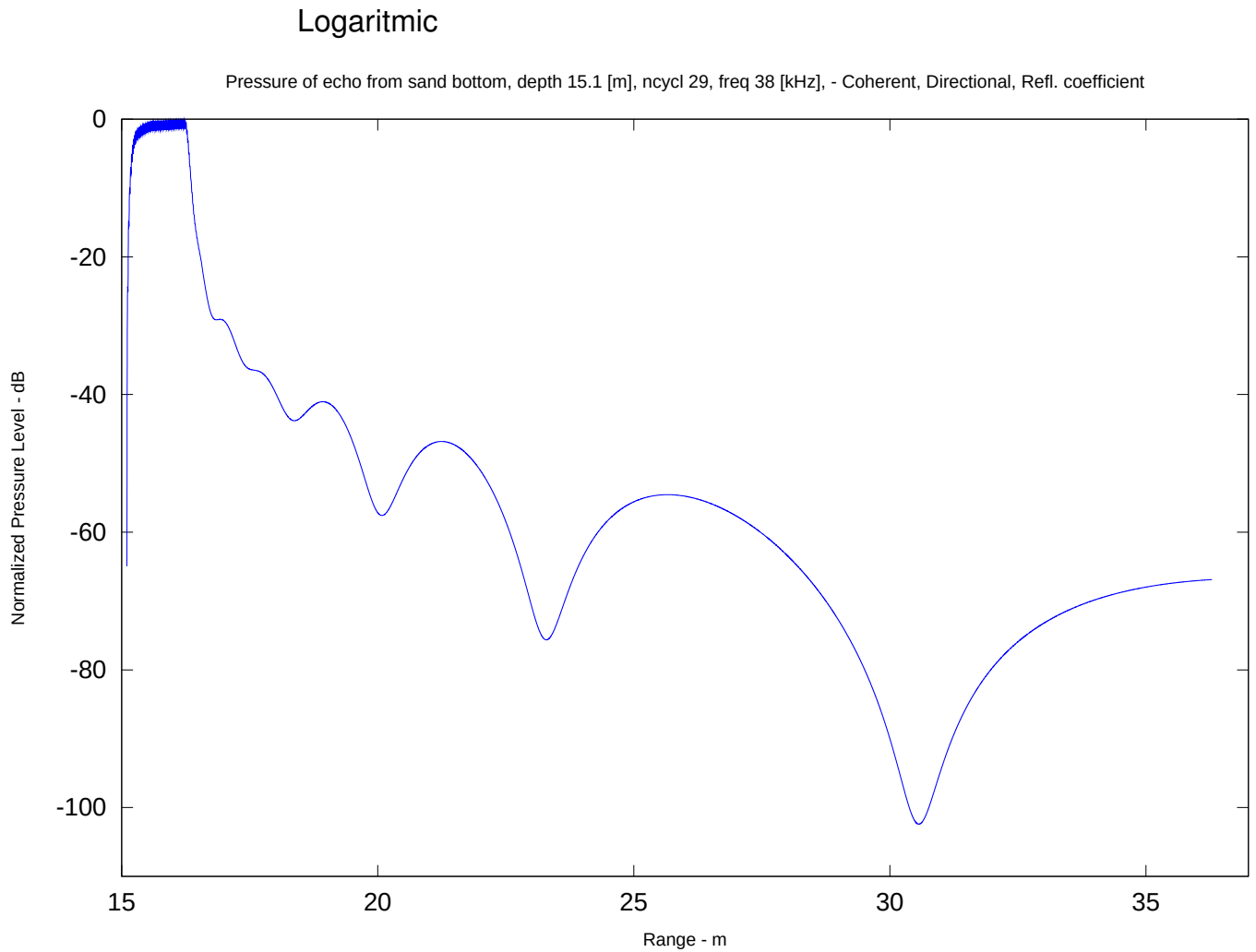

Simulation for Noela's experiment

Experiment

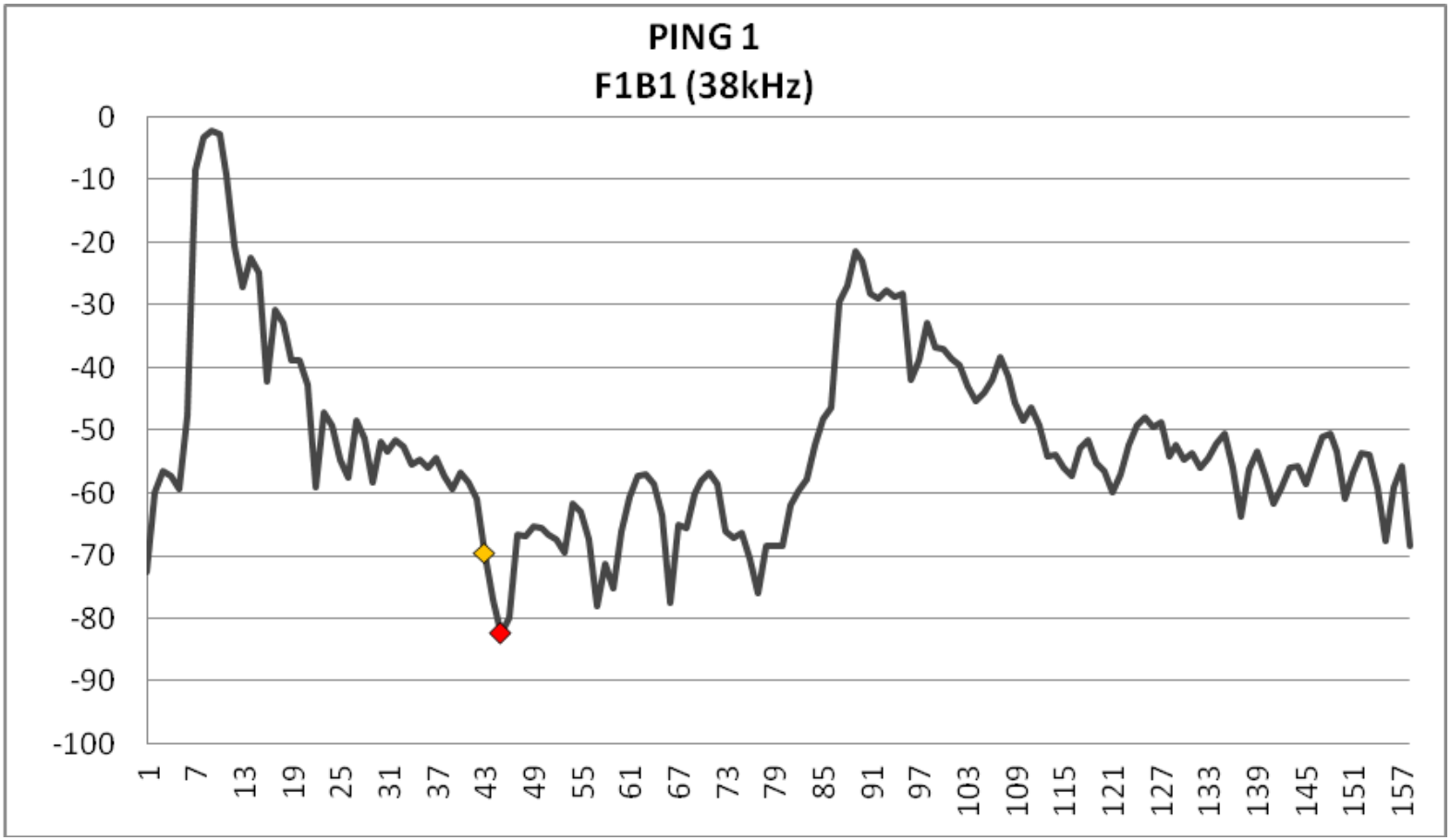

Comments on comparison with Noela's experiment

Pulse shape guessed, not exact

Comments on comparison with Noela's experiment

Pulse shape guessed, not exact
The log plot show interesting dips. Noela's range starts 7 m before the bottom: to compare subtract 8 m from her scale!

Comments on comparison with Noela's experiment

Pulse shape guessed, not exact
The log plot show interesting dips. Noela's range starts 7 m before the bottom: to compare subtract 8 m from her scale!
Thus, the big dip at 31 m matches roughly her dip at 44!

Comments on comparison with Noela's experiment

Pulse shape guessed, not exact
The log plot show interesting dips. Noela's range starts 7 m before the bottom: to compare subtract 8 m from her scale!
Thus, the big dip at 31 m matches roughly her dip at 44!
No parameter adjustments tried so far

Comments on comparison with Noela's experiment

Pulse shape guessed, not exact
The log plot show interesting dips. Noela's range starts 7 m before the bottom: to compare subtract 8 m from her scale!
Thus, the big dip at 31 m matches roughly her dip at 44!
No parameter adjustments tried so far
Scaled experiments on sand bottom will be made soon

Concluding remarks

This investigation has only just started. Several questions arose while putting up the simulation code, which still remain to be answered. Most important: realistic reflection coefficient! Also imperative to solve: Why does not the normalizing of the amplitude work?

32nd Scandinavian Symposium on Physical Acoustics, Finse, Norway, 08 - 11 February 2009

Deposit detection using plate waves

Remi A. Kippersund[1,2], **Per Lunde**[2,1] **and Kjell-Eivind Frøysa**[1]

[1] Christian Michelsen Research AS (CMR), P.O.Box 6031 Postterminalen, N-5892 Bergen, Norway

[2] University of Bergen, Dept. of Physics and Technology, Allégaten 55, N-5007 Bergen, Norway

1 Introduction

Methane hydrates are ice-like crystals [1] that impose a threat to oil and gas transport pipelines as they can accumulate and clog the pipes. Methane hydrates form under unfavorable process conditions like low seabed temperature and high fluid pressure. Such process conditions are encountered more and more often as subsea processing and transportation of multiphase fluids over long distances is becoming a viable solution for several oil and gas fields. Solutions for monitoring hydrate formation are highly called for.

Guided waves in pipes and plates are popular in non-destructive testing (NDT) due to their low attenuation and full coverage potentials [2-10]. Different modes have different properties that can be exploited in the search for a specific fault. Examples of such are the dispersive nature of some modes that are being used to measure thickness changes by sound velocity (for example due to corrosion) [3], and mode conversion, which can indicate fault in welds based on non-symmetric reflection [4,5].

The aim in this work is to study modes and methods to investigate the potentials for detecting wall deposition and growth of methane hydrates in wet gas transport pipelines using guided ultrasonic waves. There has been a resent growing interest in using guided waves for deposit detection and characterization. The studies have been reported with basis in deposition problems from many industries like oil, food and chemical, see e.g. [11-15]. The problem of detecting a deposit is related to typical problems in non-destructive testing, but here the aim is to detect the effect of a load on the waveguide and not a change in the waveguide itself. Like in NDT, there are different cases which can have different optimal solutions. A focus on “non-leaky modes” has been chosen for this study since these provide a means to detect wall deposits independently of flow.

The deposit is here assumed to build up gradually on the wall. Transmission measurements, like sound velocity and attenuation are therefore most likely to give best results (as opposed to detecting reflections). Mode conversion is another measurand that may add information about the deposit distribution.

2 Theory

Guided wave modes are infinite in numbers and generally dispersive. For a thorough introduction to the phenomena see e.g. the book by Joseph L. Rose [6]. To aid the

understanding of guided wave propagation and as a tool for studying the effect of added layers, a model for calculating the sound velocity and attenuation as function of frequency has been used. This model is an own implementation of the model DISPERSE as described in [7-9].

The model is based on the global matrix method [16], describing the layers as infinite plane parallel (for plates). Starting with a semi-infinite layer, which can be vacuum, liquid or solid, a number of finite layers (both fluid and solid) can be added. The final layer is another semi-infinite layer which again can be vacuum, fluid or solid. Wave attenuation is handled by complex wavenumbers and absorbing materials are included in the model by complex compressional and shear velocities as material property entries.

A similar model has been implemented for a cylindrically layered system (pipe model). Here the first layer is the cylinder core of infinite length (vacuum, liquid or solid), while the infinite layers now are annular in the cross section. The final semi-infinite layer surrounds in this case the infinitely long pipe or bar [8].

Both wavenumber dispersion curves (complex) and modeshapes (showing through thickness displacement- and stress-components) are calculated in the program. A tracking algorithm, as suggested by Lowe [7] is applied to "connect the dots" between frequency steps for the different modes. This is especially useful for calculating group velocity (see e.g. Rose [6]) defined as $c_G=\partial\omega/\partial\xi$, where ω is the angular frequency and ξ the horizontal wavenumber.

3 Simulations

3.1 Platemodes as pipemode representatives

The model described in the previous section has been used to calculate the dispersion curves of an aluminum plate, of thickness d, in vacuum as illustrated with black dotted lines in figure 1 (where the modes shown are the anti-symmetric, A_0, A_1, A_2, and symmetric Lamb-modes, S_0 and S_1). The curves show the phase velocity as a function of frequency-thickness product, fd. Aluminum is here chosen for comparison with measurements in the experiment section below.

In figure 1, the red curves (underneath the dotted black plate dispersion curves) show some of the propagating modes in an aluminum pipe with wall thickness 3 mm and inner diameter 10 cm. Note that additional propagating modes, like flexural and torsional modes that are left out from this figure.

The simulations show how it is plausible to use plates as representatives for pipes as the comparison is very good except from at low frequencies. The onset of this deviation is determined by the pipes diameter to thickness ratio, D/T (here 100/3).

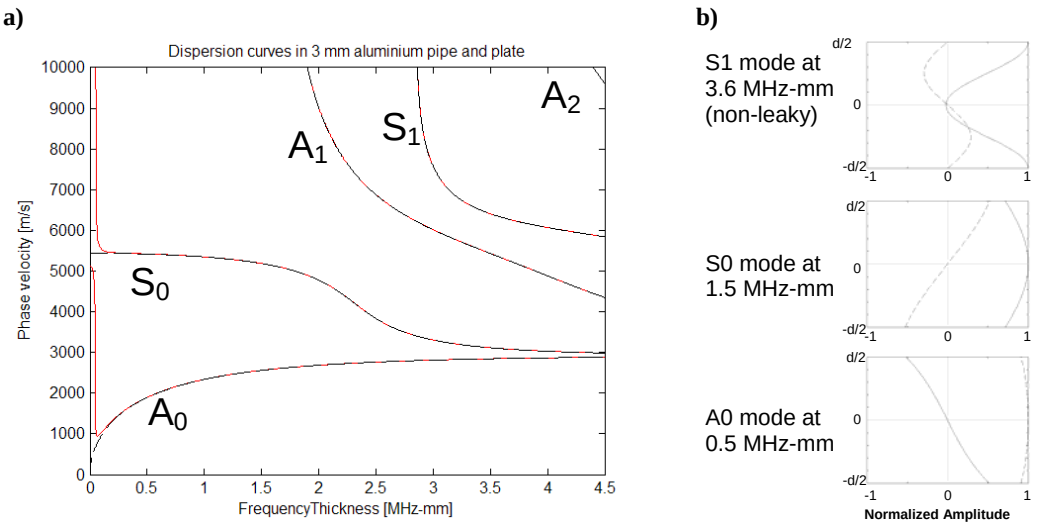

Figure 1 a) Dispersion curves for an aluminium plate (black dotted) compared with a 10 cm inner diameter, 3 mm thick aluminium pipe (red). b) Through thickness displacement components (mode shapes) of the plate with thickness, d. Dotted line: out-of-plane component. Solid line: in-plane comconent.

This onset increases to higher frequencies for smaller D/T. It is however important to remember that the comparison is done with the additional assumption of symmetric excitation around the circumference of the pipe. Otherwise another group of modes, flexural modes would occur (not shown here).

3.2 Non-leaky modes

In figure 1_b some sample mode shapes calculated by the plate model are shown. These show the in-plane and out-of-plane displacement components through the plate. The S_1 mode is termed "non-leaky" at the fd shown here (3.6 MHz-mm) because the out of plane displacement component is zero at the boundaries. The wave will therefore not radiate acoustic energy into a fluid which does not support shear forces (ideal). This property is well recognized by system designers who whish to make measurements "independently" of flow, and can be found in the symmetric modes in a narrowband close to where the phase velocity of the mode matches the bulk compressional velocity as observed by Victorov in 1967 [17].

Shear horizontal (SH) modes [9] are another group of modes with the properties of being non-leaky. The displacement components of these modes are normal to the propagation direction, and only in-plane. Having only in-plane displacement components, the modes are non-leaky at *all* frequencies. The pipe analog to these plate modes are the torsional modes which have displacement components only in the angular direction. The phase velocity dispersion curves of the first three SH modes are shown as solid lines in figure 2_a.

3.3 The effect of dispersion

The group velocity can be thought of as the signal, or envelope velocity. The group velocities shown in figure 2_b are calculated from the phase velocities shown in figure 2_a. Note that the group velocity in general is different from the phase velocity except from SH_0 which is non-dispersive. Dispersion can also cause pulses to smear out and represent by that a challenge in velocity and attenuation measurements.

a) b)

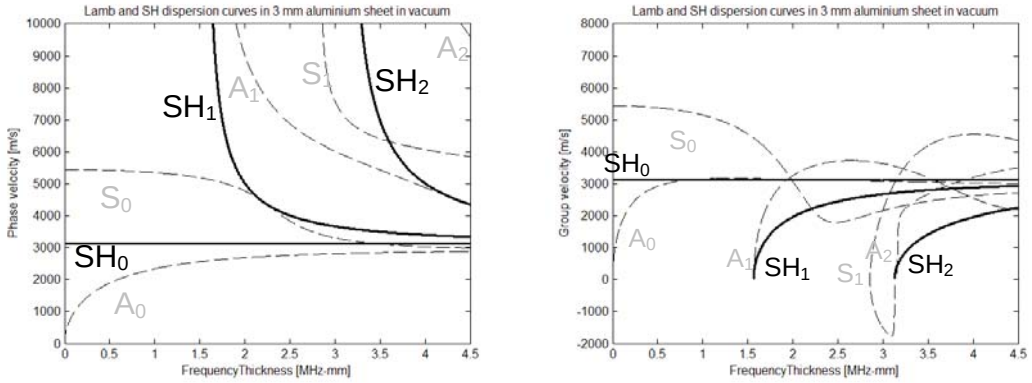

Figure 2 a) Phase and b) Group velocity dispersion curves for Lamb (dashed lines) and SH modes (solid lines) in an aluminium plate

To study this effect in some more detail, a Hanning windowed ten period sine burst is propagated as a plane wave using the phase velocity found in the model. First the pulse is propagated with the central frequency of the signal, then the frequency content of the excitation signal is propagated with the frequency dependency calculated for the mode investigated (single mode propagated as a plane wave to isolate the effect of one dispersive mode).

a) b)

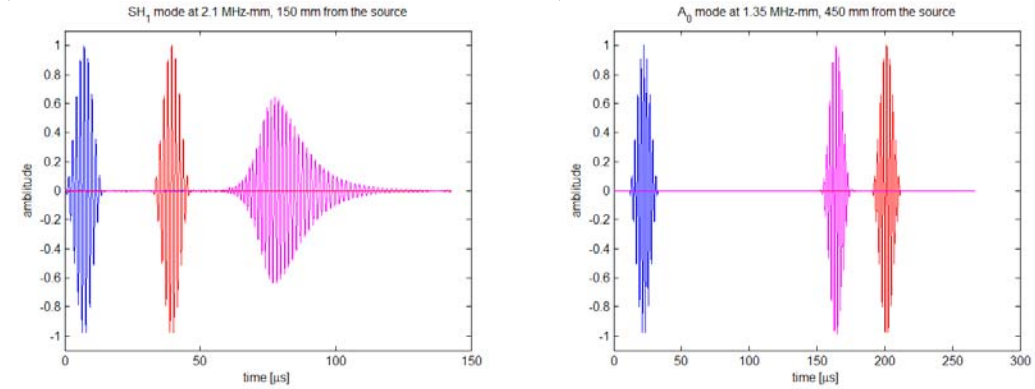

Figure 3 Dispersion demo a) SH_1 at 2.1MHz-mm b) A_0 at 1.35 MHz-mm. Plane wave propagation of a 10 period Hanning windowed sine burst (blue) propagated with:
I. constant phase speed equal to speed at centre frequency (red).
II. phase speed as calculated in figure 2a for the frequency components in the pulse (purple).

The two examples given in figure 3 are a) the SH_1 mode at 2.1 MHz-mm, and b) A_0 at 1.35 MHz-mm. The excitation signal is shown in blue in the figures. The phase and group velocities of these modes can be read from figure 2. The SH_1 mode has a group velocity lower than the phase velocity along with a positive group velocity slope. The dispersive pulse (purple) smear out and arrive later than the constant speed, center frequency propagated (red) signal in figure 3_a.

In the second example (figure 3_b), the A_0 mode is propagated at the centre frequency where the group velocity is *higher* than the phase velocity and has a zero slope (local maximum). The dispersive pulse arrives first in this example and the pulse envelope is virtually unchanged. Note that although the envelope of the pulse is travelling faster, the zero crossings still travel with the speed of the phase velocity.

3.4 Attenuating deposit layer

Adding a deposit layer of increasing thickness to the plate, it has been observed that the thinnest layers (below 0.1 mm here) only affect higher frequency ranges. Increasing the layer thickness will increasingly affect lower frequencies and add "layer-modes" to the dispersion curves. An example of dispersion curves (unloaded SH and bi-layer modes) for an aluminium plate with 0.5 and 1 mm thick viscoelastic Bitumen deposit layer on one side is shown with dotted gray lines in figure 4.

a) 0.5 mm Bitumen deposit on one side

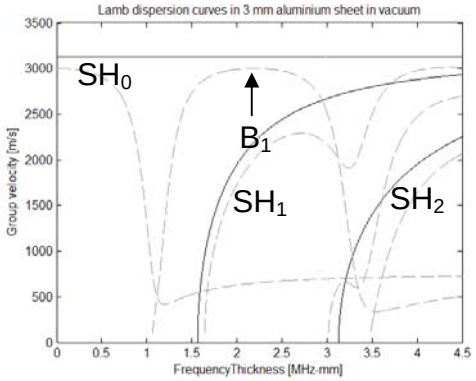

b) 0.5 mm Bitumen deposit on one side

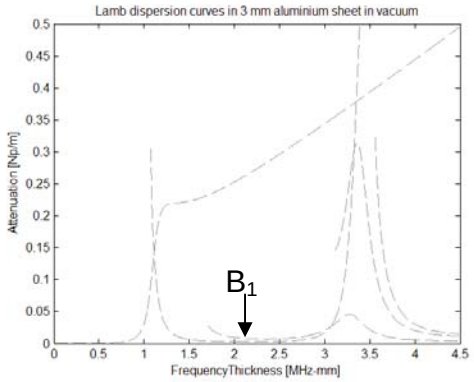

c) 1 mm Bitumen deposit on one side

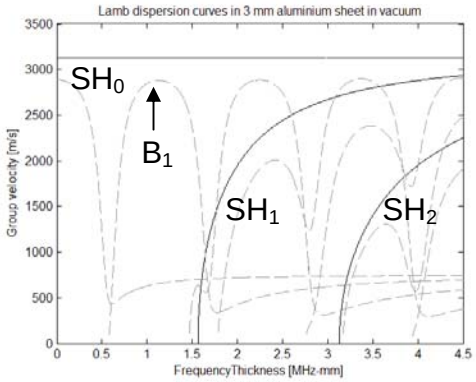

d) 1 mm Bitumen deposit on one side

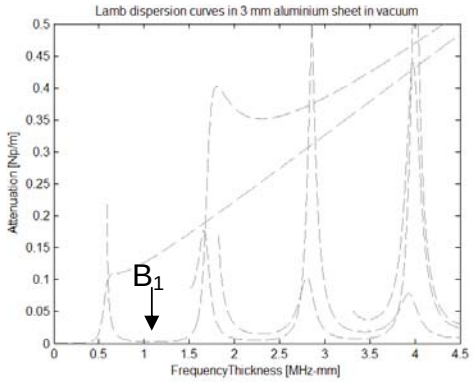

Figure 4 Left column: Group velocity and Right column: Attenuation for guided wave modes in an aluminium plate covered with a Bitumen deposit layer on one side. The thickness of the deposit was 0.5 mm (top row) and 1 mm (bottom row).

Figure 4_a and 4_c show the group velocity and figure 4_b and 4_d show the attenuation of the bi-layer modes. The thickness dependent second bi-layer mode, B_1 is indicated by an arrow in the figures. The black solid lines are the group velocity curves of the unloaded SH modes from figure 2_b. The viscoelastic Bitumen deposit is as described by Barhinger et. al. [10] with density, $\rho = 1500$ kg/m^3, compressional velocity $c_L =$ 1860 m/s, shear velocity $c_S = 750$ m/s, compressional absorption $\alpha_L/\omega = 0.000023$ s/m and shear absorption $\alpha_S/\omega = 0.00024$ s/m.

4 Two initial experiments

Both dispersion and multimode propagation complicate signal interpretation of guided waves. A typical approach in NDT is to optimize a system for single mode excitation [4]. It is then preferable to operate on frequencies below the cutoff of higher order modes where few modes exist. Another approach is to deal with multiple modes for example by some kind of spectrogram analysis, see e.g. [15]. The goal then may be to

get a broader picture of the different modes present to characterize the waveguide. In the first experiment shown here, the goal was to investigate which modes were transmitted in a simple transducer configuration.

In the second experiment, spectral amplitude components were studied with different loads on the plate. Again, no attempt was made to work on a single mode, but a window was put on the time domain signal to avoid edge reflections.

4.1 Experimental setup

The experiment was conducted on a 6082 T6 Aluminum plate with dimensions LWD (length x width x depth) 1750 mm x 1000 mm x 3 mm, see figure 5_a. The material data used in the modeling for the aluminum plate was: Density, ρ = 2700 kg/m^3, compressional velocity, c_L = 6320 and shear velocity, c_S = 3130. The elements where shear polarized gold plated PZT27 rectangular plates LWD = 18 mm x 3 mm x 1 mm, optimal for exciting SH modes. Sending and receiving elements (one of each) were glued to the plate with Araldite 2020 and the separation between sender and receiver was 500 mm.

4.2 Plate without deposit, spectrogram analysis

The spectrogram shown in figure 5_b was obtained experimentally by adding 190 spectrograms with 10 period sine excitations from 110 kHz to 299 kHz in 1 kHz steps. Overlaid the experimentally obtained intensity plot are the calculated *group velocity* dispersion curves converted into travelling times. The colors on the modeled curves represent shear horizontal (black), asymmetric- (blue) and symmetric-lamb modes (red), respectively. Besides from the shear horizontal modes actually aimed for, there are observed traces of both symmetric and asymmetric lamb modes. In addition there are some late arrivals in the range 0.5 to 1 MHz-mm which are not accounted for by the "direct path" propagation curves.

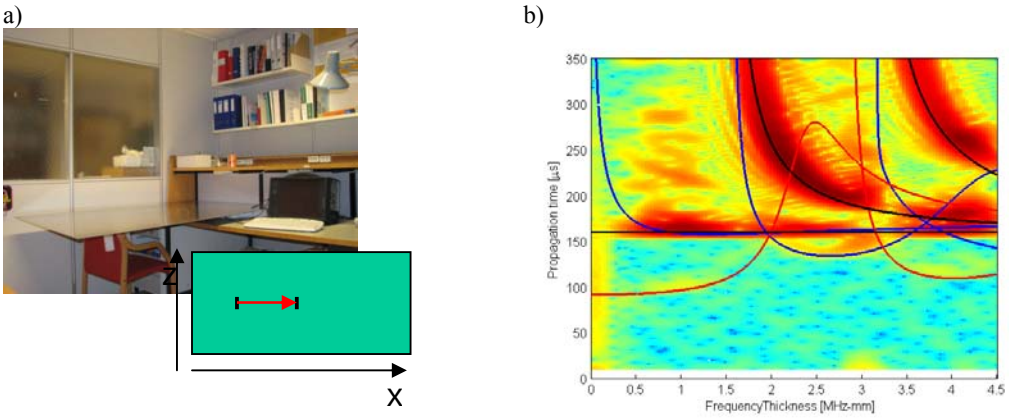

Figure 5 a) Experiment with shear polarized PZT elements to excite SH waves in an Aluminium plate. b) Spectrogram analysis (experimental data) and calculated group velocity dispersion curves converted to time of flight. Blue, red and black curves represent asymmetric-, symmetric- and SH-modes respectively.

4.3 Plate with deposit, spectral amplitudes

In figure 6_a the signal picked up by the receiver with air loading is shown (in black and red). The excitation signal was a single sine period at 400 kHz. The red part is the segment used as input to the FFT shown as the air loading curve in figure 6_b.

Similarly, the frequency responses with different loading layers are shown in figure 6_b with colors and styles as indicated by the legend.

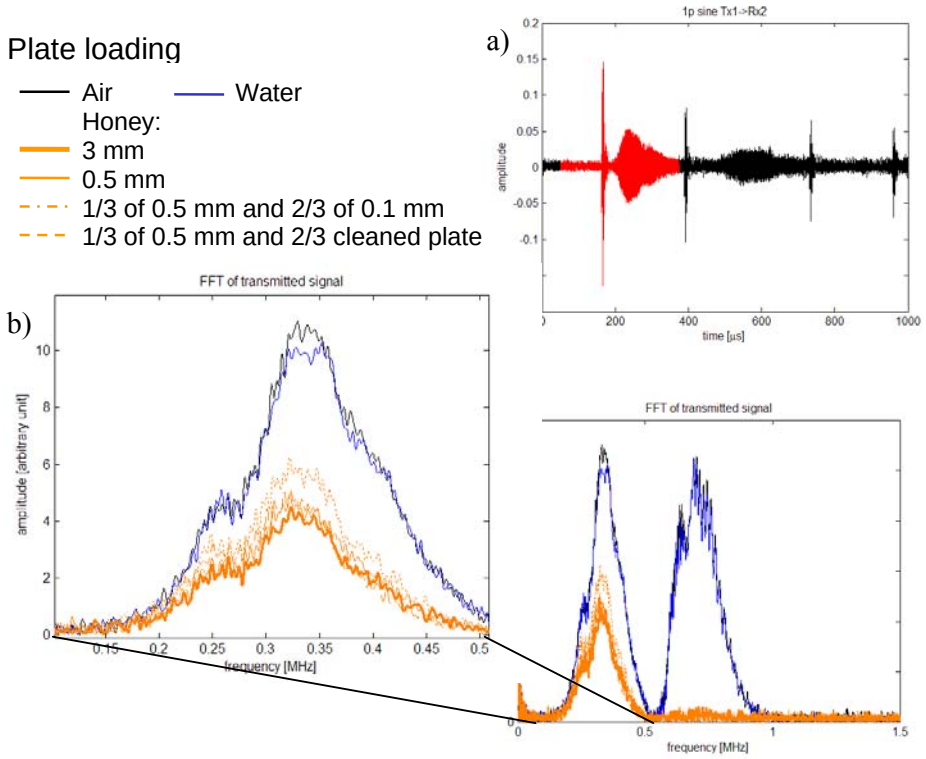

Figure 6 a) Received signal from a 400 kHz sine period transmitted 50 cm along the 3 mm aluminium plate. b) Frequency domain representation of the red part of the signal in a) with different plate loadings (see legend)

The different loads studied in this experiment were water and different layers of honey as indicated by the legend in figure 6. The honey was off the shelf Norwegian honey, "Ekte honning" from Honning centralen. An approximately 5 cm wide strip was laid in the propagation path between, and about 10 cm beyond, the transducer elements. The dashed lines in the legend of figure 6 indicate parts of honey removed transversally to the propagation direction, leaving 4 cm long lumps of honey and about 8 cm of open spaces between them.

5 Discussion

Methane hydrate formation in oil and gas transport pipelines can occur both in the flow and on pipe walls. In this work, the focus has been on hydrates forming and growing on the pipe wall. This is therefore seen a problem of detecting the loading effect on a wave travelling in the pipe wall. Transmission measurement quantities, like sound velocity and attenuation were considered here to be most promising measurands. Properties of mode propagation that affect the decision on mode selection and processing technique were studied in the paper.

A model based on the global matrix method for calculating dispersion curves and mode shapes of multilayered plates and pipes has been implemented to study the effect of loading on guided wave modes. This model was used to check how plates could be used as representatives for pipes in the initial work since a plate was considered easier to do experiments on. The pipe modes were well described by the

plate modes except from at low frequencies. The onset of this deviation was not studied in detail in this work but it was observed that it was connected to the pipe diameter to thickness ratio.

Since the problem is to detect the effect of a viscoelastic load on a fluid (wet gas) flowing pipe, non-leaky modes like torsional, or shear horizontal for plates are especially interesting. With these modes it is possible to discriminate between non-viscous (flowing fluid) and other (actual) deposit layers.

Phenomena like group velocity and signal smearing, which are related to mode dispersion where studied in a simplified single mode plane wave pulse propagation calculation. Phase velocity dispersion curves calculated in the above mentioned model was used as input to these calculations. Traditional techniques like zero crossing for sound velocity and peak detection for attenuation are both affected by these phenomena. Signal smearing can be minimized by operating at a zero slope (max peak) group velocity.

As an alternative to single mode pulse detection, spectrogram analysis has been tested in an experiment. The experiment was here run to see which modes were present in a transducer setup using shear polarized PZT elements oriented to excite SH modes. It was demonstrated how the calculated group velocity describe the signal propagation in the plate. Besides the SH modes, traces of S_0, S_1 and A_1 were observed in the transmitted signal.

Deposit layers were investigated both with simulations and experimentally. The simulations indicated a potential use of sound velocity to measure the thickness of the deposit layer. The sound velocity thickness dependence was found at a frequency times thickness product where the group velocity had a maximum peak and the attenuation was at a minimum as indicated by arrows in figure 4. These features both spoke in favor of a method based on measuring thickness by the sound speed of these modes. A feasibility study on this possibility was done by Ma et. al. [15]. An analysis similar to the one in figure 5_b (but with reassigned spectrogram for better resolution) was run to obtain a broad picture of the bi-layer modes. The modes calculated were successfully reproduced in the experiment and thickness could be quantified but only as long as the layer was covering the whole circumference of the pipe. The weakness is that the method relay on bi-layer modes where the deposit itself acts as a waveguide. Applied to a practical situation with inhomogeneities both in material properties and spread, it will probably not produce clean mode curves and thickness information may be hard to extract.

In the second experiment, the focus was on spectral amplitude changes due to waveguide loading. Not seeking to sort out a single mode, the signal input to the Fourier transform was truncated just before first edge reflection including contributions from as many modes as possible in the limit of the size of the plate. In this initial experiment, indications were found on an increase in attenuation with increasing amounts of honey. This experiment was however not set up for systematic studies of the loading effect, but more as a first test on experimental setup and processing algorithms. Work is currently being done on methods to improve frequency and wavenumber bandwidth and signal to noise ratio of the measurements in order to do a more thorough attenuation study with deposits.

6 Acknowledgements

The work presented here has been done as part of a PhD fellowship of the 1st author (2008-2011), under a 4-year strategic institute programme (SIP), "Multimodal flow assurance metering station (MuFAMES)" (2006-2009), which is carried out in a cooperation between Christian Michelsen Research AS, the University of Bergen (UoB) / Dept. of Physics and Technology, and StatoilHydro ASA. The SIP is supported by the Research Council of Norway (NFR).

7 References

1. E. D. Sloan, and C. A. Koh. *Clathrate hydrates of natural gases*. CRC Press, 2007.
2. D. N. Alleyne, B. Pavlakovic, M. J. S. Lowe, and P. Cawley, "Rapid, long range inspection of chemical plant pipework using guided waves," Insight 43,(2001): 93-96.
3. Jenot, F., M. Ouaftouh, M. Duquennoy, and M. Ourak. "Corrosion thickness gauging in plates using Lamb wave group velocity measurements." *Measurement Science and Technology* 12, no. 8 (2001): 1287-1293.
4. Cawley, P., M. J. S. Lowe, D. N. Alleyne, B. Pavlakovic, and P. Wilcox. "Practical long range guided wave inspection–applications to pipes and rail." *Proceedings of NDE2002,, Chennai, India* (2002): 5-7.
5. John J. Ditri, "Utilization of guided elastic waves for the characterization of circumferential cracks in hollow cylinders," The Journal of the Acoustical Society of America 96, no. 6 (December 0, 1994): 3769-3775.
6. Joseph L. Rose, Ultrasonic Waves in Solid Media (Cambridge University Press, 1999).
7. M.J.S. Lowe, "Matrix techniques for modeling ultrasonic waves in multilayered media." *Ultrasonics, Ferroelectrics and Frequency Control, IEEE Transactions on* 42, no. 4 (1995): 525-542.
8. B. N. Pavlakovic, "Leaky guided ultrasonic waves in NDT," Ph.D. thesis, University of London, Imperial College of Science, technology and medicine (1998)
9. Simonetti, F. *Sound propagation in lossless waveguides coated with attenuative materials* Ph.D. thesis, University of London, Imperial College of Science, technology and medicine (2004)
10. J.N. Barshinger, and J.L. Rose. "Guided wave propagation in an elastic hollow cylinder coated with a viscoelastic material." *Ultrasonics, Ferroelectrics and Frequency Control, IEEE Transactions on* 51, no. 11 (2004): 1547-1556.
11. Kenneth R. Lohr and Joseph L. Rose, "Ultrasonic guided wave and acoustic impact methods for pipe fouling detection," Journal of Food Engineering 56, no. 4 (March 2003): 315-324.
12. Thomas R. Hay and Joseph L. Rose, "Fouling detection in the food industry using ultrasonic guided waves," *Food Control* 14, no. 7 (October 2003): 481-488.
13. J.J. Silva, A.M.N. Lima, and J.S. Rocha Neto, "Wavelet-Based Method for Fouling Detection Using Ultrasonic Guided Waves," in Ultrasonics Symposium, 2006. IEEE, 2006, 444-447.
14. J. Ma, F. Simonetti, and M. J. S. Lowe, "Scattering of the fundamental torsional mode by an axisymmetric layer inside a pipe," The Journal of the Acoustical Society of America 120, no. 4 (October 0, 2006): 1871-1880.
15. J. Ma, M. J. S. Lowe, and F. Simonetti. "Feasibility study of sludge and blockage detection inside pipes using guided torsional waves." *Measurement Science and Technology* 18, no. 8 (2007): 2629-2641.
16. Schmidt, Henrik, and Finn B. Jensen. "A full wave solution for propagation in multilayered viscoelastic media with application to Gaussian beam reflection at fluid--solid interfaces." *The Journal of the Acoustical Society of America* 77, no. 3 (March 0, 1985): 813-825.
17. Viktorov, I. A. *Rayleigh and Lamb waves*. Plenum Press New York, 1967.

SSPA Finse 2009

Capacitive Micromachined Ultrasonic Transducer (CMUT): Conventional and collapsed operation

Hanne Martinussen, Helge E. Engan and Astrid Aksnes
Department of Electronics and Telecommunications
Norwegian University of Science and Technology

Introduction

We have previously reported on work done within the SMiDA project that aims at making a probe designed for detection of vulnerable plaques in arteries (1). The probe will contain an acoustic CMUT array including electronics attached to it, as well as an optical part intended for spectroscopic investigations. The overall diameter is going to be about 1 mm.

Here we extend this work to FEM modeling for an element that deviates from the initial symmetric design which was originally specified, but not achieved in practical production. We also have operated the CMUT in the collapsed state, and report some measured responses for this mode of operation.

FEM modeling

We have currently made a full finite element modeling based on the COMSOL software program (2) of the conventional mode.

For reference, Fig. 1 shows a sketch of the geometry of the CMUT element.

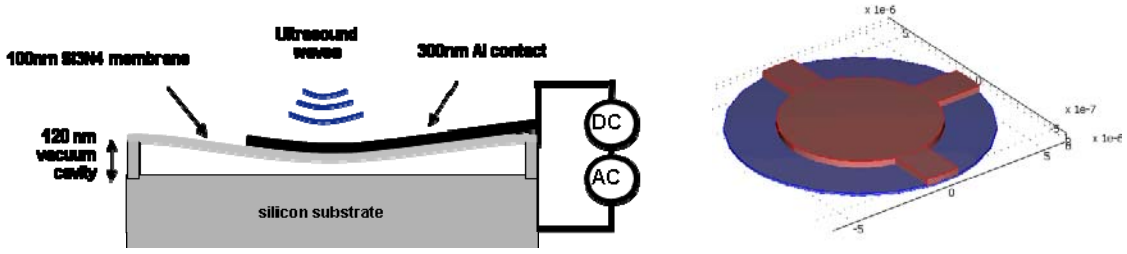

Fig. 1. a) Sketch of the CMUT element, b) perspective view of the membrane and metal electrode.

By applying the previously reported laser probe (1) at an arbitrary location on the CMUT surface, we have measured a typical frequency response as shown in Fig. 2a. We see a fundamental resonance around 30 MHz, and two higher resonances around 60 MHz. Our previously reported model which was based on symmetry around one of the three tabs shown in Fig. 1b could not account for this double resonance.

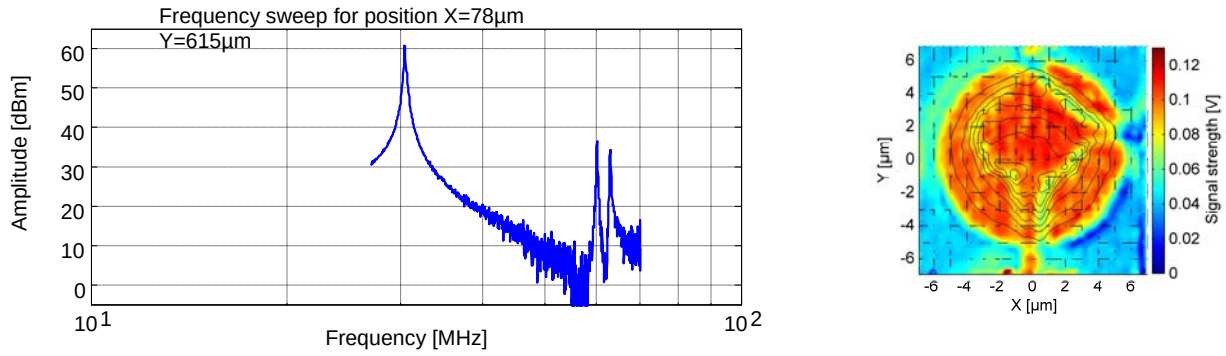

a) b)

Fig. 2. Laser probe measurements. a) Typical frequency response, b) observed reflection pattern of the CMUT.

As is demonstrated in Fig. 2b, however, there is a noticeable asymmetry in the structure as shown by the distribution of the reflected light from the CMUT surface. We have built this feature into a new FEM model as indicated in Fig. 3b. In the modeled frequency response in Fig. 3a the measured split in the higher resonance is clearly demonstrated. The placement of each resonance is relatively well reproduced after adjusting slightly some of the geometric and material parameters.

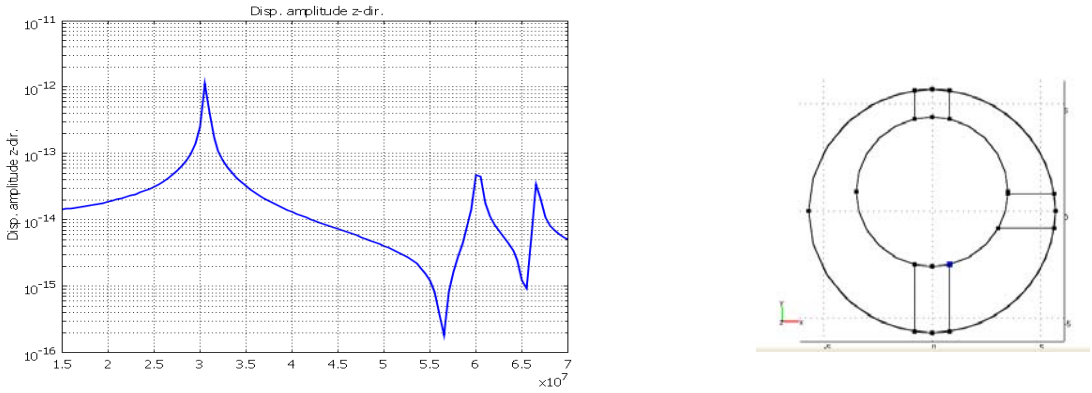

a) b)

Fig. 3. a) Simulated frequency response of vertical displacement at an arbitrary location on the CMUT as based on the asymmetric model shown in b).

From the model simulations we also obtain the displacement distribution over the surface. This is shown for all three resonances together with measured data in Fig. 4. We conclude that the simulations reproduce all main features of the measured results.

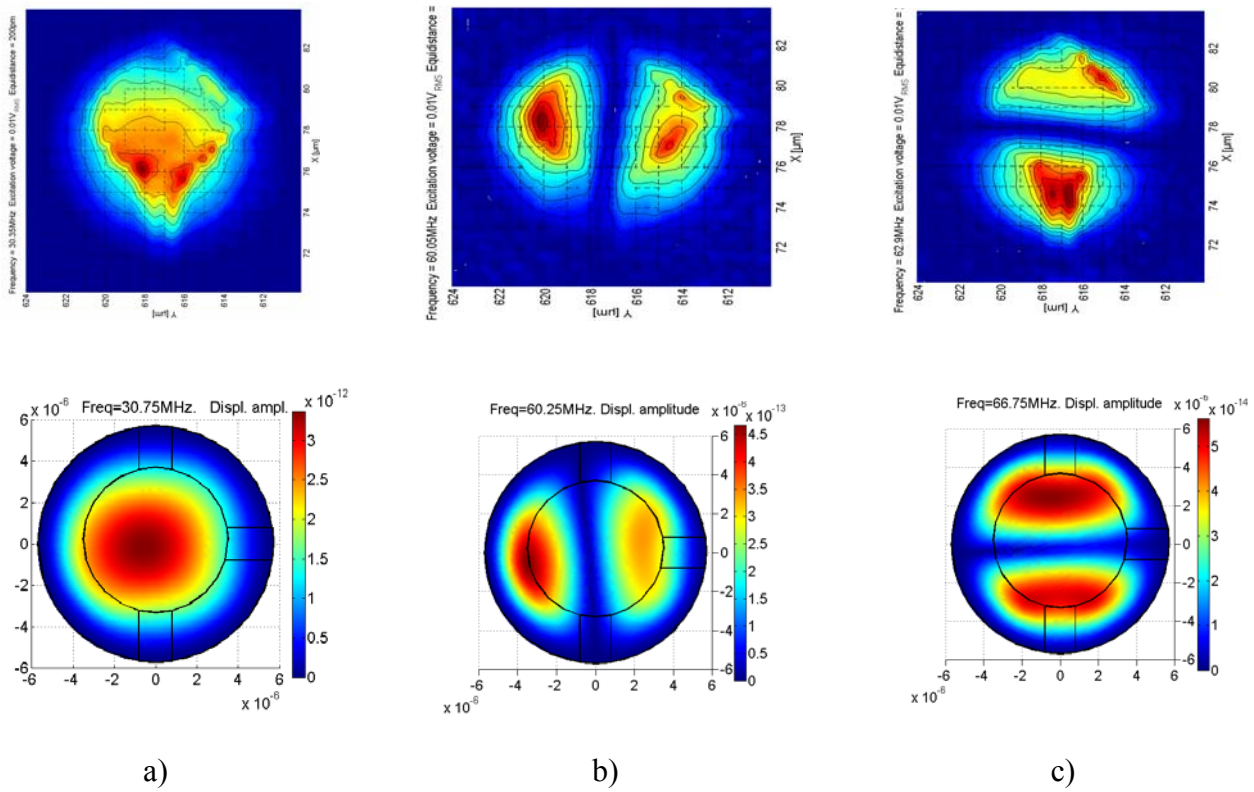

a) b) c)

Fig. 4. Amplitude distribution for the three resonances shown in Fig. 3. a) Fundamental resonance, b) and c) the two higher order resonances (note that the two lobes in each distribution are in opposite phase). Upper row: Measured distribution. Lower row: Simulated distribution.

Collapsed operation

Referring to Fig. 1a, a simple model for the pressure p exerted on the CMUT surface obtains (3)

$$p = \frac{\varepsilon_0}{2}\left(\frac{V_{DC} + V_{AC}\cos(\Omega_a t)}{d}\right)^2$$ where Ω_a is the acoustic frequency and d is the gap width. To first order when $V_{AC} \ll V_{DC}$, this can be written $p = \frac{\varepsilon_0}{2d^2}\left(V_{DC}^2 + 2V_{DC}V_{AC}\cos(\Omega_a t)\right)$. The first order term in this expression shows that a high value of V_{DC} is required to obtain a high vibration coupling. However, this means that the zero order term gives a high static deflection of the membrane, so that the value of d is reduced. Therefore, the gap width decreases more strongly than according to a quadratic law, eventually yielding an unstable situation in which the membrane collapses onto the bottom of the cavity at what we call the snap-in voltage. This is illustrated in Figs. 5 and 6. Upon further increase of V_{DC} the CMUT stays in a relatively stable collapsed state. By reducing the voltage when in this state, the CMUT stays in this same state until well below the snap-in voltage. Eventually it goes back to the conventional state at the snap-out voltage.

a) b)

Fig. 5. Cross sections of CMUT in a) conventional and b) collapsed operation

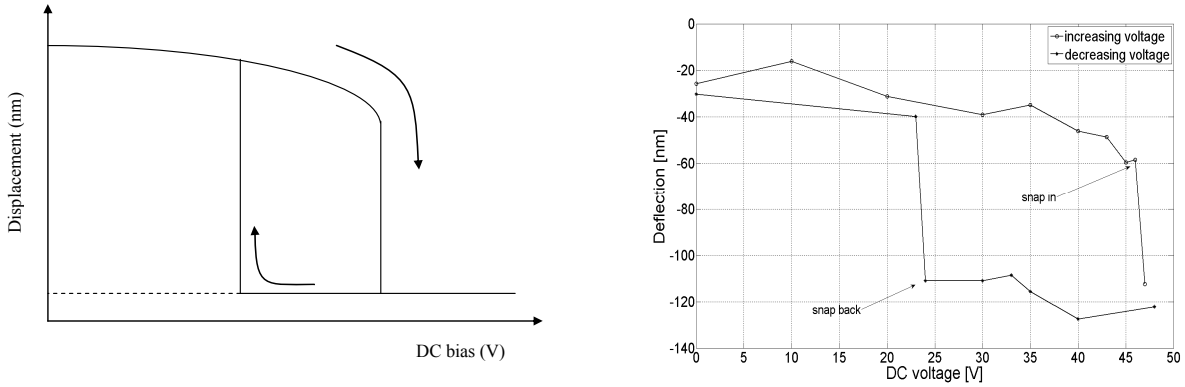

Fig. 6. Deflection of membrane as function of bias voltage, a) principle, b) optically measured response at center of CMUT.

In these and subsequent measurements we have used the optical probe in a new way. From previous reports (1) we deduce that the detected signal contains the following terms of interest:

$$I = \underbrace{A_1^0 A_2^0}_{I_0} \cos\left(\Omega_m t \underbrace{-\phi_1 + \phi_2}_{\psi_0} \right) + \underbrace{A_1^0 A_2^0 \frac{2\pi a}{\lambda}}_{I_1} \cos\left(\left(\Omega_a - \Omega_m\right) t \underbrace{+\phi_1 - \phi_2 + \phi - \pi/2}_{\psi_1} \right)$$

where the quantities $I_0, I_1, \psi_0,$ and ψ_1 are readout values from the measurement setup. We have previously used the following relations for determining the amplitude *a* and phase ϕ of the vibrations:

$$a = \frac{\lambda}{2\pi}\frac{I_1}{I_0}, \quad \phi = \psi_0 + \psi_1 + \pi/2 .$$

In addition, all other quantities being equal we can image the surface based on the optical reflectivity being proportional to I_0 while the topography can be deduced from the surface height. This is given by $y = \frac{\lambda}{4\pi}\psi_0 + const.$ These quantities are measured basically in the baseband. Therefore the height measurement is dependent on high stability of both optical arms. It is thus of interest to find the detection limit of this quantity. In our setup it seems that this stability currently is of the order of 10 nm or somewhat larger in a typical measurement series.

Based on these considerations we have measured the surface profiles in conventional and collapsed operation. A typical result is shown in Fig. 7 where measured profiles across the CMUT and including two opposite tabs are shown for the two situations. Also shown is a curve depicting the difference in the two profiles, i.e., the actual voltage-induced displacement. It should be noted that certain artifacts occur caused by different optical properties of the various materials. These artifacts can give systematic errors, but they are not accounted for here.

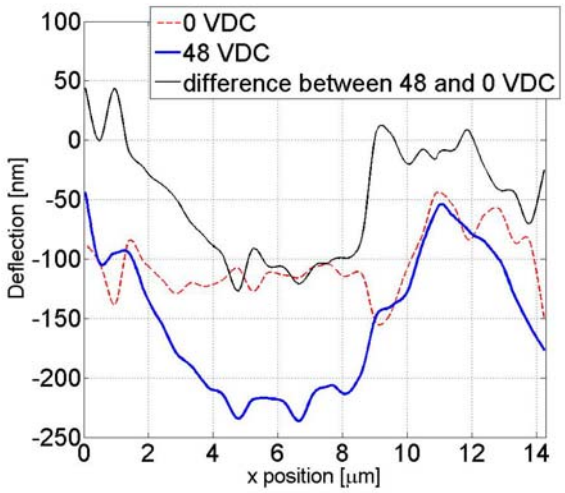

Fig. 7. Measured static profiles of CMUT for 0 VDC and 48 VDC which is slightly above the snap-in voltage. The black curve is the difference between the two measurements.

Inspecting Fig. 5b we expect acoustic resonance frequencies to be generally higher in collapsed operation than in conventional operation since the effective membrane width is smaller in the collapsed state. Due to lack of symmetry of the CMUTs we decided to make optical frequency scans at four different locations as shown in Fig. 8. It is observed that there is a relatively large difference in the spectra. Mode patterns for two typical resonances are shown in Fig. 9.

Conclusion

We have reported simulations of the non-symmetric CMUT in conventional operation, obtaining simulated data agreeing well with measured data. The laser probe has been used to retrieve static profiles simultaneously with vibration data. This is an important feature which is not published before. In addition, vibration modes under collapsed operation has been measured. Such detection has required the laser probe to operate beyond 150 MHz, which is still well below the designed frequency limit of about 1GHz.

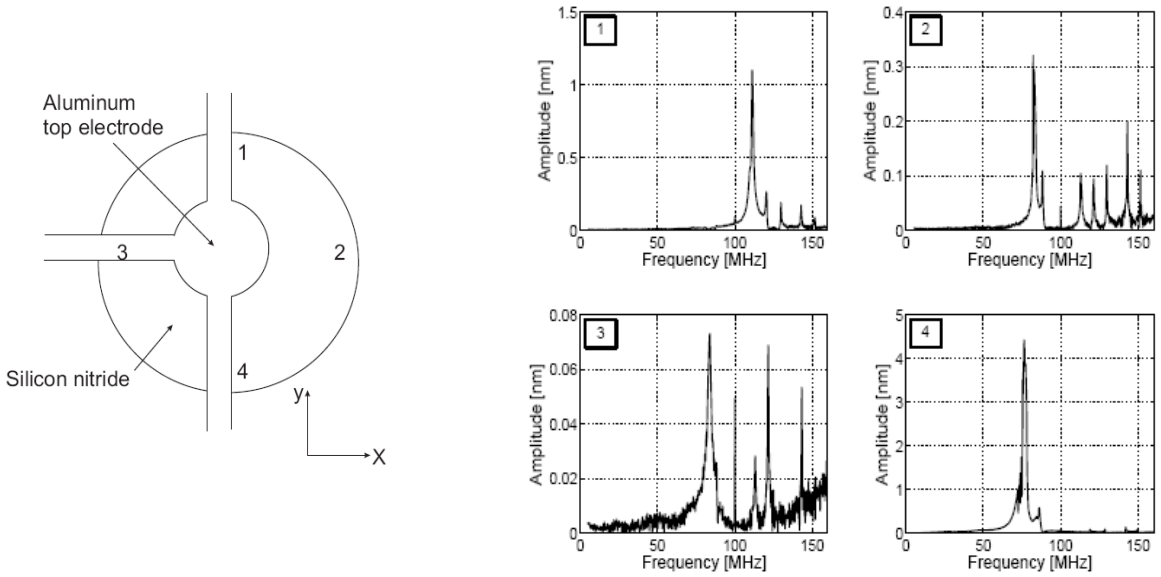

a) b)

Fig. 8. a) Four locations where optical frequency scans shown in b) were made.

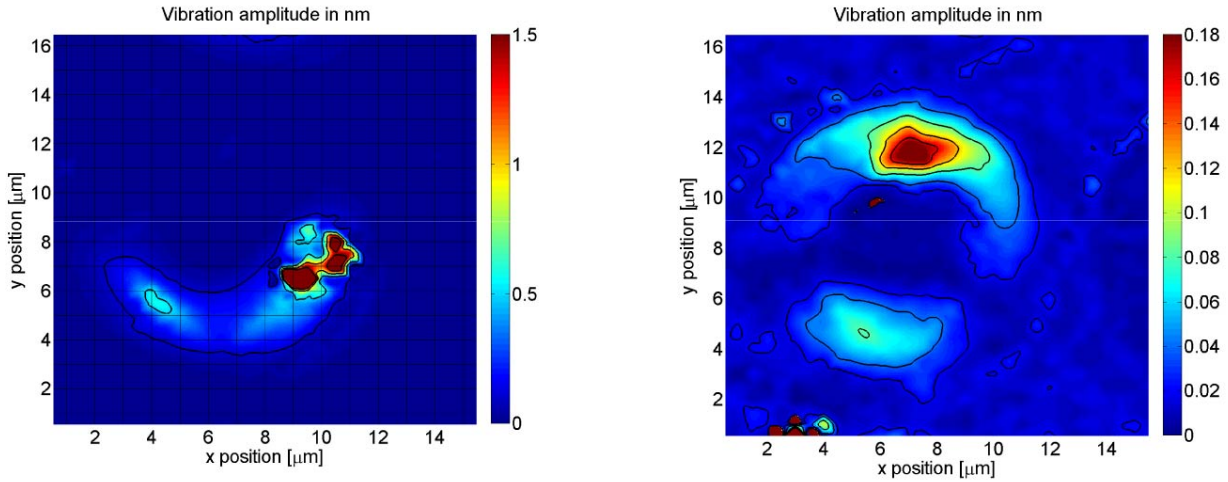

a) b)

Fig. 9. Mode patterns as measured optically for a) 76.5 MHz and b) 113 MHz

1 H. Martinussen, A. Aksnes, H.E. Engan, "Heterodyne interferometry for acoustic vibrations", Proc. of the 29th Scandinavian Symposium on Physical Acoustics, Norwegian Physical Society (NFS) 2006 ISBN 82-8123-001-0.

2 www.comsol.com

3 A. Nikoozadeh, B. Bayram, G.G. Yaralioglu, and B.T Khuri-Yakub, " Analytical calculation of collapse voltage of CMUT membrane", Proc. 2004 IEEE International Ultrasonics, Ferroelectrics, and Frequency Control Conf., p. 256.